Near-single-cycle laser for driving relativistic plasma mirrors at kHz repetition rate - development and application

Frederik Böhle

To cite this version:

Frederik Böhle. Near-single-cycle laser for driving relativistic plasma mirrors at kHz repetition rate - development and application. Optics [physics.optics]. Université Paris Saclay (COmUE), 2017. English. NNT : 2017SACLX116 . tel-01806334

NNT : 2017SACLX116

Thèse de doctorat
de l'Université Paris-Saclay
préparée à l'Ecole Polytechnique

Ecole doctorale n°572
Ondes et Matière
Spécialité de doctorat: Physique

par

Frederik Böhle

Near-single-cycle laser for driving relativistic plasma mirrors at kHz repetition rate - development and application

Thèse présentée et soutenue à Palaiseau, le 08 décembre 2017.

Composition du Jury :

M.	Manuel Joffre	Professeur associé École Polytechnique	(Président du jury)
M.	László Veisz	Professeur Umea University	(Rapporteur)
M.	Fabien Dorchies	Directeur de Recherche CELIA	(Rapporteur)
Mme.	Aurélie Jullien	Chargé de Recherche INLN	(Examinatrice)
M.	Antoine Rousse	Directeur de Recherche LOA	(Directeur de Thèse)
M.	Rodrigo Lopez-Martens	Chargé de Recherche LOA	(Co-Directeur de Thèse)

Acknowledgements

First I would like to thank Manuel Joffre, László Veisz, Fabien Dorchies and Aurélie Jullien as members of the jury for taking the time and interest to read the manuscript and assist in the PhD defense. It was a great pleasure and honour to discuss my work with you, besides the corrections to the manuscript were very helpful.

We live in an ultrafast world and just as is our laser system, my time at the LOA felt very short and intense. It was such a pleasant atmosphere working together hand in hand with so many great people and scientists that I feel very lucky having been given this opportunity. The *French way of life* created a very warm and interactive environment. Often at lunch our discussions would develop into heated debates about the latest events, politics, or just how to completely reshape society for a better world. These deep-dives, away from the day-to-day science, were the ideal balance towards a perfect day in the lab.

I deeply thank everybody who was part of this experience. Foremost I am very grateful to our amazing group leader Rodrigo Lopez-Martens, who integrated me into his friendly team. He managed to create a stimulating environment while allowing enough freedom for one's own interests. He also allowed me to interact globally with the scientific community around the world, while presenting our work at different conferences. This has really given me the perspective to judge the importance of our work and to see it in the context of the fast-evolving, ultrafast-optics community.

A year before I started my PhD work, I had joined the lab to perform the experimental work for my Master's degree at the Technical University Munich. Back then, Aurelie Jullien was still part of the group, but has since then moved to the sunny side of France. It was really her, who introduced me to all the experimental techniques in the lab and I owe her a very important debt. I could always count on her vast understanding of femtosecond lasers and non-linear optics, and it was a great pleasure to work with her.

I also had the fortune to spend many evenings in the lab together with Maimouna, a former PhD student of the group. While tackling the mood of the laser, or demystifying the solid target, there was always enough positive optimism to try again and again to get the sought-after results. And I can truly state that my results would have never been possible without her. In the lab, we were just the perfect team with an ideal composition of *German engineering* and *French creativity.* Thanks for all this experience.

Looking back on all those years, I really come to appreciate the amazing teamwork and atmosphere in our group PCO and close partner group APPLI. So I would like to thank all present and past members for so many fruitful discussions and joyful moments. In particular: Aline, Benoît, Diego, Dominykas, Hermance, Isabel, Jean-Baptiste, Jean-Philippe, Jérome, Magalie, Marie, Maxence, Natalia, Neil, Olivier and Stefan.

Thanks also to all the other colleagues at the LOA. The LOA is an excellent institute that can only function so well through the seamless help of the secretary and the mechanical workshop. Even though my request were sometimes not the easiest, I could always count on them. In particular I would like to thank Jean-Lou Charles from the mechanical workshop for the pride he took in machining the parts with absolute precision and perfect finish. Something that is so important with state of the art research.

Over time we had the opportunity for many rewarding collaborations. In particular I would like to thank: François Sylla and Cedric Sire from SourceLAB; Martin Kretschmar, Andreas Blumenstein, Tamas Nagy and Peter Simon from the Laser-Laboratorium Göttingen e.V; Francisco Silva, Rosa Romero and Helder Crespo from Sphere Ultrafast Photonics; Fabien Quéré from the CEA; Máté Kovács from ELI-HU.

This all would not have been possible without the strong support from my friends and family. My parents did an incredible job raising me. Marie-Theres and Gregor, you have always believed in me and allowed me to freely pursue my own interests. Thank you for letting me live my dreams. My late brother Lukas, and my younger siblings Franziska and Julius made growing up so enjoyable and I feel very lucky for the strong bonds that keep us together.

Only two people left to thank - last but not least - you are simply the most important parts of my life. To my wonderful wife Marta, I feel so fortunate having found each other. Our journey together turned out to be so amazing. Cannot wait to see, where it will still take us. Out of this love came our son Jan Leon, and his smile, still inside the warm belly, gave me the last push to finish my PhD. Thanks :-)

Acronyms

AOPDF acousto-optic programmable dispersive filter

ASE amplified spontaneous emission

BSI barrier-suppression ionization

CEP carrier envelope phase

CM chirped mirror

CPA chirped pulse amplification

CWE coherent wake emission

FDI frequency domain interferometry

FOD fourth-order dispersion

FROG frequency resolved optical gating

FT Fourier transform

FTL Fourier transform limited

FWe2 full width at $1/e^2$

FWHM full width at half maximum

GDD group delay dispersion

HCF hollow-core fiber

HHG high-harmonic generation

ID inner-core diameter

MCP micro-channel plate

MPI multi-photon ionization

NLSE nonlinear Schrödinger equation

PIC particle-in-cell

PSD position sensitive detector

QWP quarter-wave plate

ROM relativistically oscillating mirror

SDI spatial domain interferometry

SHG second harmonic generation

HHG solid high-harmonic generation

SPM self-phase modulation

STC spatio-temporal coupling

TGC transmission-grating compressor

TOD third-order dispersion

VLA vacuum laser acceleration

WFR wavefront rotation

XPW cross-polarized wave

XUV extreme ultraviolet (10 nm - 124 nm)

Abstract

Very short light pulses allow us to resolve ultrafast processes in molecules, atoms and matter. This started with the advent of femtochemistry, for which Ahmed Zewail received the Nobel Prize in Chemistry in 1999. Ever since researcher have been trying to push the temporal resolution further and we have now reached attosecond pulse durations. But their generation remains very challenging and various different mechanisms are the topic of heated research around the world.

Our group at the LOA focuses on attosecond pulse generation on plasma mirrors in the relativistic regime. For this a high intensity, high contrast and high repetition-rate femtosecond laser chain is being developed to reach relativistic intensities ($\gg 10^{18}\,\mathrm{W/cm^2}$) when focused onto an overdense plasma (solid target). An overdense plasma reflects the incoming light and acts like a mirror that oscillates with a relativistic velocity. This periodically compresses and stretches the incident light field and thus creates an attosecond pulse every optical cycle. In using few-cycle driving laser pulses it should be possible to only generate a single attosecond pulse during the interaction.

During the first part of my PhD, I implemented a nonlinear compressor to reduce the duration of CEP stable laser pulses coming from a double CPA laser system based on traditional Ti:Sapphire amplifiers. While propagating these high intensity, but many cycle laser pulses through a gas filled wave-guide (HCF), I was able to compress them to near-single-cycle duration (3.5 fs) and increase their peak intensity to 1 TW while maintaining controlled CEP. During the second part, I controlled their spatio-temporal characteristics in a vacuum beamline to precisely drive relativistic high-harmonic-generation on solid targets. It was the first time ever that this has been achieved at 1 kHz repetition rate. By CEP gating the few-cycle-pulses, single attosecond pulses were generated. The conclusion has been supported by numerical simulations. Additionally a new regime to accelerate electron bunches on soft gradients has been detected.

Résumé

Les impulsions laser ultra-brèves nous permettent de suivre en temps réel les phénomènes ultrarapides au sein de la matière à l'échelle microscopique. C'est précisément pour l'invention de la chimie à l'échelle femtoseconde, ou femtochimie, qu'Ahmed Zewail se vit décerner le prix Nobel de chimie en 1999. Depuis les utilisateurs du laser cherchent à augmenter la résolution temporelle, c'est-à-dire réduire la durée des impulsions laser. Aujourd'hui, nous savons générer des flashs lumineux à l'échelle attoseconde dans le domaine spectral de l'extrême ultraviolet (XUV) mais l'efficacité de génération reste faible et le développement de sources laser attosecondes intenses constitue un sujet de recherche très actif sur le plan international.

Notre groupe au LOA se concentre sur la génération d'impulsions attoseconde sur miroir plasma en régime relativiste. Pour cela, il cherche à développer une source d'impulsions femtosecondes à forte cadence et fort contraste et suffisamment énergétiques pour atteindre des intensités relativistes ($\gg 10^1 8\,\mathrm{W/cm}^2$) lorsqu'elles sont fortement focalisées sur un plasma surdense. Un plasma surdense réfléchit la lumière incidente et par conséquent agit comme un miroir qui se déplaçant à vitesse relativiste et qui comprime l'impulsion incidente, produisant ainsi un flash attoseconde par cycle optique. En utilisant des impulsions proches d'un cycle optique, il est donc envisageable de générer une seule impulsion attoseconde intense pendant l'interaction.

Dans la première partie de mon travail de thèse, j'ai réalisé un compresseur non-linéaire pour réduire la durée des impulsions issues d'une chaîne à double dérive de fréquence (10mJ, 25fs, 1kHz) à phase enveloppe-porteuse (CEP) stabilisée. En propageant les impulsions du laser à haute intensité dans une fibre creuse remplie de gaz rare, j'ai réussi à générer des impulsions de 1.3 cycle optique avec une puissance crête autour de 1TW avec une CEP stabilisée. Dans un deuxième temps, j'ai mis en forme spatialement et temporellement les impulsions issues du compresseur à fibre pour générer à la fois des impulsions attosecondes intenses et des faisceaux d'électrons énergétiques sur un miroir plasma à gradient de densité contrôlé. Ces expériences nous permis, pour la première fois, de mettre en évidence la production d'impulsions attosecondes isolées dans l'XUV, l'émission corrélée de

faisceaux d'électrons énergétiques en régime relativiste ainsi qu'un nouveau régime d'accélération d'électrons à très long gradient plasma.

Le premier chapitre de ce manuscrit décris le sujet de cette thèse qui est de générer des impulsions de lumière ultra court pour suivre en temps réel des phénomènes ultrarapides. Afin de visualiser la durée des événements en question (d'ordre d'attoseconde et plus court), une échelle temporelle montrant des événements quotidiens est présentée. La spectroscopie attoseconde et la diffraction électronique femtoseconde sont deux candidats prometteurs pour tracer ces événements courts. Les deux sources peuvent être générer par une interaction laser-plasma surdense.

Afin d'aider de comprendre les propriétés importantes du laser et des interactions laser-plasma, une brève introduction mathématique est donné dans le deuxième chapitre.

La première parti présente des modifications d'une chaine laser afin d'avancer dans le régime relativiste sur un miroir plasma. Le Chapitre 3 présente des exigences principales du laser et ses défis technologiques. Des solutions sont proposées et évaluées dans leur contexte scientifique.

Chapitre 4: Le problème de contraste d'un système laser traditionnel a été résolu grâce à un système double CPA. Un filtre non-linéaire entre les deux CPAs améliore le contraste temporel pendant que le deuxième CPA permet la récupération d'énergie. Cela devrait permettre d'atteindre des intensités relativistes au foyer sans pré-ioniser la cible.

Dans le Chapitre 5 le schéma d'un compresseur à fibre creuse à haute énergie est développé afin d'atteindre le régime de quelques cycles optiques. Grâce à la combinaison des trois améliorations distinctes la puissance maximale du laser atteint le niveau d'un TW.

Chapitre 6: Afin de délivrer précisément des impulsions femtoseconde de quelque cycle optique sur une cible solide, une ligne de faisceaux sous vide était développée. La caractérisation du laser est également faite sous vide pour un résultat le plus précis possible.

La deuxième partie de la thèse parle de l'interaction laser-plasma en utilisant la chaine laser améliorée. Une introduction brève sur l'interaction laser-plasma est donnée au Chapitre 7, suivie d'un aperçu de deux mécanismes principaux de génération d'harmoniques sur une cible solide. Les propriétés distinctes de chaque de ces mécanismes sont présentées.

Des expériences d'interaction laser-plasma à haute cadence sur une cible solides exige un énorme effort afin d'assurer les conditions expérimentales stable et les diagnostics fiable. Dans le Chapitre 8 des moyens expérimentaux pour la génération harmoniques sont présentés.

Le Chapitre 9 montre la génération des harmoniques sur une cible solide en régime relativiste pour la première fois au kHz. Ce résultat est complété par la production d'impulsions attosecondes isolées dans l'XUV. Il est suivi de la démonstration de l'émission corrélée de faisceaux d'électrons énergétiques en régime relativiste ainsi qu'un nouveau régime d'accélération d'électrons à très long gradient plasma.

Contents

1. Introduction

We humans visualize the world on a very specific timescale. For transformations or motions in general that evolve over a long time we cannot perceive the changes directly. A flower for example, does not seem to be changing much when we look at it with our naked eye. Only with time-lapse photography, we can create a movie of the changes and play it back at a much faster pace. Then suddenly we can visualize the growing process.

This is similar towards the other end of the timescale, to every shorter processes. To see how the wings of a fly move we need a high speed video cameras, take thousands of frames per second, and then play it back at a much lower pace.

In fact we can only recognize a tiny fraction out of all the natural processes that take as long as the age of the universe ($4.5 \cdot 10^{17}$ s) down to as short as the atomic unit of time ($2.4 \cdot 10^{-17}$ s) or shorter. The fraction we can visualize is around the centre of this vast scale. It is not surprising that our heart rate of around $1\,\mathrm{s}^{-1}$ serves as a reference.

The different processes that take place on this shorter part of the timescale are shown in Figure 1.1 represented by pictograms on the bottom. But to understand their motion, we need to resolve it. Many advances in science are achieved with new techniques to image ever shorter processes (shown at the top of Figure 1.1). Atoms and molecules for example vibrate down to the femtosecond timescale. New technologies to resolve this motion has created a complete new domain a few decades ago, which is called femtochemistry. For his pioneering contribution Ahmed Zewail has been awarded the 1999 Nobel Prize in Chemistry.

Further down are the electron dynamics in atoms, molecules or solid state matter, which happens on the attosecond timescale. Again a complete technological breakthrough was required. And currently there are 2 potential sources for resolving these ultrafast dynamics in matter. There is the ultrafast electron diffraction and attosecond spectroscopy. Both are quite similar to the pump-probe experiments in Femtochemistry. The first uses as a probe an electron bunch of a few fs in duration and the latter attosecond light pulses.

---

[1] Pictogram sources: Stopwatch: dtjohnnymonkey, public domain; Camera: Vision Research; Flashlamp: Gregory Maxwell, GFDL 1.2; Oscilloscope: Good Will Instrument; Laser: Continuum Lasers; Heart: Josinho8, public domain; Fly: Deora et al. PNAS 112, 1481–1486 (2015); Apple: Harold Edgerton; CPU die: Intel; Atom: GFDL; Plasma: Simulation from Vincenti et al. Nat. Commun. 5, 3403 (2014)

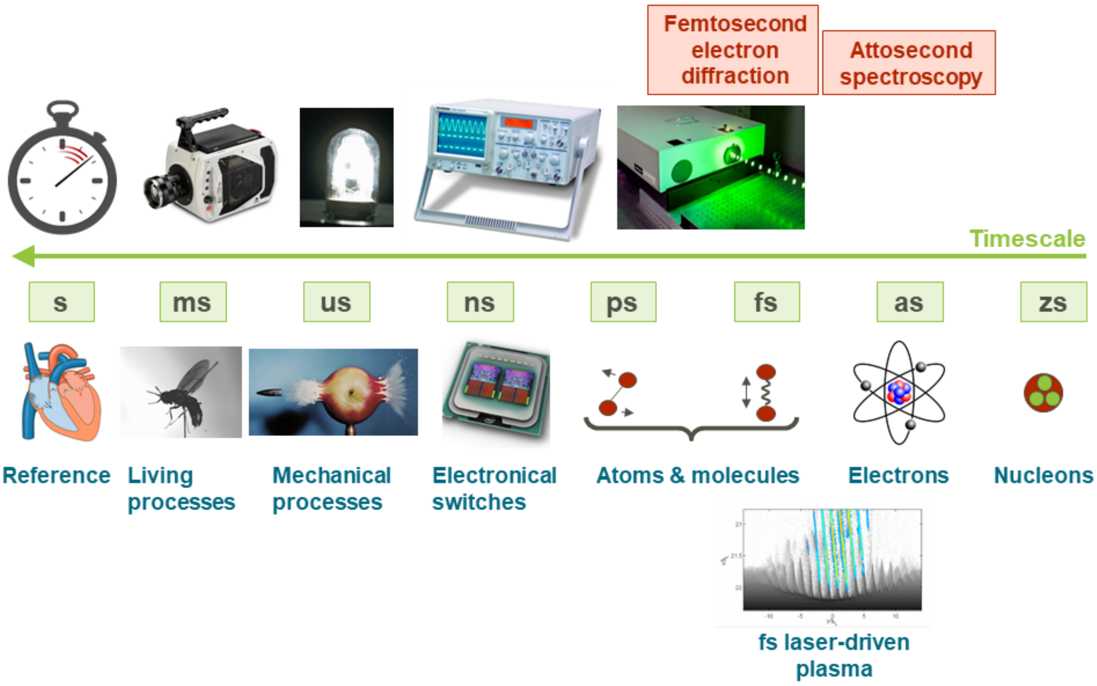

Figure 1.1. Visualization of different timescales from seconds to zepto seconds (10^{-21} s) by typical processes and typical measurement techniques. Pictograms from various sources[1].

The electron dynamics of a laser-plasma interaction happen also on these short timescales and they can be an efficient source of attosecond pulses and ultrashort electron bunches. But to use it efficiently we need to understand and control the collective plasma electron dynamics on a femto- to attosecond timescale. Intense femtosecond laser pulses are of course ideal for this and can be used both for a convenient probe as well as a driver.

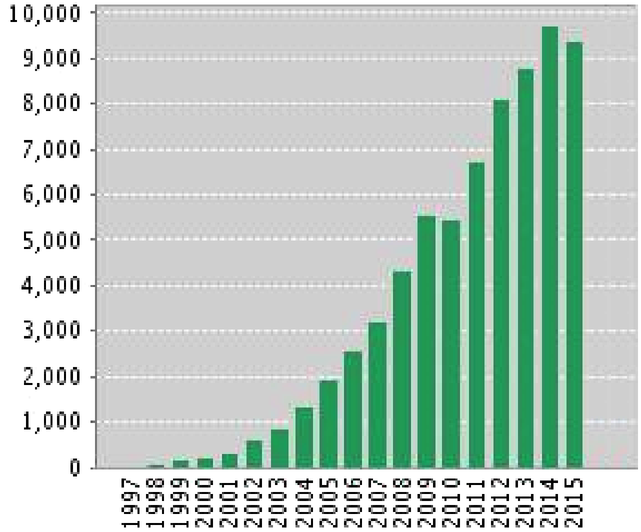

Figure 1.2. Number of citations per year on the topic of *attosecond*. Soure: Web of Science; webofknowledge.com

Attosecond spectroscopy is a fast growing field. If we look at the number of citations per year, we see an exponential like growth (Figure 1.2). Creating the attosecond pulses is on the other hand not so easy. They require an extremely large spectral bandwidth. From Fourier analysis we know that the shorter the pulse, the broader the spectrum has to be. Actually the full visible spectrum is not enough to create sub femtosecond light pulses. Instead we need to reach into the XUV range, which spans across a much larger bandwidth.

In this spectral range, attosecond pulses can be created through high-harmonic generation (HHG). The first attosecond pulses have been observed in 2001 [1, 2]. Those pulses have been generated inside a gas medium. Our group on the other hand focuses on solid density plasmas, which are potentially able to deliver much stronger attosecond pulses.

A plasma is one of the four states of matter. It seems a bit like an ionized gas, where at least a part of the electrons are dissociated from the atoms and move freely around. A plasma can easily be created by strong lasers, where the laser electric field completely deforms the atom's Coulomb potential to free the electrons.

Consisting of charged particles, a plasma couples strongly to electromagnetic waves. At low frequencies and intensities it behaves like a conductor and just reflects an incident wave hitting a vacuum-plasma interface. Towards higher intensities the electrons are accelerated and a highly complex nonlinear behaviour appears, where one needs to model the collective electron dynamics to understand the process.

These dynamics can be used to efficiently compress an intense incident light field. We use fused silica surfaces that quickly turn into a plasma from the rising edge of the laser pulse. The laser has a duration of only a few femtoseconds and is focused down to extremely high intensities ($> 10^{18}\,\mathrm{W\,cm^{-2}}$). These high intensities accelerate the electrons to relativistic velocities. Under proper condition, attosecond pulses can be generated.

But to do this, we first need to have a laser, suitable for these highly demanding solid-plasma experiments. Our group has chosen to do both. That is laser development and its applications in plasma physics. The design approach for our laser chain is to source existing components from the industry, and put our own development efforts in novel techniques, sometime also in collaboration with industrial partners. This has allowed us to efficiently build a whole laser chain and beamline for our experiments.

Lasers have come a long way since their first invention in 1960 by Theodore Maiman. Contrary to the public conception, lasers are often used in a mode where they emit pulses of light. This allows to reach higher intensities, while keeping the average power low (Figure 1.3). The laser field got so strong nowadays, that electrons inside the field start to quiver with relativistic velocities. This is called the relativistic regime for laser plasma interactions.

Three key technological breakthroughs have pushed the limit further. Q-switching inside a laser cavity could release in a very short time the accumulated energy in the lasing crystal. This gives short and high energy pulses. Mode-locking allowed even shorter pulse duration down to a few femtoseconds. But it was note before the last crucial milestone that the laser field could become comparable to the coulomb potential for bound electrons. Chirped pulse amplification (CPA) stretches the pulse before amplification so the laser crystal does not get damages from the high field strength. After amplification the stretching is reversed and a much higher peak power achieved (Figure 1.4) [4].

Relativistic laser intensities are now commonly obtained. High fidelity, high-repetition-rate lasers for solid targets on the other hand are still on the edge of state of the art technology. This becomes clear throughout the first part of my PhD.

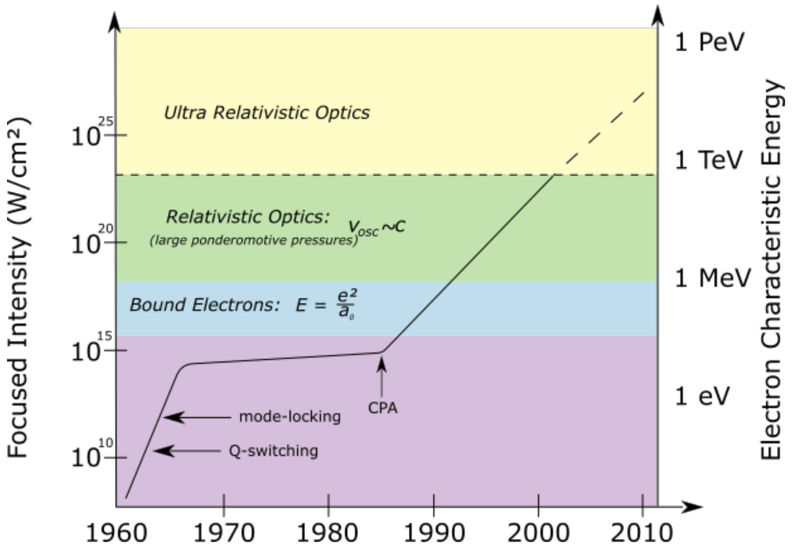

Figure 1.3. Chronology of highest laser intensity in focus by year. Displayed together with the characteristic electron energy inside the laser field. This indicates the regime of operation for a laser plasma experiment (colour background). The development has been accelerated by three key technological milestones indicated by arrows. Reprinted from [3]

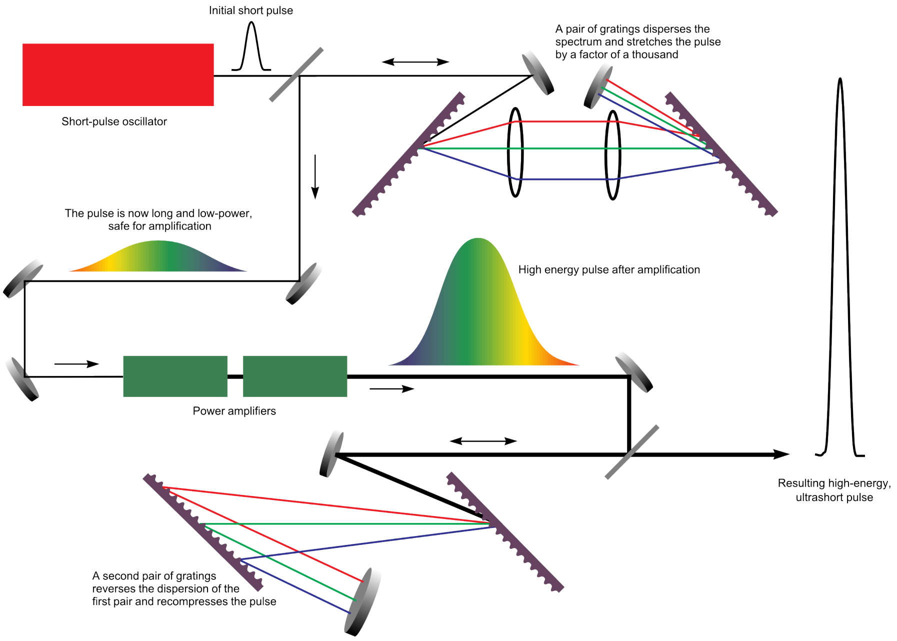

Figure 1.4. Concept behind a CPA system, where the pulse is stretched before being amplified and recompressed again. Reprinted from [5]

2. Mathematical Background and Formalism of Laser Physics

Let me lay the base for all further mathematical description by starting with Maxwell's equations. I imagine practically every dissertation in optics touches this set of four equations at some point or another. They got introduced in the second half of the 19th century by James Clerk Maxwell and unified the magnetic and electric fields into a common understanding of electromagnetism. It is of particular pleasure, that these equations will be the base for both parts of this thesis, spanning from low field intensities of linear and nonlinear optics to the high field physics regime that drives relativistic light compression and particle acceleration. In its most general form they are written as:

$$\begin{aligned} \nabla \cdot \vec{E} &= \frac{\rho}{\epsilon_0} \qquad & \nabla \times \vec{E} &= -\frac{\partial \vec{B}}{\partial t} \\ \nabla \cdot \vec{B} &= 0 \qquad & \nabla \times \vec{B} &= \mu_0 \vec{J} + \mu_0 \epsilon_0 \frac{\partial \vec{E}}{\partial t} \end{aligned} \tag{2.1}$$

The electric ($\vec{E}$) and magnetic ($\vec{B}$) fields can be defined by the Lorentz force they impose on a test charge q.

$$\vec{F} = q\left[\vec{E} + \vec{v} \times \vec{B}\right] \tag{2.2}$$

In Maxwell's equations we see that fields can be either generated by charges (ρ) and currents ($\vec{J}$) or self-sustainingly by changing field strength $\frac{\partial \vec{B}}{\partial t}$ or $\frac{\partial \vec{E}}{\partial t}$. This cross-relation between the electric and magnetic field leads to propagating oscillating waves, where the propagation speed is derived from the *feedback* constant $\mu_0\epsilon_0$. And in vacuum ($\rho = 0;\ \vec{J} = 0$), solving the two coupled differential equations

$$\begin{aligned} \nabla \times \nabla \times \vec{E} &= -\nabla \times \frac{\partial \vec{B}}{\partial t} \\ &= -\mu_0 \epsilon_0 \frac{\partial^2 \vec{E}}{\partial t^2} \end{aligned} \tag{2.3}$$

leads to a wave-equation

$$\nabla^2\vec{E} - \frac{1}{c^2}\frac{\partial^2\vec{E}}{\partial t^2} = 0 \tag{2.4}$$

with $c = \frac{1}{\sqrt{\mu_0\epsilon_0}}$ being the propagation speed. This of course changes in the presence of charges and we will develop in Section 2.1 the necessary understanding of linear and nonlinear optics by looking at electromagnetic wave propagation, assuming non-magnetic media without free charges. Then in Section 2.2 we will treat how intense laser fields interact with a plasma, i.e. with only free charges and currents.

2.1. Electromagnetic waves in linear and nonlinear optics

Solving Maxwell's equations inside a material with the complex response of bound electrons would be overwhelming. It can be therefore convenient to rewrite Maxwell's equations from a macroscopic viewpoint and as such hide the influence of bound electrons behind a more abstract definition. For this we separate the free charges from the bound charge distribution of the material:

$$\rho = \rho_f + \rho_b \tag{2.5}$$

Inserting this into Maxwell's equations we get

$$\nabla \cdot \epsilon_0\vec{E} - \rho_b = \rho_f \tag{2.6}$$

And we can define an auxiliary field $\vec{D}$

$$\vec{D} := \epsilon_0\vec{E} + \vec{P};\ \text{with } \nabla \cdot \vec{P} := -\rho_b \tag{2.7}$$

where $\vec{P}$ is called the polarization field. So Equation (2.6) becomes

$$\nabla \cdot \vec{D} = \rho_f \tag{2.8}$$

The charge distribution of the material represented by the polarization field is in general complex, but we will see later, that one often can establish a linear or polynomial relation between $\vec{D}$ and $\vec{E}$.

We can very similarly separate the current distribution by

$$\vec{J} = \vec{J}_f + \vec{J}_b \tag{2.9}$$

and inserting also into Maxwell's equations

$$\begin{aligned} \nabla \times \vec{B} &= \mu_0 \left(\vec{J}_f + \vec{J}_b \right) + \mu_0 \frac{\partial \vec{D} - \vec{P}}{\partial t} \\ \Leftrightarrow \qquad \frac{1}{\mu_0} \nabla \times \vec{B} - \vec{J}_b + \frac{\partial \vec{P}}{\partial t} &= \vec{J}_f + \frac{\partial \vec{D}}{\partial t} \end{aligned} \tag{2.10}$$

leads us to the auxiliary field $\vec{H}$

$$\vec{H} := \frac{1}{\mu_0} \vec{B} - \vec{M}; \text{ with } \nabla \times \vec{M} := \vec{J}_b - \frac{\partial \vec{P}}{\partial t} \tag{2.11}$$

where $\vec{M}$ is called the magnetization field. So Equation (2.10) becomes

$$\nabla \times \vec{H} = \vec{J}_f + \frac{\partial \vec{D}}{\partial t} \tag{2.12}$$

Free charges and currents only occur if the electric field gets strong enough to ionize the material - a condition generally undesirable in optics as it destroys the material. We will see in Chapter 5 however, that it does happen in the case of nonlinear optics in gases. Thus we simplify further by $\rho_f = 0$; $\vec{J}_f = 0$. This leads us to the simplified Maxwell's equations where the material response is hidden inside D and H.

$$\begin{aligned} \nabla \cdot \vec{D} &= 0 \qquad & \nabla \times \vec{E} &= -\frac{\partial \vec{B}}{\partial t} \\ \nabla \cdot \vec{B} &= 0 \qquad & \nabla \times \vec{H} &= \frac{\partial \vec{D}}{\partial t} \end{aligned} \tag{2.13}$$

Also, magneto-optic effects, even though an interesting field with applications also used in our laser chain (Faraday effect, etc.), will not be considered and only non-magnetic media are treated ($\vec{H} = \frac{1}{\mu_0} \vec{B}$).

When now solving the two inhomogeneous differential Maxwell's equations we get an additional source term (following [6, chapter 2])

$$\nabla^2 \vec{E} - \frac{1}{c^2} \frac{\partial^2 \vec{E}}{\partial t^2} = \frac{1}{\epsilon_0 c^2} \frac{\partial^2 \vec{P}}{\partial t^2} \tag{2.14}$$

It is helpful to develop the polarization in a power series of the E-field to distinguish between linear and nonlinear material responses. This is technically only true under the assumption of monochromatic waves ($\chi(\omega)$), but it nonetheless provides an intuitive insight.

$$\vec{P} = \epsilon_0 \left(\chi^{(1)} \cdot \vec{E} + \chi^{(2)} \cdot \vec{E}^2 + \chi^{(3)} \cdot \vec{E}^3 + \cdots \right) \tag{2.15}$$

with $\chi^{(n)}$ being the nth-order susceptibility tensor of rank $n+1$. In an isotropic material, for example, the linear susceptibility is just a scalar and relates to the refractive index $n = \sqrt{1+\chi^{(1)}}$. Also, as there cannot be any favoured direction, $\chi^{(2)}$ needs to be zero, which means that no nonlinear effect of order two can occur.

2.1.1. Ultrashort pulses

This thesis deals with ultrashort pulses of electromagnetic waves that exhibit only a few oscillations. Naturally, from the uncertainty principle, the photons, while being well defined in their temporal position, must have a large uncertainty in their energy, i.e. they have a very large spectrum. But as the refractive index of all materials is frequency dependent, different parts of the spectrum travel with different group velocities. This leads to a stretching of the pulse, which lowers in turn the intensity. Just looking at the temporal description of laser pulse we can separate the electric field into a real valued amplitude and a complex oscillating part:

$$\vec{E}(t) = \vec{E}_0(t) \cdot \exp(-i\phi(t)) \tag{2.16}$$

where $\phi(t)$ is called the temporal phase. The actual observable electric field needs to be of course a real valued quantity:

$$\vec{\mathcal{E}}(t) = \frac{1}{2}\vec{E}(t) + cc. \tag{2.17}$$

though this technical detail will be overlooked in this thesis.

E_0 relates to the shape of the pulse, i.e. the temporal intensity profile. The instantaneous flow of electromagnetic power is given by the Poynting vector:

$$\vec{S} = \frac{1}{\mu_0}\vec{E} \times \vec{B} \tag{2.18}$$

Whereas the intensity of a laser pulse is defined as a time-averaged quantity – averaged over a time longer than the field oscillations, but short enough for the timescale of interest. This leads to:

$$I(t) = \frac{1}{2\eta} \cdot |E(t)|^2 \tag{2.19}$$

with $\eta = \sqrt{\mu_0/\epsilon}, \epsilon = \epsilon_0 \cdot (1 + \chi^{(1)})$.

A common pulse shape is described by a Gaussian function:

$$I(t) = I_0 \cdot \exp(\frac{t^2}{2 \cdot \tau^2}) \tag{2.20}$$

To describe the shape of a pulse we define a temporal width by the mean square deviation (pulse centred around $t = 0$):

$$\sigma_\tau^2 = \frac{\int_{-\infty}^{\infty} t^2 I(t)}{\int_{-\infty}^{\infty} I(t)} \tag{2.21}$$

For a Gaussian profile this is identical to the τ parameter in Equation (2.20) and relates to its full width at half maximum (FWHM) as $\tau_{\mathrm{FWHM}} = 2\sqrt{2\ln 2} \cdot \sigma_\tau$ and to the full width at $1/e^2$ (FWe2) as $\tau_{\mathrm{FWe2}} = 4 \cdot \sigma_\tau$.

Also the temporal phase $\phi(t)$ has some important and intuitive properties. Let us first decompose the phase:

$$\phi(t) = \phi_0 - \omega_0 \cdot t + \phi_{NL}(t) \tag{2.22}$$

ω_0 is the carrier frequency with which the field oscillates. ϕ_0 is the temporal offset from the field maxima to the envelope peak, which is visualized in Figure 2.1. The carrier envelope phase (CEP) value for a many-cycle pulses is rather of academic value, as the neighbouring peaks have similar field strength and a physical process would not be sensitive to a change in CEP. But in the case of few-cycle pulses this could mean that electrons, which are ripped of an atom only during the strongest field peak, get accelerated either to one side or the other, depending on the sign of this peak.

The nonlinear part ϕ_{NL} leads to a change in instantaneous frequency over the duration of the pulse, for example a linear chirp $\phi_{NL}(t) = a \cdot t^2$, lead to a linear rising frequency. But we will ultimately come back to this in the spectral description of light pulses.

Description in the spectral domain

So far we talked about the temporal variation of the electric field, but a description in the spectral domain via Fourier transform (FT) is equally correct and complete. For this we decompose the oscillating field into overlaying monochromatic waves with a given phase offset. In linear optics these monochromatic waves can then be treated separately during propagation and give an easy understanding of how a material affects the pulse shape. For this we define the spectral amplitude by the FT:

$$\tilde{E}(\omega) = \frac{1}{\sqrt{2\pi}} \int_{-\infty}^{\infty} E(t) \cdot \exp(-i\omega t)\,\mathrm{d}t \tag{2.23}$$

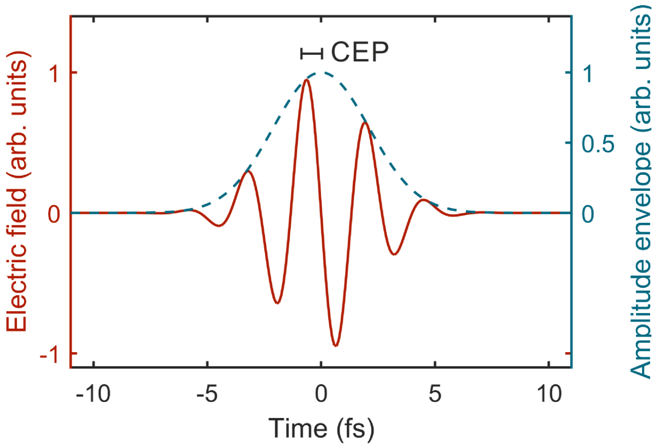

Figure 2.1. Electric field of a few-cycle laser pulse where the field oscillations are shifted relative to the pulse envelope by the CEP.

This can be again separated into a real spectral amplitude $A(\omega)$ and a complex term of unitary length.

$$\tilde{E}(\omega) = A(\omega) \cdot \exp\left(i\varphi(\omega)\right) \tag{2.24}$$

with $A(\omega) := \left|\tilde{E}(\omega)\right|$.

One can once again define an intensity in accordance to Parseval's theorem:

$$\tilde{I}(\omega) = \frac{1}{2\eta}\left|\tilde{E}(\omega)\right|^2 \tag{2.25}$$

and a spectral width

$$\sigma_\omega^2 = \frac{\int_{-\infty}^{\infty} \omega^2 \tilde{I}(\omega_0 + \omega)}{\int_{-\infty}^{\infty} \tilde{I}(\omega)} \tag{2.26}$$

The temporal and spectral width are related through the uncertainty principle by the following inequality:

$$\sigma_\tau \cdot \sigma_\omega \geq \frac{1}{2} \tag{2.27}$$

in practice it is usually more convenient to use FWHM values for which an inequality equation is dependent on the pulse form. Anyway the inequality relation turns to equality for a Gaussian profile with a flat phase. We can see this by Fourier transforming the temporal pulse shape of Equation (2.20) under the assumption of a flat phase. By doing so we get again a Gaussian function:

$$\tilde{I}(\omega) = \tilde{I}_0 \cdot \exp\left(\frac{(\omega-\omega_0)^2}{2\cdot\sigma_\omega}\right) \tag{2.28}$$

with $\tilde{I}_0 = I_0 \cdot 2\tau^2$ and $\sigma_\omega = \frac{1}{2\tau}$.

The phase of Equation (2.24) is best developed into a Taylor series around the central frequency ω_0:

$$\varphi(\omega) = \varphi_0 + \varphi^{(1)} \cdot (\omega - \omega_0) + \frac{\varphi^{(2)}}{2} \cdot (\omega - \omega_0)^2 + \frac{\varphi^{(3)}}{6} \cdot (\omega - \omega_0)^3 + \cdots \tag{2.29}$$

with $\varphi_n = \frac{\mathrm{d}^n\varphi}{\mathrm{d}\omega^n}|_{\omega_0}$. φ_0 relates again to the CEP, while the second term describes the group delay. The envelope of a light pulse travels at the group velocity v_g:

$$v_g = \frac{\partial\omega}{\partial k} \tag{2.30}$$

We see then directly that the second term $\varphi^{(1)}$ corresponds to the group delay, that means simply a delay in time of the pulse envelope relative to a given reference. This is in general not of interest.

The next term $\varphi^{(2)}$ is called the group delay dispersion (GDD) or chirp, which describes that the different spectral parts of the pulse travel at different velocities. In fact there is a linear group delay versus frequency relation. This type of pulse degradation leads to a longer pulse than what could be obtained from the spectral bandwidth. An example of a chirped pulse is shown Figure 2.2 a, where the 'red' part of the spectrum arrives before the 'blue' part. The broader the spectrum, the stronger the influence of GDD is. A 3.5 fs (at 800 nm) pulse travelling through only 1 mm of glass will be stretch already to 29 fs, so an eight times increase. On the other hand a 25 fs long pulse stretches only by 1.3% of its original duration.

The higher order phase terms $\varphi^{(3)}$ etc. lead to a pulse distortion. $\varphi^{(3)}$ or also called third-order dispersion (TOD) leads, for example, to the generation of pre- or post-pulses as seen in Figure 2.2 b.

When an optical pulse travels through a dispersive $n(\omega)$ medium of length L, it acquires the following spectral phase:

$$\varphi(\omega) = \frac{n(\omega)}{c} \cdot \omega \cdot L \tag{2.31}$$

2.1.2. Nonlinear optics

Until now we only discussed how material propagation affects the pulse in the case of a linear polarization relation, i.e. the light field was sufficiently weak. In that case higher order terms in the polarization did not weight in. At stronger light fields this is no longer the case and we must treat higher order polarization effects

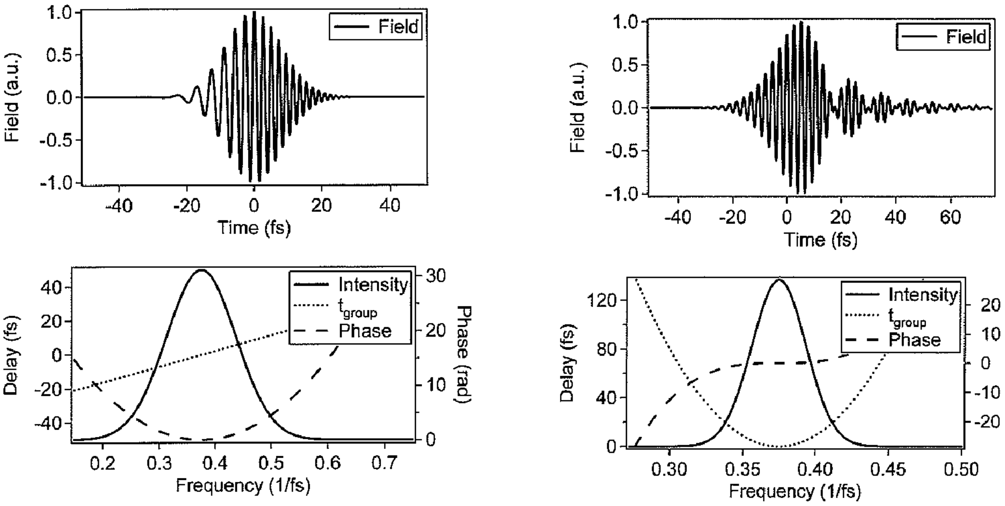

Figure 2.2. Effects on the pulse shape coming from a quadratic (pure GDD, left) or cubic (right) spectral phase. Reprinted from [7]

in growing order. Let us assume the following wave (after [6, chapter 1]):

$$E(t) = E_1 \cdot \exp(-i\omega_1 t) + E_2 \cdot \exp(-i\omega_2 t) \tag{2.32}$$

consisting of two frequencies ω_1 and ω_2. If this wave propagates through an anisotropic medium with a non-vanishing second order nonlinear susceptibility, this contributes to the overall polarization by:

$$\begin{aligned} P_2(t) = \epsilon_0 \chi^{(2)} \cdot \Big[& E_1^2 \cdot \exp(-i(2\omega_1)t) \\ & + E_2^2 \cdot \exp(-i(2\omega_2)t) \\ & + 2E_1E_2 \cdot \exp(-i(\omega_1 + \omega_2)t) \\ & + 2E_1E_2^* \cdot \exp(-i(\omega_1 - \omega_2)t) \\ & + 2E_1E_1^* + 2E_2E_2^* \Big] \end{aligned} \tag{2.33}$$

We see here that new frequencies ($\omega_1 + \omega_2$, $2\omega_1$, etc.) are *generated*, i.e. the polarization oscillates at previously not present frequencies. This in turn will lead to the generation of new frequencies through the wave equation (Equation (2.14)). As the initial electric field contributes quadratically to the polarization, this conversion process will also scale quadratically in intensity. For a third order nonlinear process cubically and so on. This effect will be exploited in the nonlinear pulse cleaning device (XPW) in the middle of our laser chain, where the temporal profile of the pulse gets filtered by taking the cube of the input signal.

Another concrete example is the intensity dependent refractive index:

$$n = n_0 + n_2 \cdot I \tag{2.34}$$

This is a third order process, in which $(\omega + \omega - \omega)$ contribute to the polarization at the fundamental frequency and therefore changing the refractive index with the intensity profile of the pulse. This leads to an instantaneous frequency shift and therefore a spectral broadening, which will be exploited in the post-compression setup detailed in Chapter 5.

2.2. Maxwell's equation in a laser-plasma interaction

In a plasma we will make a similar simplification to screen the microscopic behaviour of the particles and treat it as collision-less. That means in a sense neglecting the microscopic fields around the particles that lead to scattering and only treat the field, averaged over a certain distance. We will also assume that the plasma is unmagnetized and non-relativistic. The plasma is described by the charge density ρ and the current density $\vec{J}$ for the electrons and ions. But the particles are free to move and are accelerated by the electromagnetic fields. And for the full description one would need to solve $6 \cdot N$ coupled differential equations. The fluid model reduces this complexity by not looking at individual particles but instead describes the plasma with macroscopic averaged quantities like density, mean velocity, temperature, etc. Also, the ions and electrons have a largely different mass and behave therefore on very different time-scales. It makes it easier to describe each particle class with their own fluid type. We reach the two-fluid description of a plasma with the continuity equation (after [8]):

$$\frac{\partial n_j}{\partial t} + \nabla \cdot (n_j \cdot \vec{v}_j) = 0 \tag{2.35}$$

and the fluid equation:

$$n_j \left(\frac{\partial \vec{v}_j}{\partial t} + \vec{v}_j \nabla \cdot \vec{v}_j \right) = \frac{n_j q_j}{m_j} \left(\vec{E} + \frac{\vec{v}_j \times \vec{B}}{c} \right) - \frac{1}{m_j} \cdot \nabla p_j \tag{2.36}$$

for each particle type j with charge q_j, mass m_j, density n_j, pressure p_j and mean velocity $\vec{v}_j$.

From these equations one can obtain two plasma wave solutions, the electron plasma waves and the ion acoustic waves. The plasma waves are oscillating essentially at the plasma frequency:

$$\omega_p = \sqrt{\frac{e^2 n_e}{m_e \epsilon_0}} \tag{2.37}$$

plus a small correction depending on the wave number (n_e electron density).

Together with Maxwell's equations one can derive the propagation of electromagnetic waves in a plasma that leads to the dispersion relation:

$$\omega^2 = \omega_p^2 - k^2 c^2 \tag{2.38}$$

and we see that for frequencies above the plasma frequency the wave becomes evanescent with k imaginary. This brings us to define the critical density until which light can propagate inside the plasma at a given wavelength:

$$n_c = \frac{\epsilon_0 m_e \omega^2}{e^2} \tag{2.39}$$

A wave would reflect at an interface surpassing this critical density and this limit separates what we call an underdense from an overdense plasma. For our laser with a central wavelength of around 800 nm the critical density is at $n_c = 1.7 \cdot 10^{21}\ \mathrm{cm}^{-3}$. A solid material like fused silica has around 400 times this density, making our experiments overdense laser-plasma interactions.

The ions move on the other hand on much slower time-scales, which gives the electrons enough time to follow. The ion acoustic waves oscillate at:

$$\omega_i = \pm k v_s \tag{2.40}$$

with v_s being the ion-sound velocity. In a thermalized state the velocity is:

$$\sqrt{\frac{Z k_B T_e}{m_i}} \tag{2.41}$$

with m_i the ion mass. This will become of interest when we treat the plasma expansion after an initial ionization.

Lastly I would like to define what it means when we talk about relativistic laser intensities. In the non-relativistic case, free electrons quiver inside the electric field oscillations with a certain velocity:

$$v_q = \frac{e E_0}{m_e \omega} \tag{2.42}$$

and we define the normalized laser amplitude as the ratio of this velocity to the speed of light:

$$a_0 = \frac{eE_0}{m_e \omega c} \tag{2.43}$$

Once the speed reaches c, the normalized amplitude reaches unity. We therefore speak about the non-relativistic regime for $a_0 \ll 1$ and the relativistic regime for $a_0 \gtrsim 1$. In terms of laser intensity the normalized amplitude reads:

$$a_0 = \sqrt{\frac{I\lambda^2}{I_0}} \text{ with } I_0 = 1.37 \cdot 10^{18} \, \frac{\mathrm{W}\,\mu\mathrm{m}^2}{\mathrm{cm}^2} \tag{2.44}$$

Part I.

Few-Cycle Femtosecond Beamline for Solid Target Experiments

3. Laser Development Challenges for Solid-Target Laser-Plasma Experiments

As set in the general introduction, the goal of this laser chain is defined by reaching a regime on solid targets, where relativistic harmonic generation and electron acceleration becomes possible. The quiver motion of electrons inside the laser electric field becomes relativistic with a field intensity in excess of $I_{rel} \cdot \lambda^2 \gtrsim 10^{18}\,\mathrm{W} \cdot \mu\mathrm{m}^2/\mathrm{cm}^2$ [9].

Intensity The first type of relativistic laser plasma experiments have been carried out on large and expensive laser facilities using picosecond pulses with multi Joule level energies [10]. Later femtosecond systems with pulse duration less than 100 fs were employed [11]. This trend in increasing the pulse energy has continued and we see now lasers operating with PW peak power in extremely large facilities [12, 13, 14]. It is these installations that also have the highest intensities, but in a somewhat brute force way. They often operate only in single-shot mode or at very low repetition rates making reliable experimental data acquisition difficult. Thermal effects lead to a degradation in beam quality making proper tight focusing troublesome.

While the intensity is proportional to the pulse energy, it is also inversely proportional to the duration and focal area:

$$I \propto \frac{E}{\tau \cdot A} \tag{3.1}$$

And so a distributed effort consisted of using a table-top, high spatial-quality, kilohertz laser in combination with adaptive optics to correct for residual wavefront aberrations. The high quality pulse can then be focused by a low F# parabola down to wavelength spot sizes [15]. With only a 0.7 mJ laser, Albert *et al.* were able to reach the edge of relativistic intensities with $1.5 \cdot 10^{18}\,\mathrm{W/cm^2}$.

Duration and Waveform Control Decreasing the pulse duration is the second method to compress the same energy into higher intensity pulses.

In an atomic, gaseous medium, lasing occurs through stimulated emission from electron transition between two discrete energy levels leading to a well-defined energy difference and thus photon energy. Here the emission line is only broadened by the lifetime, collisions and the Doppler effect. Most media have much larger bandwidth, but nonetheless a wavelength dependent gain coefficient $G(\lambda)$ that peaks at a given wavelength and falls off to 0 at either side. If the bandwidth of the gain medium is not considerably larger than the bandwidth of the laser pulse, the spectral wings will exhibit a much lower gain. Then during each amplification pass the spectrum will become more and more narrow by mostly amplifying the centre part $I(\lambda) \cdot G(\lambda)$ (exact only in the small signal gain regime). This is called gain narrowing.

Ti:sapphire has an exceptionally large bandwidth and in fact the largest one of any common lasing media. It stretches from 600 nm to well over 1000 nm as shown in Figure 3.1. The electronic lasing transitions are possible over a large energy band thanks to the vibronic transitions of the Ti^{3+}-ion inside the Al_2O_3 crystalline matrix. We see the electronic energy levels in Figure 3.1a with respect to the displacement of the Ti^{3+}-ion.

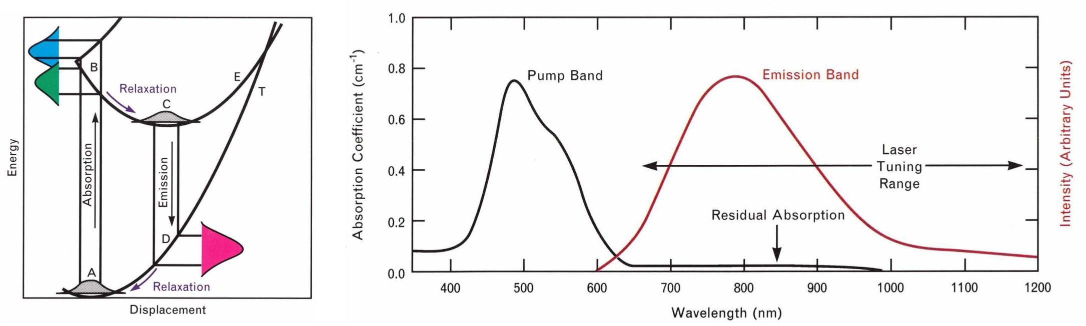

(a) Energy levels and transitions

(b) Absorption and Gain coefficient

Figure 3.1. Lasing properties of a Ti:Sapphire crystal. Reprinted from [16]

This laser medium was therefore the method of choice for a long time to reach fs pulse durations. But ultimately the gain narrowing during amplification limited the pulse duration to no less than around 20 fs at 800 nm. In a spatially dispersed amplifier an impressive duration of only 14.8 fs has been achieved [17], though this is still far from the single cycle regime. With the proposition of a post-compression setup Nisoli *et al.* were able to break this limit by spectrally broadening the pulse through nonlinear propagation inside a noble gas [18]. Chapter 5 deals with this topic of post-compression in detail. All these efforts allowed eventually to get a relativistic laser in a university sized lab.

When reaching this few-cycle regime, accurate control of the actual waveform, in particular the CEP, allows to gate the nonlinear target interaction so it happens only during one cycle. But to keep the CEP under control is a very demanding task. The whole laser chain needs to be very stable and special attention needs to be paid to the stretcher and compressor design of the CPA. We will discuss this issue in more detail in Chapter 4.

Temporal Contrast A major challenge when doing experiments on solid targets becomes what is known as the temporal contrast of the laser pulse. It is defined as the ratio of the peak intensity and the maximum intensity reached until a given time before the main pulse. If this contrast is not high enough, the leading part will provoke a premature target ionization and the main pulse cannot interact any more with a steep and well defined plasma interface.

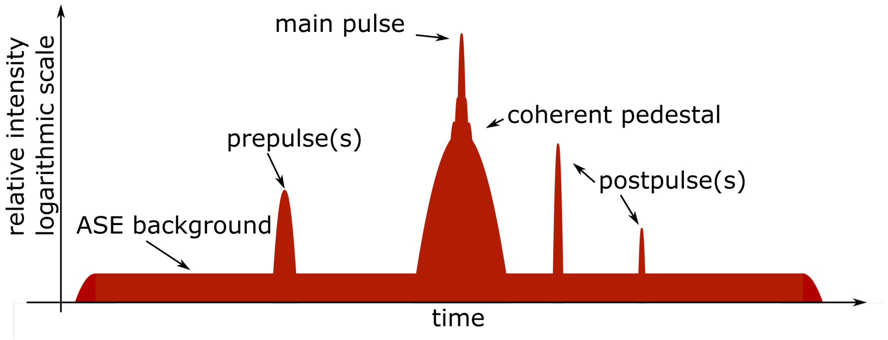

Figure 3.2. Typical temporal intensity profile on a logarithmic scale from a femtosecond laser pulse generated by a traditional CPA architecture.

In Figure 3.2 we see a typical intensity profile of a traditional CPA system. Around the main peak, we first discern a broader shape than a pure Gaussian waveform. This coherent pedestal comes typically from imperfect compression, either from never perfect alignment, or from defects in the optics leading to a residual spectral phase or sharp amplitude variations. Around this we see a number of short but intense pre- or post-pulses as a weak replica of the main pulse. This all sits on a much longer pedestal know as amplified spontaneous emission (ASE), where a spontaneous emission is amplified during the pump duration. This leads to a incoherent background noise on the nanosecond timescale.

The ASE background does not cause direct ionization and damage of the material but is initiated by a slow absorption process on crystal defects, interband transitions and excitations. The damage threshold is governed by a rate equation of electron energy gain and loss, in which electrons scatter off phonons. Once the electron has gained enough energy to surpass the band gap, further impact ionization causes an avalanche breakdown. This happens at intensities as low as $10^9\,\mathrm{W/cm^2}$ [19, 20]. Still a very high intensity in a classical sense, but 10^{10} times less than the targeted peak intensity.

Pre-pulses on the other hand are much shorter, typically even less than 1 ps and therefore ionize the material through their field strength. They lead directly to multi-photon ionization and possible strong collisional avalanche ionization that follows for pulses longer than around 50 fs. For the shortest pre-pulses damage and ionization starts already at intensity levels around $3 \cdot 10^{13}\,\mathrm{W/cm^2}$ and can be an order of magnitude lower for pulses with significant avalanche ionization [20, 21].

Our targeted peak intensity of $10^{19}\,\mathrm{W/cm^2}$ requires an incoherent contrast level of 10^{10} and a coherent contrast, including pre-pulses, around 10^6 up to a few picoseconds before the main peak. Plasma created after this by weak pre-pulses should not expand fast enough to completely destroy the interaction mechanism. We will see in Section 8.4 how the pre-pulse energy affects the plasma expansion velocity.

Stability and Repetition Rate Often laser-plasma experiments are highly non-linear in nature, making a small variation of an input parameter leading to a potentially very different result. Compared to large scale installations operating on a single-shot basis, high-repetition-rate lasers, like kHz systems, are not only intrinsically more stable, but also allow much more data to be acquired and therefore yield statistically more significant results.

4. Chained Amplification with Nonlinear Filter Stage

In a classical Ti:sapphire femtosecond laser system, a Kerr-lens mode-locked oscillator creates a broadband, femtosecond pulse train at a repetition rate typically more than 50 Mhz. The train is filtered by a pulse picker to create a kHz repetition rate. As the individual pulse energy is very low (in our case $\sim 2\,\mathrm{nJ}$), an amplifier needs a very large gain ($\sim 10^6$) to reach mJ pulse energies.

This is also how the system looked like some 5 to 10 years ago, with which our group performed their first solid target laser plasma experiments. A modified commercial Ti:Sapphire oscillator and multi-pass amplifier system (Femtolasers, Rainbow and Femtopower Pro) together with a home-made 3-pass amplifier operating at 1 kHz were able to deliver 3 mJ, 25 fs pulses (description in [22]).

But this creates two major issues for the temporal contrast of the laser pulse. First, the finite extinction of the pulse picker will lead to a forest of pre- and post-pulses around the main pulse for the duration of the amplifier pump (typically $> 100\,\mathrm{ns}$). For us the peak intensity of these pre-pulses would be too high to perform controlled relativistic solid laser-plasma experiments.

Second, the very high gain of the amplifier will lead to what is called ASE. Spontaneous emission of photons and their amplification by the high gain that leads to a certain light noise level. Typically, an ASE contrast of 10^7 to 10^8 can be obtained by a good multi-pass amplifier, like the system previously used by our group. This level would be, however, still too high to perform relativistic experiments on solid targets.

One way to increase the ASE contrast is to insert a nonlinear filter at the end of the laser chain. An established technique is the plasma mirror that exploits the self-induced plasma shuttering effect [23]. The laser is focused onto an anti-reflection coated dielectric interface, so that in normal condition, the laser is fully transmitted. But with the increasing intensity during the rising edge of the pulse, the substrate starts to ionize, and more and more electrons are heated into a plasma. Once this plasma reaches the critical electron density, the remainder of the pulse will be reflected. It is said that the plasma mirror has triggered. This creates very effectively a pulse with a sharp rising edge.

By carefully adjusting the intensity on the plasma mirror with the beam size, the trigger point can be set at a defined point before the main peak. The ASE background and pedestals before the main pulse can therefore be filtered out [24]. The contrast level can be increased by a factor of 10^4 with an energy transmission as high as 50% [25]. Implementing a plasma mirror is rather complex and needs to be done under vacuum. Additionally the destructive nature of the process means the dielectric surface must be refreshed between the shots. Operating a high-repetition-rate beamline requires to do this with high accuracy and at high speed, which further complicates the setup [26]. Additionally, plasma mirrors have been used at the end of the laser chain and therefore reduce the available energy delivered on target.

An alternative solution is to put a nonlinear filter between two complete CPA systems [27]. The pulse energy loss through the nonlinear filter can be recovered in the second CPA and amplified up to the required energy for the experiments. As long as the gain in the second CPA remains low (<1000), no significant ASE will be introduced.

The overall system complexity can be actually lower for a double CPA system than a single CPA with nonlinear filter at the end. This is because the highest average power and the peak intensity determines the required complexity level of the amplifier. Keeping the final energy constant, a nonlinear filter at the end increases the average power inside the last amplifier. Considering a transmission of 50% by the nonlinear filter, this doubles the maximum average power and intensity inside the last amplifier. A far more expensive pump laser is needed for the last amplifier. Also, especially with a kHz system, thermal effects will become much stronger and the amplifier crystal might need to be cryogenically cooled. On the other hand the much smaller absolute energy loss from a nonlinear filter inside a double CPA system is easily recovered and the main added complexity only comes from needing to have two complete stretcher-compressor units.

The conception and implementation of the double CPA system in Salle Noire at the LOA was the main work of Aurelien Ricci's PhD [28]. I participated in the implementation starting with my Diploma Thesis [29]. In this chapter I would like to show again those results together with some new results obtained during my PhD to aid in the understanding of the complete system architecture.

4.1. Double CPA Design

The design of the double CPA chain in Salle Noire was determined by the objective to increase the focused intensity on target ten-fold compared to the first experiments [30]. For this the energy needed to be increased to around 10 mJ while keeping the pulse duration below 30 fs. This could be then efficiently post-compressed to the few-cycle regime. The contrast needed to be increased by 3 orders of magnitude to a level above 10^{10}. All this while keeping a high quality wavefront and full waveform control (CEP). This should allow us to finally reach the relativistic regime for solid target laser plasma interactions. The repetition rate should also stay at 1 kHz.

4.1.1. First CPA

The first CPA is basically the previous laser but without the additional home-made amplifier. A Kerr-lens mode-locked, CEP stabilized oscillator provides broadband ultrashort pulses at a repetition rate of around 80 MHz (Femtolasers, Rainbow). The CEP is stabilized by pump power modulation that is controlled by the deviation of the f-to-2f beat signal to the design frequency. The pulses are then stretched to around ~ 7 ps (over the final amplification bandwidth) by a 20 cm SF57 bulk material stretcher and then amplified by a ten-pass Ti:sapphire amplifier (Femtolasers, customized Femtopower Compact Pro CE Phase) to around 1.9 mJ. Between the fourth and fifth pass, a Pockels cell acts as a pulse picker to provide the final 1 kHz repetition rate. It is placed in the middle of the amplification to provide efficient suppression of ASE outside the cell's opening time. An acousto-optic programmable dispersive filter (AOPDF) (Fastlite, low-jitter Dazzler HR-45-800) is also placed here to provide spectral amplitude and phase correction. At the end, the pulses are recompressed by a transmission-grating compressor (TGC), while the Dazzler takes care of the large TOD mismatch between the bulk material stretcher and the TGC. The CEP drift can be controlled by either a slow feedback on the oscillator locking electronics or a fast feedback to the Dazzler, which directly applies a phase shift on the next acoustic wave at the laser repetition rate.

4.1.2. XPW Nonlinear Filter

The nonlinear filter stage is supposed to increase the contrast by 3 to 4 orders of magnitude to a level better than 10^{10}. For the nonlinear filter process we chose cross-polarized wave (XPW) generation that has been developed as a contrast cleaning method in our institute by Jullien *et al.* [31]. It is a degenerate 4-wave mixing process ($\omega_1^{\perp} = \omega_1^{\parallel} + \omega_1^{\parallel} - \omega_1^{\parallel}$), where a linearly polarized beam is converted into a new orthogonal polarized wave at the same frequency.

An output polarizer then filters out the fundamental beam (Figure 4.1). As it is a purely degenerate process it is automatically phase-matched and achromatic over a very broad bandwidth. Also is keeps the laser wavelength. This is very important if one wants to use the same amplifier architecture for the second CPA.

This process has a cubic intensity dependence ($I_{XPW} \propto I_{fundamental}^3$) and therefore the contrast should be in theory exponentiated by the power of 3. In practice it is limited by the extinction coefficients of the polarizer. This cubic intensity

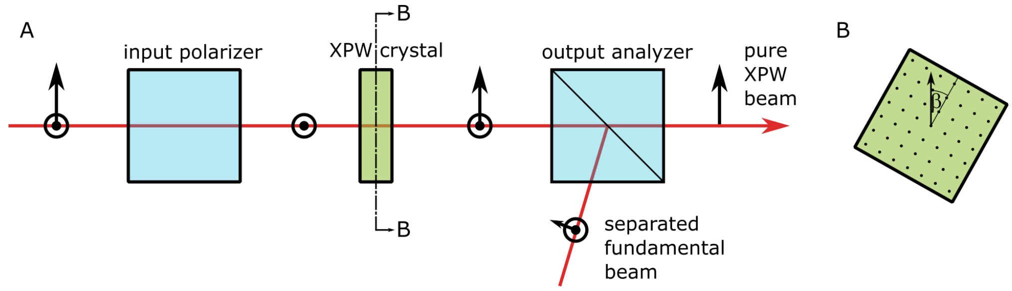

Figure 4.1. A linearly polarized input beam gets converted by an XPW generating crystal (green) to a wave with a orthogonal polarization. This wave is then selected by another polarizer and a pure XPW generated beam leaves the system. Reprinted from [29]

dependence also leads to a temporal shortening in theory by the $\sqrt{3}$. And also, assuming a flat spectral phase, acts as a cleaning device to form a more Gaussian like spectrum. It has also been shown that it preserves the CEP and allows for CEP-stable operation [32].

This technology is now fully developed and has been integrated in many large (>100 TW) laser installations [33, 34]. Our high efficiency implementation is shown in Figure 4.2. The beam is send into a vacuum system where the focused beam is coupled into a 250 μm HCF for spatial filtering [35]. This leads to a diverging beam of high quality, where at just the right distance the intensity is optimal to place a first crystal.

As a crystal material we use barium fluoride (BaF_2). It has a centro-symmetric cubic lattice and so shows no second order nonlinearity. Self-phase modulation (SPM) is proportional to the third-order nonlinear susceptibility $\chi^{(3)}_{xxxx}$, where as XPW generation is proportional to $\chi^{(3)}_{xxxx}$ and the anisotropy σ of $\chi^{(3)}$. BaF_2 has only a moderate value of $\chi^{(3)}_{xxxx} = 1.59 \cdot 10^{-22}\,\mathrm{m^2V^{-2}}$, but a large anisotropy of $\sigma = -1.2$. So one gets high efficient XPW generation without too much SPM [31].

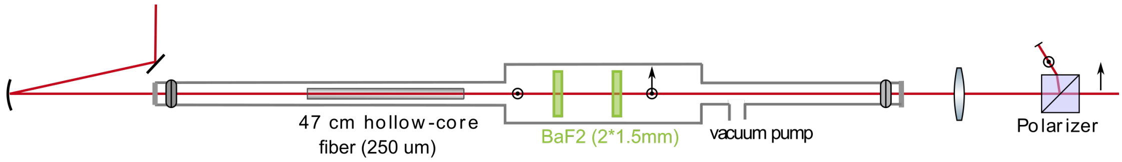

Figure 4.2. Current XPW implementation with a HCF for spatial filtering and two XPW crystals all placed inside a vacuum system. The re-collimated beam is then filtered by a polarizer to obtain a purely XPW generated beam. Based on [36]

This first crystal (1.5 mm thickness) converts around 20% to 25%, which is the limit of the single crystal regime. During propagation the fundamental beam gets depleted in the centre and efficient conversions stops. But after a few centimetres of free space propagation the fundamental beam reshapes. Placing a second crystal there can increase the overall conversion efficiency to around 33% [36].

The beam exits the vacuum system and gets recollimated to a large beam size (25mm clear aperture) to avoid nonlinear effects in the polariser and stretcher that follow. The fundamental beam is rejected by a high extinction ratio, broadband Glan-Laser polarizer (Karl Lambrecht Corp.).

4.1.3. Second CPA

The second CPA is designed to boost the remaining 300 μJ up to the final $\sim$ 10 mJ. In order to maintain good CEP stability, the B-Integral needs to be minimized and consequently, the stretching factor needs to be increased compared to the first CPA. The stretcher and compressor need to remain compact. Environmental fluctuations like air flow or vibrations cause big phase distortion in large open space dispersive systems. Zenghu Chang showed that the reflection gratings inside a compressor or stretcher need to be interferometically stable to prevent random and uncorrectable CEP shifts [37]. This condition can be relaxed inside a prism based compressor, but the large separation between the prism and optics required for high energy pulses make CEP stabilization very demanding.

The ideal solution seems to be the same design as the first CPA (bulk stretcher and TGC) and only up-scale the stretching ratio and beam aperture. The transmission gratings are very close together and allow CEP-stable operation. Unfortunately a TGC has a TOD to GDD ratio of opposite sign than most optical materials. Inside the first CPA the Dazzler could correct this, but ultimately the Dazzler's capacity will limit the maximum possible stretching factor. This would therefore create an unacceptable B-Integral in the amplifier.

This traditional scheme of a CEP-stable, kHz CPA stage (and that of the first CPA) is shown in Figure 4.3a, where we see the complex interplay of the dispersion management. If the TGC could be replaced by a novel device with matching dispersion of bulk material, the stretching would be increased and the B-integral decreases (Figure 4.3b). Therefore we can amplify to tens of mJ without degrading CEP stability or beam quality.

Fastlite developed a new compressor based on the combination of gratings and prisms called GRISM (GRating and prISM) compressor that can perfectly compensate the GDD and TOD of SF57 glass used as the stretcher [38]. The optical design is shown in Figure 4.4. A high index prism pair is enclosed between two transmission gratings. The beam is spatially and temporally dispersed by travelling through all four components. It then needs to pass this configuration a second time to reverse the spatial chirp so that only the temporal dispersion remains. In

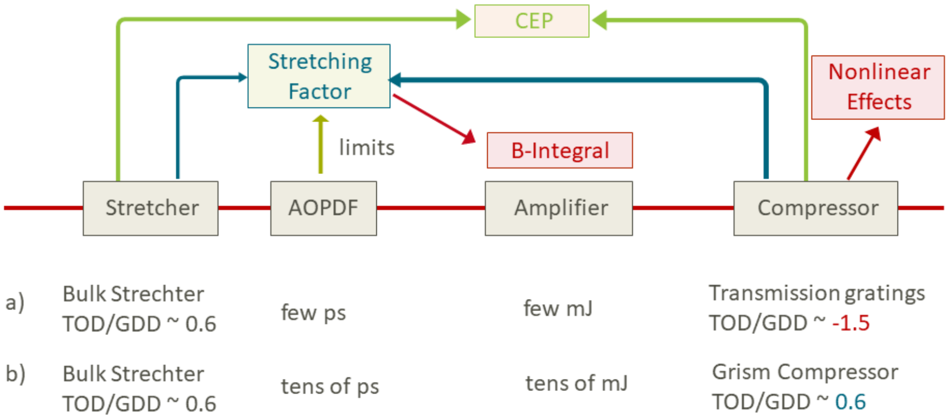

Figure 4.3. Complex interplay between dispersion management and CEP stability as well as beam quality. For CEP stability compact dispersive elements are required. In a) a mismatch in dispersion from a compact stretcher and compressor means the AOPDF limits the maximum stretching factor to a few ps. Due to the B-integral this limits the maximum energy to a few mJ. On the other hand if the stretcher and compressor matches b), the pulse can be stretched to tens of ps and the energy may rise to tens of mJ. The nonlinear effects inside the compressor need to be additionally considered.

fact it is possible to adjust the GDD to TOD ratio to match any material by either translating one of the prisms parallel to the grating or by changing the apex angle of the prisms. The new limiting factor is the fourth-order dispersion (FOD) mismatch between bulk and GRISM.

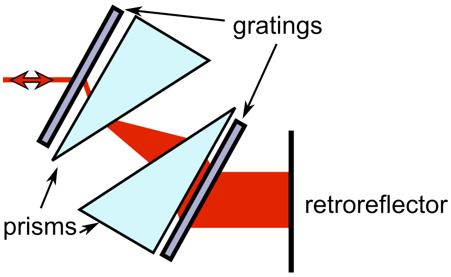

Figure 4.4. GRISM compressor design with two prisms in between two transmission gratings. Reprinted from [29]

Our group went into a collaboration with Fastlite to adapt this novel compressor to a high energy CPA system [39]. The GRISM is particularly suited for this as the air gap between the gratings and prisms insures that the pulse does not travel compressed through the prism material.

The actual implementation for the second CPA is shown in Figure 4.5. We started with 300 μJ pulses from the XPW system. In order to keep the B-integral below π we went for a pulse stretching of 45 ps or 0.75 $\frac{\mathrm{ps}}{\mathrm{nm}}$, which is a factor of 7 higher than the first CPA. This is done by travelling through 75 cm of highly dispersive SF57 glass in a snooker geometry which gets to 30 ps. The Dazzler (double-pass) completed the stretching to 45 ps and compensated the FOD mismatch between the bulk stretcher and the GRISM. Additionally the Dazzler shaped the amplitude to pre-compensate to some extent the gain narrowing in the amplifier.

This only left 30 μJ to be amplified by a 6-pass booster to around 4.2 mJ. And then, separated by a Pockels cell, to 15 mJ by a home-made 2-pass power amplifier with mode adaptation after each pass. Both amplifiers were cooled under vacuum to 180 K. The beam was then extended to around 22 mm (FWe2) and compressed by a GRISM compressor in an unfolded configuration.

The nonlinear effects inside the substrate material of the last grating still made it necessary to finish compression by 8 chirped mirrors (CMs) with a combined dispersion of 2000 fs^2. The compressor had a transmission of around 67%, so we were left with around 10 mJ.

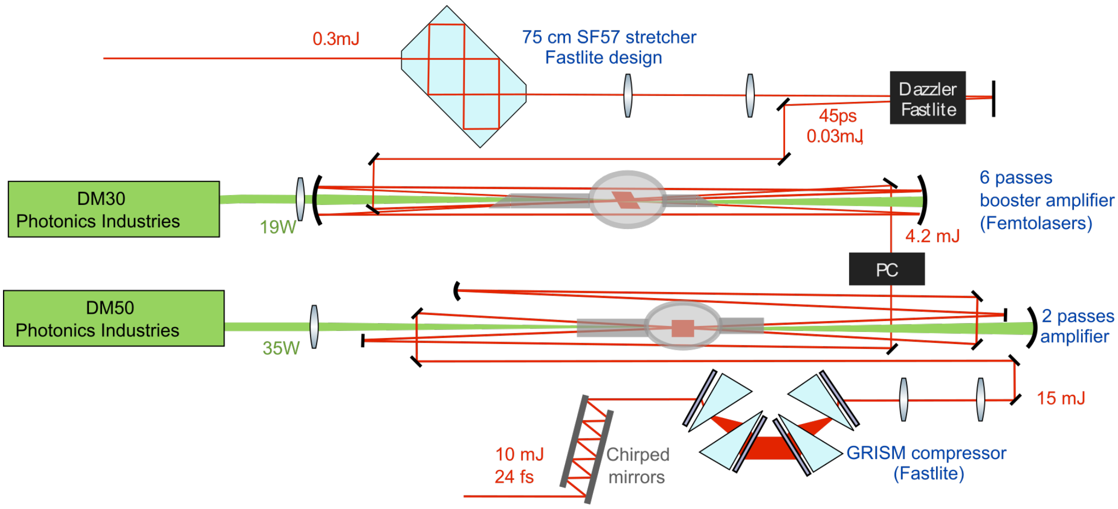

Figure 4.5. Current implementation of the second CPA subsystem. Adopted from [40]

4.2. Results

On a daily basis, we measured 10 mJ after the GRISM compressor and the CMs have a theoretical transmission of around 99%. In principle the CMs can be installed directly after the GRISM compressor, but for the HCF post-compression (Chapter 5) they were installed inside a vacuum chamber. In this configuration the actual compressed energy was slightly lower.

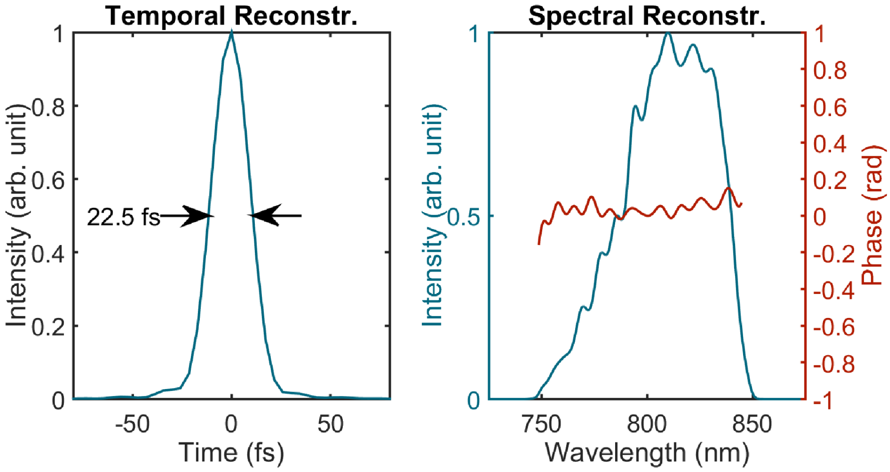

Figure 4.6. Wizzler measurement after GRISM + CM from 07.12.2015.

Thanks to the feedback mechanism of the Wizzler to the Dazzler we obtained a Fourier transform limited (FTL) pulse with a rather flat phase - only some phase oscillations from the CMs remain. We obtained a pulse duration of 22.5 fs (Figure 4.6), but it was depend on alignment and gain narrowing, so in general it will be in the range of 22 to 24 fs. This is significantly shorter than the pulse duration at the output of the first CPA and is thanks to the spectral broadening of the XPW filter.

In Figure 4.7a we can see the output spectrum of the first CPA and of the XPW setup. We can remark a strong spectral broadening with a remarkably resemblance to a Gaussian fit as was predicted from the spectral cleaning effect. The pulse can be compressed by CMs down to a duration of 9.3 fs measured by a Wizzler USP (Figure 4.7b). This corresponds to a temporal shortening factor of around 3, which is higher than the expected $\sqrt{3}$ for a Gaussian pulse with flat phase. It has its origin in significant SPM on the fundamental beam in this high energy XPW setup [36].

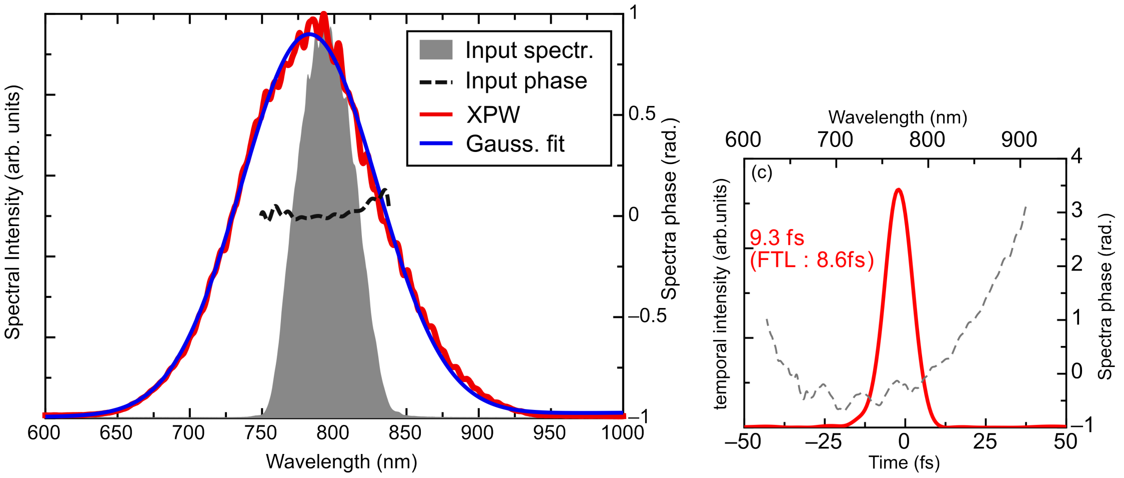

(a) Spectrum before and after XPW filter stage **(b)** Wizzler measurement.

Figure 4.7. Spectro-temporal characteristics of XPW filter stage. Reprinted from [36].

Although the Dazzler would support the full XPW bandwidth, the large amount of FOD that needed to be compensated introduced spectral clipping and we got a transmitted spectrum from around 720 to 890 nm. To precompensate the gain narrowing the amplitude was modulated with a dip in the centre. Most of the gain narrowing happened in the booster amplifier, which has a gain of around 150. The final spectrum after the GRISM is shown in Figure 4.8 together with the spectrum after the Dazzler for comparison.

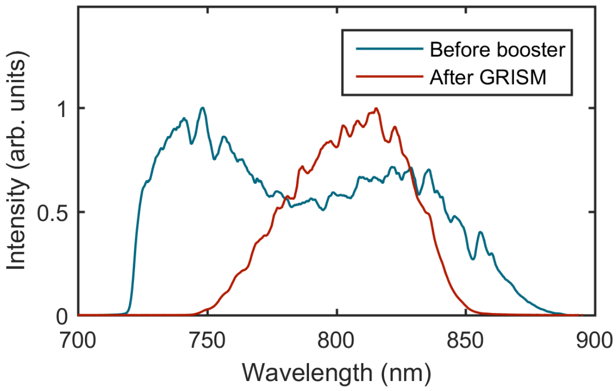

Figure 4.8. Spectrum after Dazzler and after GRISM from 06.11.2013

4.2.1. Spatial Phase

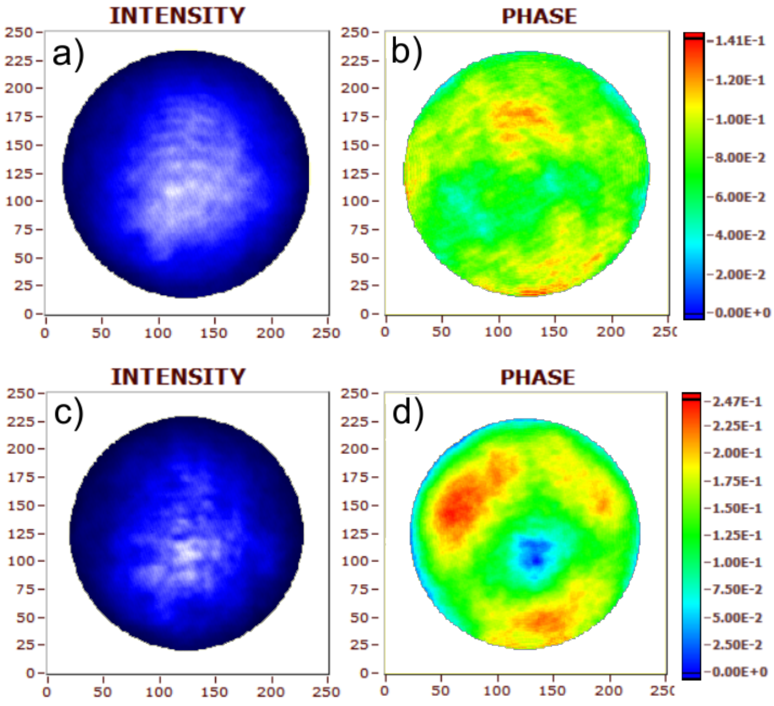

Figure 4.9. Spatial intensity and phase profile of the laser beam retrieved with a wavefront measurement before (a and b) and after (c and d) the GRISM compressor, with subtraction of tilt and spherical phase.

Amplifying a laser beam to a high energy and high average power can introduce strong wavefront aberrations due to thermal or nonlinear effects. Figure 4.9

displays a wavefront measurement before and after the GRISM compressor done with a PHASICS device (Phasics Corp.). For better visualization any spherical and linear phase was subtracted. The beam before the GRISM compressor had a wavefront aberration of 110 nm PtV and 14 nm RMS. This corresponds to a rather good beam quality with an M^2 value of 1.45.

Though after the GRISM compressor significant thermal effects became visible with the spherical aberration Zernike coefficient increased 7 fold. The effect had a long (minutes) reaction time to the input power and it was therefore concluded that it was thermal in nature. The M^2 value after the GRISM compressor was 1.9 with an overall wavefront aberration of 247 nm PtV and 46 nm RMS. This shows that the current GRISM compressor design with a grating size of 30 mm is at its limit regarding average power. In the next chapter we will see that the HCF transmission for this beam quality was only on the order of 70% which can likely be attributed to these wavefront aberrations.

4.2.2. Contrast

To verify the temporal contrast enhancement of the XPW filter stage, we performed high dynamic range 3ω-cross correlator measurements (Sequoia, Amplitude Technologies). The temporal contrast could not be measured after the XPW setup directly as the minimum input energy for the full dynamic range of our cross-correlator is on the order of 1 mJ. So the measurement was done only at the end of the chain. In any case, the ASE level should not have changed in the second CPA as the total gain was below 1000.

In Figure 4.10 we see two contrast measurements showing mainly the coherent properties of the pulse a few tens of ps around the main peak. One measurement was done under the usual condition, the other one with a spectral apodization by the Dazzler to reduce the spectral bandwidth. The final pulse duration was then 30 fs. In fact we found out that some mirrors in the amplifier slightly clipped the spectrum which led to the formation of temporal pedestals by the nature of a Fourier transform. This is clearly visible in the figure.

In the apodized form, the contrast drops sharply to a level around 10^{-6} at 1 ps before the main peak, indication good stretcher-compressor performance. In the condition with full spectral bandwidth we see large pedestals at an intensity around 10^{-4} ± 3 ps around the centre.

Figure 4.11 compares the contrast at the end of the laser chain to a measurement from the first CPA on a long timescale. We can identify a non-coherent ASE background level of less than 10^{-11} until around 20 ps before the main peak. This is an improvement between 10^3 and 10^4 compared to the condition after the first

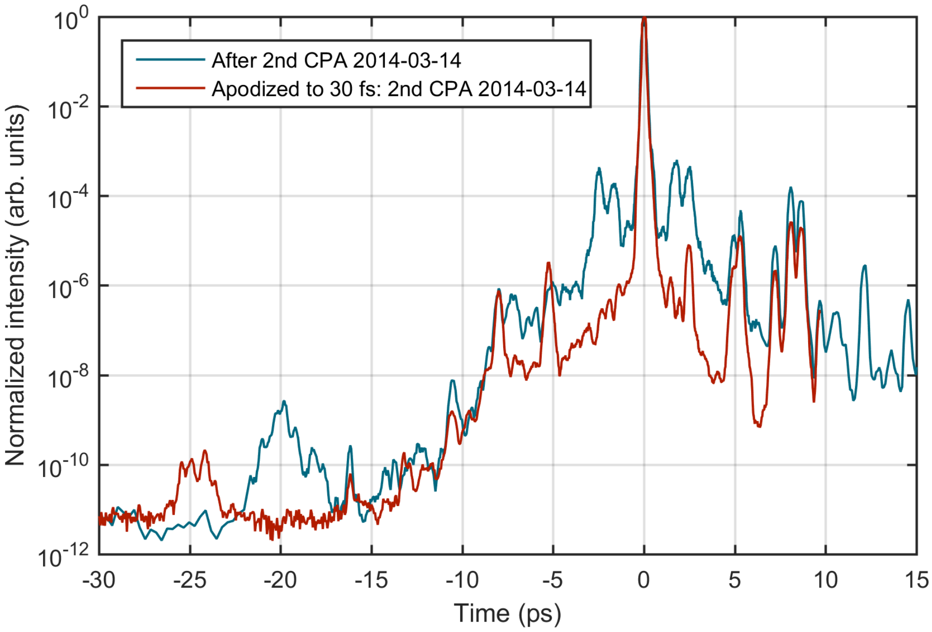

Figure 4.10. Temporal contrast measurement at the end of the laser chain for usual conditions (blue) and with spectral apodization (red).

CPA [1]. This is consistent with the extinction ratio of the fundamental beam in the XPW filter stage. The employed polarizer has an extinction coefficient better than 10^4, but the beam suffers slight depolarization during reflection off mirrors or propagation through optics inside the XPW setup. Therefore the overall extinction ratio is lower.

Nonlinear Post-Pulse Conversion Even in the apodized form, however, the contrast measurement revealed two pre-pulses around 6 and 8 ps before the main pulse. What we found out is that they were caused by a beam-splitter and the XPW vacuum exit window. By removing the beam-splitter and replacing the normal incidence XPW exit window by a Brewster's angled window, the pre-pulses vanished (Figure 4.12).

But the double reflection inside the glass substrate can only introduce a post-pulse. A priori, post-pulses are not an issue for laser plasma experiments as they arrive after the main pulse and cannot alter the experimental conditions any more. But if they are introduced before amplification in a CPA, an unintuitive phenomena can occur that converts post- to pre-pulses. This phenomena has been described

---

[1] Measurements were taken independent from each other, and therefore the actual performance of the filter stage cannot be deduced with absolute certainty from this result.

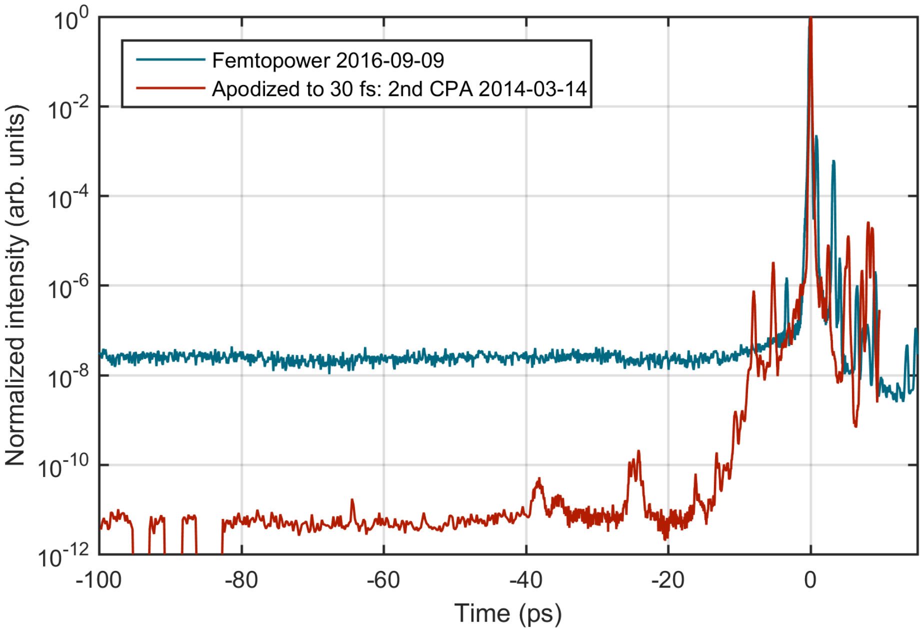

Figure 4.11. Temporal contrast measurement at the end of the chain with spectral apodization (red) compared to a measurement after the first CPA (blue).

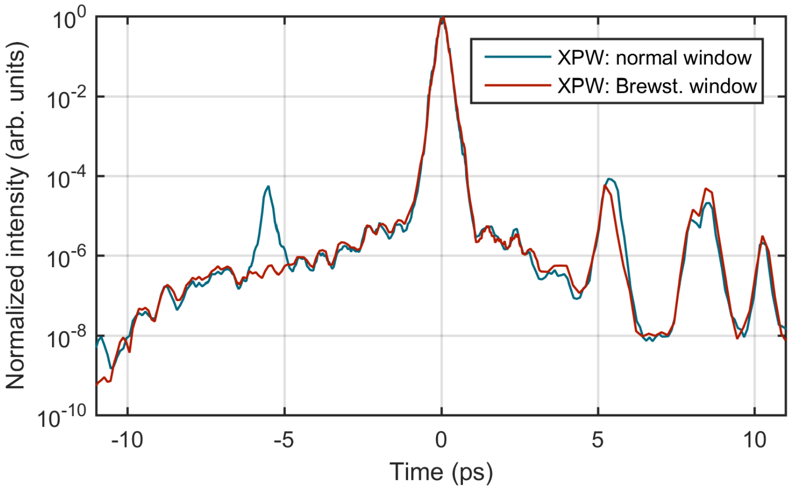

Figure 4.12. Temporal contrast measurement at the end of the laser chain. The normal incidence exit window from the XPW setup introduces a post-pulse 6ps after the main peak (blue). It gets then converted to a pre-pulse during amplification. Replacing the window with a Brewster window solves this problem (red).

both theoretically and experimentally [41, 42].

In a CPA the pulse is temporally dispersed and stretch (in our case to 45 ps). If a post-pulse falls within this window it will overlap with the main-pulse and interfere. As they have different instantaneous frequencies they will form temporal amplitude modulations. During propagation in the amplifier medium a nonlinear response can occur either from saturation effects or from the nonlinear optical Kerr effect. The saturation effects will cause a periodic distortion of the modulated amplitude (and phase). In case the nonlinear effects become significant (in our case the B-integral in the amplifier is around π and can be considered significant), these amplitude modulations cause phase oscillations at the same modulation frequency.

Once the beam gets recompressed, the phase oscillation and amplitude distortion will cause the symmetric emergence of pre- and post-pulses around the main peak. By the nature of the Fourier transform, the delay is related to the modulation frequency, which is just the delay between the main- and initial post-pulse. Therefore post-pulses can get converted into pre-pulses inside a CPA system.

This explains why the beam splitter and XPW exit window were causing the pre-pulses observed in Figure 4.12. This emphasizes once again the care needed when designing a high temporal contrast laser system.

As a side note, the post-pulse that was causing the nonlinear conversion still seemed to be present after replacing the XPW window. It is only slightly lower in intensity. But after amplification, there were still windows present in the beam-pass with the same thickness. The post-pulse from the XPW window were probably just, so to speak, *hiding* under those.

Amplifier Crystal Diffusion Another contrast issue that was causing trouble became visible by a forest of pre-pulses in the auto-correlator measurement after the first CPA stage (shown in Figure 4.13 b). As it turned out, with the limited temporal range, the auto-correlator was not able to measure the real pre-pulse that was revealed by a measurement with a fast photodiode and oscilloscope (Figure 4.13 a). The largest pre-pulse was at 1 ns before the main peak, and the forest of pre-pulses in the auto-correlator trace were likely all post-pulses of this large pre-pulse.

A micro damage on the amplifier crystal, small enough to not cause any drop in output energy, was diffusing a small amount of light. As it is a multi-pass amplifier, any diffusion that happens in focus will be transmitted onto all other passes. As the Pockels cell is installed after the first four passes, the full MHz pulse-train from the oscillator gets amplified. At the fourth pass, the diffusion was re-injecting the amplified MHz train into the first pass. This got then re-amplified by the large gain of 10000 during the first four passes. This pulses have of course a large delay relative to the pulse that diffused. But as it so happened, this delay was just slightly shorter (1 ns) than the period of the oscillator MHz pulse train. Therefore, a re-amplified pulse from the pulse-train was also present before the main pulse, which gets picked by the Pockels cell. This has an opening time of a few ns though, and therefore the parasitic pulse was not blocked and got further amplified in the last six passes.

This explains how a large pre-pulse can be present a nanosecond before the main pulse. And care must be taken to detect any micro damage in the amplifier crystal.

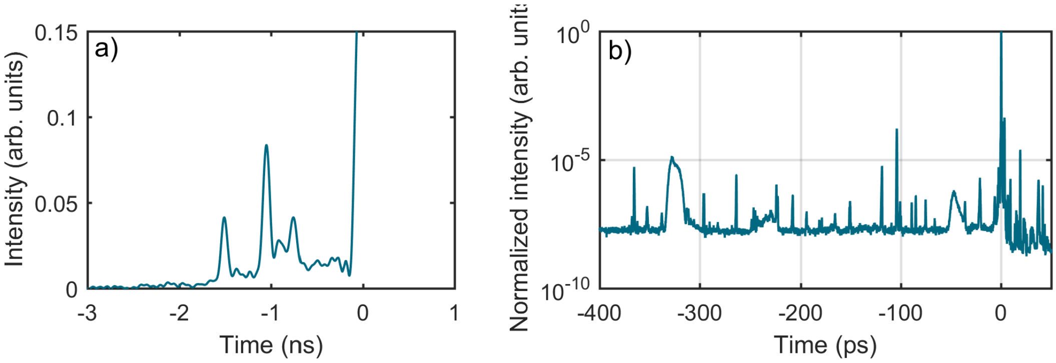

Figure 4.13. Temporal contrast after the first CPA system measured with a fast photodiode (a) on a long temporal range. High-dynamic range measurement with an auto-correlator (b) shows the range closer to the main pulse. The forest of pre-pulses stem all probably from post-pulses of the large pre-pulses seen in figure (a).

4.2.3. CEP

The CEP is measured with a Menlo f-to-2f system (APS 800) and stabilized with a slow feedback on the oscillator locking electronics. At the end of the chain we achieved a RMS phase error of 240 mrad over the course of 45 minutes. The CEP variations are shown in Figure 4.14

Even so, the feedback on the oscillator can destabilize it, particularly when the error signal gets strong. Often the oscillator needed to be relocked after a given amount of time (10 - 60 minutes). In any case, the feedback frequency is also limited to around 10 Hz. To overcome both constraints, we started installing a feedback onto the Dazzler with a kHz CEP measurement with a new device from Fastlite (Fringeezz). The Dazzler updates each acoustic wave to correct for CEP variations. This way the feedback frequency can reach the Nyquist limit and also filter fast CEP instabilities, introduced for example by air fluctuations. Additionally it is completely decoupled from the oscillator, which should give much

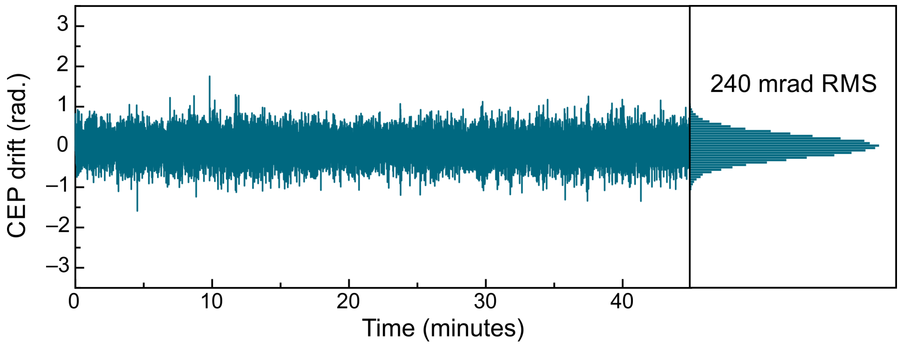

Figure 4.14. CEP drift of the double CPA laser chain at the time when the output energy was 8 mJ and 22 fs.

better long term stability. We did not get to test the full laser chain with the new implementation, but preliminary tests on the Femtopower look promising.

4.3. Conclusion

This section has shown a unique laser chain designed to drive relativistic optics on solid targets at 1 kHz. This is the first double CPA system that can be CEP stabilized thanks to a compact grism-based compressor. The XPW filter improves the temporal contrast by 3-orders of magnitude to the required level of 10^{11}. We published a subset of the results in [40] at the state the chain was in 2014. To fully reach relativistic intensities, the laser can now be post-compressed by the HCF technique, presented in the next chapter.

5. Post-Compression into the Few-Cycle Regime

The gain narrowing limit of Ti:Sapphire amplifiers has restrained the minimal pulse duration that is achievable to around 20 fs in a traditional amplifier. The effect of gain narrowing can be softened by spatially dispersing the seed beam and amplifying different parts of the spectrum independently. The minimal pulse duration achieved with this technique until today is 14.8 fs [17]. Therefore other, radically different ideas need to be considered to reach into the few-cycle regime.

Parametric Amplification One way is to leave the terrain of traditional stimulated emission amplifiers and utilize parametric optical processes. Impressively short pulses down to 4 fs have been amplified by Baltuska *et al.* in 2002 [43]. Recently a high power system with 18 TW peak power and a pulse duration of 4.5 fs was built, where the spectrum is amplified in parts using two different pump colours [44]. Despite the recent advancements in this technology, it is a challenging task and experimental verification of solid laser plasma interaction remains elusive. But certainly this will be achieved in the coming years. Additional it carries along a huge technological change from traditional CPA technology and it would be very expensive to upgrade an already existing CPA based laser chain. Very complex pump lasers are necessary. Besides, the coherent temporal quality is often fairly poor. When doing high-field experiments, this is not of any concern as the processes are highly non-linear. But in the coherent wake emission (CWE) regime on solid target HHG (Chapter 7) this is not the case and a poor temporal quality would prohibit producing clean results.

Spectral Broadening Another way is to spectrally broaden an already amplified signal by some form of nonlinear process that creates spectral components at new wavelengths. Ideally the full energy is only redistributed and not absorbed or lost otherwise. The spectral phase over the full bandwidth must remain defined and smooth, so that is can be flattened through dispersive elements like CM to eventually reach a shorter pulse.

Very early on SPM in single mode fibers has been used to compress pulses. This technique offered excellent propagation and mode quality, but was limited to very low pulse intensities due to material damage [45].

A first attempt on compressing high-power femtosecond pulses was made by Rolland *et al.* in using a bulk material as a medium for SPM [46]. The mode area could be made arbitrarily large and damage to the material was prevented. Self-focusing was overcome by using only a thin slab of material. A four orders of magnitude increase in pulse energy compared to the previously used single mode fibers was achieved. A 92 fs pulse was compressed down to 24 fs and 100 μJ. This technique did not have the advantages of homogeneous propagation. Consequently spatial filters were needed to clean up the profile, which leads to energy loss. They estimated that only 20% efficiency could be achieved. Anyway, for an even higher pulse power, this approached was destined to fail as well due to self-focusing breakup and damage to the material.

Changing the medium to a rare gas with a high ionization threshold can overcome this limit and still gives enough spectral broadening if one assures long propagation distances. For this, the laser is propagated through a gas-filled waveguide in which it then undergoes SPM. This is nowadays a well-established technique developed two decades ago by Nisoli *et al.* [18]. It unites both advantages of excellent mode quality and compatibility with high-power pulses.

More recent, a drastically different approach has been endeavoured by overpassing the ionization barrier in a gas and actually using the plasma formation as means of self-guiding through filamentation [47, 48]. Kerr-lens focusing and plasma defocusing lead to this diffraction-less propagation in filaments and lead to a relative long interaction length. The broadening is then also induced by SPM but with an additional effect coming from the plasma formation that gives rise to a long spectral tail in the blue. The generated pulses are difficult to compress as the spectral phase can depend sensitively on the gas pressure [48]. In particular the leading edge is blueshifted by the sudden increase in the number of free electrons during ionization and the ensuing decrease in refractive index. This, however, leads to a very different phase behaviour to SPM and can therefore not be corrected by usual CMs. This method can provide high transmission in a simple setup, but it also leads to radially inhomogeneous beams, where only the centre contains the shortest pulses. And we also showed that the plasma can lead to spatio-temporal couplings that produce effectively longer pulses in focus [49].

5.1. Spectral Broadening in a Gas-Filled HCF

In Chapter 2 we saw how a four wave mixing process leads to an intensity dependent refractive index $n(t) = n_1 + I(t) \cdot n_2$ that quickly evolves in time with short pulses. This sudden change causes an instantaneous frequency shift. The rising edge will be red-shifted and the falling edge blue-shifted. To ensure a long propagation distance of a tightly collimated beam to generate enough nonlinear phase, the beam is coupled into a gas filled waveguide, typically a hollow-core fiber (HCF).

To get an idea of the spectral broadening, we start by writing the accumulated phase of the laser pulse by integrating along the fiber of length L:

$$\phi(t) = \omega_0 t - \frac{\omega_0}{c} \int_0^L n(t,z)\,\mathrm{d}z \tag{5.1}$$

or we can write it as a nonlinear phase shift with only the nonlinear refractive index, also called the B-Integral:

$$B = \Delta\phi(t) = -\frac{\omega_0}{c} \int_0^L n_2(z) \cdot I(t,z)\,\mathrm{d}z \tag{5.2}$$

The instantaneous frequency is:

$$\omega_{inst} = \frac{\mathrm{d}\phi}{\mathrm{d}t} \tag{5.3}$$

So with the time dependent refractive index we get a frequency shift around the pulse of:

$$\delta\omega(t) = -\frac{\omega_0}{c} \int n_2(z) \cdot \frac{\partial I(t,z)}{\partial t}\,\mathrm{d}z \tag{5.4}$$

The maximal frequency shift is obtained during the steepest slope of the intensity. Figure 5.1 shows this relation.

One can also see, that the frequency shift is linear in the centre of the pulse. But a linear instantaneous frequency dependence is just a second-order phase or also linear chirp, which can be easily compensated by CMs.

It is convenient to derive a simple formula for the broadening factor F for a FTL Gaussian input pulse and neglecting dispersion (only SPM). This will prove helpful in determining the scaling law at high power. As the spectral and temporal width are related by the time bandwidth product $\sigma_\omega \sigma_\tau = 0.5$ (Equation (2.27)), the steepest slope can be derived from the spectral bandwidth σ_ω and this replaces the differentiation in Equation (5.4). Pinault *et al.* [50] showed that the broadening factor becomes simply:

$$F = \frac{\sigma_\omega}{(\sigma_\omega)_0} = \sqrt{1 + \frac{4}{3\sqrt{3}} B^2} \tag{5.5}$$

And we see that for large broadening factors $F \gg 1$, it approaches the B-integral.

For very short and broadband pulses proper treatment of the nonlinear Schrödinger equation (NLSE) leads to a group velocity that is also dependent on the intensity.

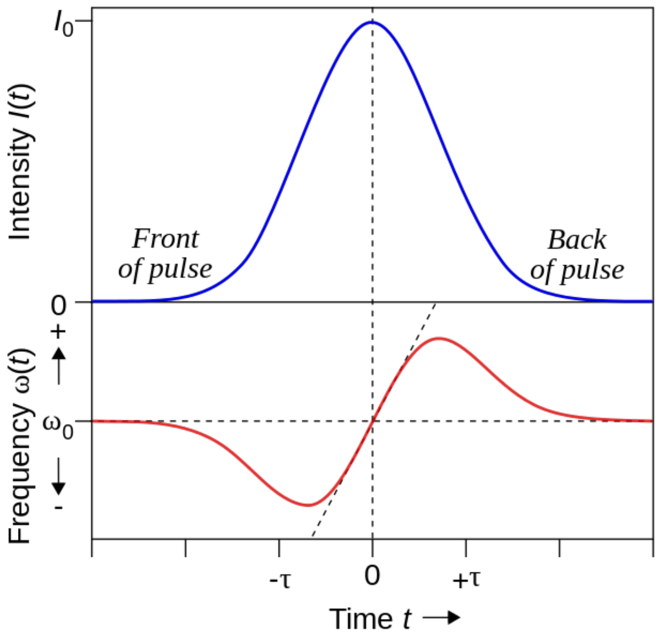

Figure 5.1. Instantaneous frequency shift of an intense laser pulse due to SPM. Licensed under CC-BY-SA-2.5, created by Emmanuel Boutet

Usually this leads to a lower group velocity for the centre of the pulse. This is called self-steepening, where the trailing edge slope increases and the leading slope decreases. This leads to an enhanced frequency shift in the trailing part of the pulse and therefore an overall blueshift of the spectrum [51, 52].

5.1.1. Propagation Modes in a Hollow Waveguide

Unlike optical fibers, that have a cladding of lower refractive index compared to the core, hollow waveguides cannot profit from the total internal reflection. Instead they are rather *low quality* waveguides that in a sense only loosely bind the beam to its core. The guidance properties have been described by Marcatili and Schmeltzer in [53]. The solution to the wave-equation inside a hollow waveguide leads to three types of modes. The transverse electric or TE, transverse magnetic or TM and the hybrid or EH modes. The first two mode types represent a distribution of either pure circular electric or magnetic fields. Only the hybrid modes allow for a quasi-linearly polarized wave. The transverse electric field for EH_{nm} modes can be constructed from Bessel functions:

$$\vec{E}_{nm}(r,\theta) = J_{n-1}(\frac{u_{nm}\cdot r}{a}) \cdot [\cos(m\theta)\cdot \vec{e}_\theta + \sin(m\theta)\cdot \vec{e}_r] \tag{5.6}$$

with a being the inner core radius, J_n the n$^{\text{th}}$ order Bessel function and u_{nm} the m$^{\text{th}}$ zero of the n$^{\text{th}}$ order Bessel function. We see that the intensity profile for a proper mode is always circular symmetric. Only through the interference of different modes can this symmetry be broken.

In any case, during propagation the wave exhibits attenuation from their intrusion into the dielectric cladding. The attenuation constant for the hybrid modes is given by:

$$\alpha_{nm} \propto \left(\frac{u_{nm}}{2\pi}\right)^2 \cdot \frac{\lambda^2}{a^3} \tag{5.7}$$

with the proportionality constant being dependant on the refractive index of the cladding. The transmitted power becomes then:

$$P(L) = P_0 \cdot \exp(-2\alpha L) \tag{5.8}$$

We see that the attenuation is close to quadratic in the mode order n or m, under the very crude assumption that the zeros of the Bessel function are linearly spaced. Therefore, under the right conditions, higher order modes get quickly attenuated in contrast to the fundamental mode. As such, the HCF acts as a spatial mode filter that can be very useful to spatially clean a laser pulse. The lowest order mode very much resembles the Gaussian beam profile. If consequently the laser focus has aberrations from the ideal shape, these are coupled into the higher order modes. The selective attenuation of these higher order modes then leads to a cleaner Gaussian like beam profile after the HCF. This was already used in the XPW temporal cleaning stage described in Chapter 4. In fact we can see the fiber transmission for the linearly polarized modes EH_{1m} in Figure 5.2. The left figure shows the 40 cm long HCF used in the XPW setup, while Figure 5.2b corresponds to the much longer HCF eventually used in the post-compression setup. In both cases we note that the 4th or higher order modes are attenuated to less than 40% initial power.

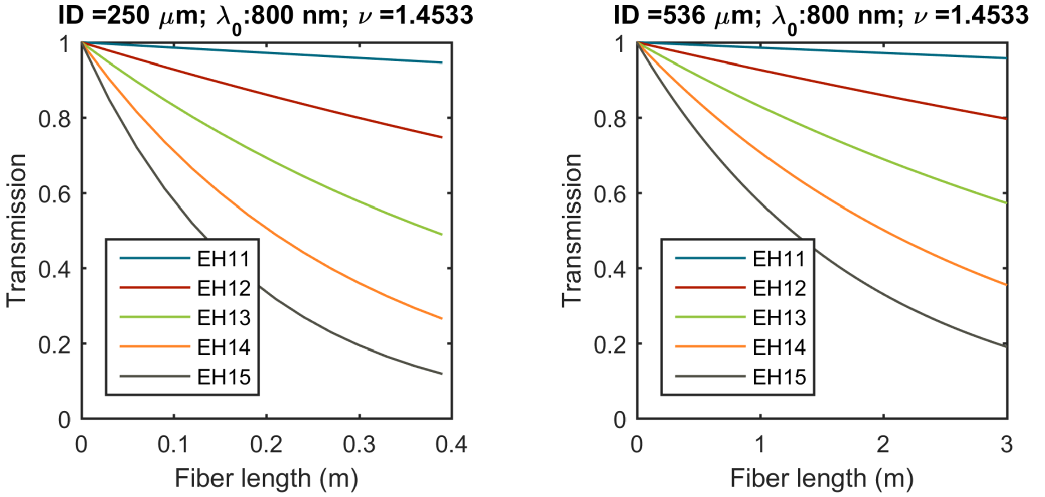

(a) HCF used for the XPW filter

(b) HCF used for the post-compression setup

Figure 5.2. HCF tranmission of the lower order hybrid modes.

Coupling into a HCF

For optimal operation, it is important to couple most of the laser beam into the fundamental mode of the fiber. For this the beam needs to be focused onto the fiber entrance and match as best possible the fundamental mode. Fortunately, the Gaussian beam, as the eigensolution to the paraxial Helmholtz equation, can be adjusted in size to form a close match. In any case, the Gaussian beam is the mode out of most lasers.

To calculate the incoupling efficiency, we project the input profile onto the different modes [54]. We consider a Gaussian beam with linear polarization that is centrally focused onto the HCF with the following profile:

$$E(r, w_0) = \sqrt{\frac{2}{\pi}} \cdot \frac{1}{w_0} \cdot \exp\left(-\frac{r^2}{w_0^2}\right) \tag{5.9}$$

Being linearly polarized, this beam couples into the hybrid modes with EH_{1m}. The absolute field amplitude of those modes is given from Equation (5.6)

$$E_{1m} = \frac{1}{\sqrt{Q_m}} \cdot J_0\left(\frac{u_{1m} \cdot r}{a}\right) \tag{5.10}$$

with the energy normalization of $Q_m = \int J_0^2\left(\frac{u_{1m} \cdot r}{a}\right) 2\pi r \, \mathrm{d}r$.

The inner product of two wave functions is defined as: $(\varphi, \psi) = \int \varphi^* \psi \, \mathrm{d}^3 x$. To develop the Gaussian input beam onto the eigensolution we therefore calculate the inner product for all combinations:

$$c_m(w_0) = \int E(r, w_0) E_{1m} \cdot 2\pi r \, \mathrm{d}r \tag{5.11}$$

The relative optical power inside a given mode is then $P_m(w_0) = [c_m(w_0)]^2$. The burning question is what beam size w_0 optimizes the coupling into the fundamental mode. We see in Figure 5.3 the relative energy in the different modes depending on the Gaussian beam size. We note for an optimal beam size of $2w_0 = 0.64 \cdot \mathrm{ID}$ (ID: inner core diameter) the coupling is optimized at 98% into the lowest order mode. The coupling into the fundamental mode is, however, asymmetric over the beam size and falls steeply towards smaller input beams. As such, if the experimental condition do not allow a perfect match, a slightly larger beam is better than a smaller one. This also avoids exciting the second mode too strongly.

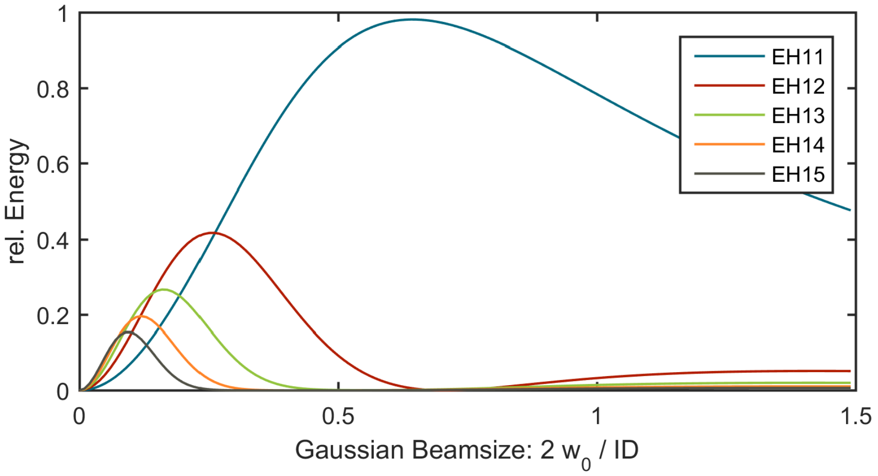

Figure 5.3. Coupling coefficients between the hybrid modes E_{1m} for a HCF and a Gaussian beam with the mode size of w_0

Curvature of the Fiber Axis

Another crucial aspect for the losses during linear fiber propagation, is the longitudinal curvature of the waveguide. Due to the weak guiding already a rather weak bending leads to significant losses. An additional term can be derived for the attenuation constant (Equation (5.7)) that takes the radius of curvature R into account. Taking the curvature orthogonal to the plane of polarization, this leads to [53]:

$$\alpha_{nm}(R,\theta=90)\propto\left(\frac{u_{nm}}{2\pi}\right)^2\cdot\frac{\lambda^2}{a^3}+\frac{4}{3}\left(\frac{2\pi}{u_{nm}}\right)^2\left(1-\frac{n(n-2)}{u_{nm}^2}\right)\cdot\frac{a^3}{\lambda^2R^2} \tag{5.12}$$

Then we can derive a radius of curvature R_0 that doubles the losses for the fundamental EH11 mode as:

$$R_0\approx 9.2\cdot\frac{a^3}{\lambda^2} \tag{5.13}$$

This scales to the third power in core radius and therefore rises very quickly for large inner-core diameter (ID) fibers. It becomes an experimental challenge to implement a fiber support that keeps the fiber straight over the full length. Typically a 250 μm ID HCF ($a = 125\,\mu$m) has been used to broaden mJ level pulses. This gives a characteristic radius of curvature of $R_0 \approx 224$ m at 800 nm, which is a reasonable value that is achievable for fiber lengths around 1 m. But increasing the core diameter, which becomes necessary for higher pulse energies, to for example 536 μm leads to an order of magnitude increase to $R_0 \approx 300$ m. Considering that also longer fibers are needed this becomes very challenging. This radius of curvature corresponds to a deviation at the end of a 1 m long fiber of only 1.8mm from a straight line.

5.1.2. Scaling Law of a Hollow-Core Fiber Compressor

The HCF compressor is a well-established technique developed some 20 ago, but so far it has still remained challenging at multi-mJ pulse energies. These high energy pulses might damage the fiber entrance quickly by a degraded beam profile coming either from the laser itself or by being introduced directly from the HCF input optics. This can be, for example, nonlinear effects in the input window or also the gas. Resulting in either a slow ablation of the fiber material or directly to a catastrophic failure through melting. Additionally the beam might self-focus inside the gas and/or ionize it, leading to a high loss in transmission and a very unstable broadening.

In order to achieve controlled spectral broadening with minimal losses, it has been shown that one needs to fulfil two limiting criteria [55]. First the peak power of the pulse needs to stay below the critical power for self-focusing:

$$\nu P\leq P_{cr}=\frac{\lambda^2}{2\pi n_2} \tag{5.14}$$

Actually already below the threshold the mode size in the HCF decreases with increasing power until it finally collapses at the critical power. Therefore a certain safety margin is ensured by the factor ν with should be on the order of 2 to 4.

Secondly the peak intensity needs to stay below the threshold for photo-ionization:

$$I \leq I_{th} \tag{5.15}$$

On the other hand the spectral broadening is proportional to the B-Integral as we have seen in Equation (5.2). The integral can be replaced by introducing an effective length, which consumes a varying gas pressure and an attenuation along propagation:

$$B = \frac{2\pi}{\lambda} n_2 I L_{eff} \tag{5.16}$$

Together with the first limiting criteria we get an upper limit for the broadening that is actually only dependent on the wave guide geometry. In particular it is not dependent on the nonlinear refractive index n_2:

$$B \leq \lambda \frac{L_{eff}}{A_{eff}} \tag{5.17}$$

and we absorbed again the particular spatial mode profile into an effective mode area $A_{eff} \propto ID^2$. Practically this means one has to tune the n_2 value by adjusting the gas pressure ($n_2 = \kappa p$, p: pressure) to a value just below violating the self-focusing criteria. The spectral broadening is then purely determined by the waveguide geometry.

From the second criteria we get a lower limit for the core area of the fiber by:

$$A_{eff} \geq \frac{P}{I_{th}} \tag{5.18}$$

Of course ionization is a process that gradually increases with laser intensity and given as an ionization rate. To more properly define a threshold, Vozzi *et al.* proposed that the phase shift due to ionization should stay three orders of magnitude below the phase shift from SPM. By taking into account the free electron density properly calculated with the Ammosov–Delone–Krainov (ADK) theory, they concluded with a simple fit for the minimal core radius of:

$$a \geq A \frac{E^{0.51}}{\tau^{0.45}} \tag{5.19}$$

with A a constant factor depending on the gas. This can be minimized by using a gas with a high ionization threshold. The gas with the highest threshold is Helium. It seems only justified to use another type of gas when the pressure required to achieve a certain n_2 value would be too high to be mechanically practical.

These two limiting relations give the scaling law of a HCF compressor, that with increasing the pulse power and keeping the spectral broadening constant, the length of the fiber and the core area need to be increased proportionally:

$$P \propto A_{eff} \propto ID^2 \propto L_{eff} \tag{5.20}$$

To reduce the required fiber dimensions two additional methods can be used. By going from linear to circular polarization the effective ionization threshold is increased by a factor of 1.5 by the reduction of the electric field strength. Additionally it has been shown that circular polarization leads to a more defined mode beating during propagation and therefore more stable spectral broadening [56].

However, also limited by available lab space, this might not be enough to fulfil the conservative scaling law. A second method was tested in 2005 by Suda *et al.* using a pressure gradient in the fiber with vacuum in the front and nominal exit, efficient incoupling can be maintained without distortion from ionization or self-focusing [57]. The downside is that the effective interaction length gets reduced by 33%, but nonetheless with a given space available, this technique allows an upscaling of energy while maintaining similar controlled broadening with increased pressure at the output.

Some groups have tried using chirped input pulses in order to fulfil the limiting criteria [58]. It is not evident from theory though, why this should have a positive effect. The spectral broadening factor (Equation (5.5)) was calculated assuming a FTL Gaussian pulse. The actual frequency shift (Equation (5.4)) is proportional to the slope of the intensity profile though. This means by chirping the input pulse, the spectral broadening gets reduced quadratically in the stretching ratio, while the peak power and the peak intensity are only reduced linearly. To compensate the loss in broadening, the gas pressure needs to be increased also quadratically. This is not possible, if one was already at the limit of self-focusing. And while staying just at the critical power for self-focusing, the effective broadening factor gets reduced exactly by the input pulse stretching ratio.

On the other hand, if ionization is a problem, stretching the pulse lowers the intensity only linearly while lowering the broadening quadratically. A much better approach would be to increase the mode area of the HCF, with which both the intensity and the spectral broadening vary linearly.

Stretched Flexible Fiber

At multi mJ pulse energies with the goal of reaching few-cycle TW class output pulses, the scaling law unavoidably calls for very large and long fibers. On the other hand, we have seen in Section 5.1.1 that for large fibers already a relatively small curvature of the propagation axis leads to considerable losses and excitation of higher order modes. It becomes practically impossible to ensure the required straightness for a few meter long fiber with the traditionally used metallic V-groove support.

For our implementation we went into a collaboration with Tamas Nagy and Peter Simon from the Laser-Laboratorium Göttingen e. V. They developed the so called stretched flexible fiber technique, where a very thin walled and flexible capillary get stretch to a high tensions between two supporting ends [59, 60]. Being very light due to the thin cladding only moderate stretching forces around 10 N are required so suppress gravitational bending. The resulting radius of curvature is on the order of $\sim 10\,\mathrm{km}$, becoming totally negligible for our application. The transmission approaches the theoretical value only due to mode attenuation and a quasi-diffraction limited beam profile emerges out of the fiber.

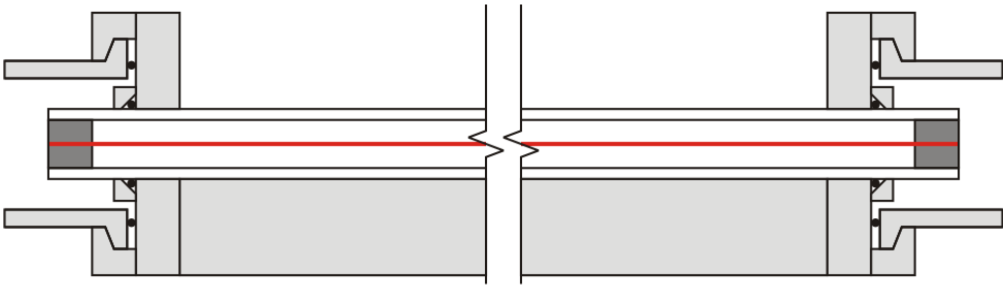

Figure 5.4. Stretched flexible fiber assembly. HCF, shown in red, is permanently glued at the ends in a stretched state to a metallic vacuum enabled support. Reprinted from [60]

Figure 5.4 shows the assembly. During manufacturing a metallic support is put around the stretch capillary. At two endpoints epoxy glue permanently ensures the stretching force provided by the metallic support. A diamond tools then cuts the rest of the capillary close to the glue points. With proper sealing to a vacuum support, this assembly allows for the pressure gradient mode.

These thin walled flexible capillaries are very sensitive to damage though. Especially at the entrance, pedestals in the spatial beam profile might either lead to direct ablation, or to a catastrophic melting. To prevent this a conical glass taper is installed coaxially in front of the input. This eventually unites both advantages of a standard rigid fiber and its resistance against light, and having an ideal scalable waveguide by the stretched flexible fiber technique.

5.2. 1st Implementation

In this section we will discuss the first implementation of a large and long HCF in the upgraded Salle Noire laser facility described in Chapter 4. It was supposed to replace the previous rigid, 1m long HCF installed on a V-Groove, working at less than half the energy. Back then in 2011, 1.6 mJ, 4.8 fs CEP-stable pulses were generated [61]. We plan to triple the peak power of the pulses with this new implementation.

5.2.1. Experimental Setup

At this time of the laser chain development, between 7 and 8 mJ, ~ 24 fs pulses were available for post compression, depending on daily alignment performance. It is possible to continuously tune the spectral phase with the Dazzler in the 2nd CPA. The spatial phase is affected by thermal and nonlinear effects inside the GRISM and amplifier crystals, but the beam profile in focus remains very Gaussian like with a 88 % theoretical incoupling efficiency, calculated by projection onto the fundamental fiber mode (Figure 5.5). Of course this calculation does not take into account the spatial phase of the pulse and is therefore rather an upper limit.

Gas	$\mathrm{n_2}$ $(\frac{\mathrm{cm}^2}{\mathrm{W}})$	$\mathrm{I_p}$	Polarization	$\mathrm{ID_{min}}$	p_{crit}
Neon	$\sim 7.5 \cdot 10^{-21}$ [62]	21.56 eV	linear	862 μm	0.41 bar
Neon	$\sim 7.5 \cdot 10^{-21}$ [62]	21.56 eV	circular	722 μm	0.57 bar
Helium	$\sim 3.5 \cdot 10^{-21}$ [63]	24.59 eV	linear	756 μm	0.87 bar
Helium	$\sim 3.5 \cdot 10^{-21}$ [63]	24.59 eV	circular	633 μm	1.23 bar

Table 5.1. Minimal ID for different gases and laser polarization for a input pulse of 8 mJ and 24 fs, calculated using Equation (5.19) and a value of A for Helium of $A_{He} = 2.62 \cdot 10^{-9}\,\mathrm{ms}^{0.45}\mathrm{J}^{-0.51}$ and for Neon $A_{Ne} = 2.99 \cdot 10^{-9}\,\mathrm{ms}^{0.45}\mathrm{J}^{-0.51}$ [55]. Additionally, the critical pressure is shown, defined as the pressure when self-focusing occurs, i.e. without the safety margin ν from Equation (5.14).

Taking 8 mJ, 24 fs pulses as the reference, we can use the scaling law from Section 5.1.2 to get an idea for the minimal fiber diameter and the maximal gas pressure. This is shown for Helium and Neon in linear and circular polarization in Table 5.1. We quickly realize that our laser power requires unprecedented large dimension and only Helium and circular polarization seems to be a viable option.

As we have seen in the previous section, the spectral broadening scales proportional to $\frac{\lambda L}{A}$, when staying at the critical power for self-focusing. The large minimal ID values from Table 5.1 will require very long fibers. We cannot, however, scale the length indefinitely as we are limited by available space on the optical table (total length 5.5 m). This means that we have to accept a certain ionization in order to get enough spectral broadening to reach the sub-2-cycle regime. In particular the minimal ID was calculated using a conservative approach. So we estimate that

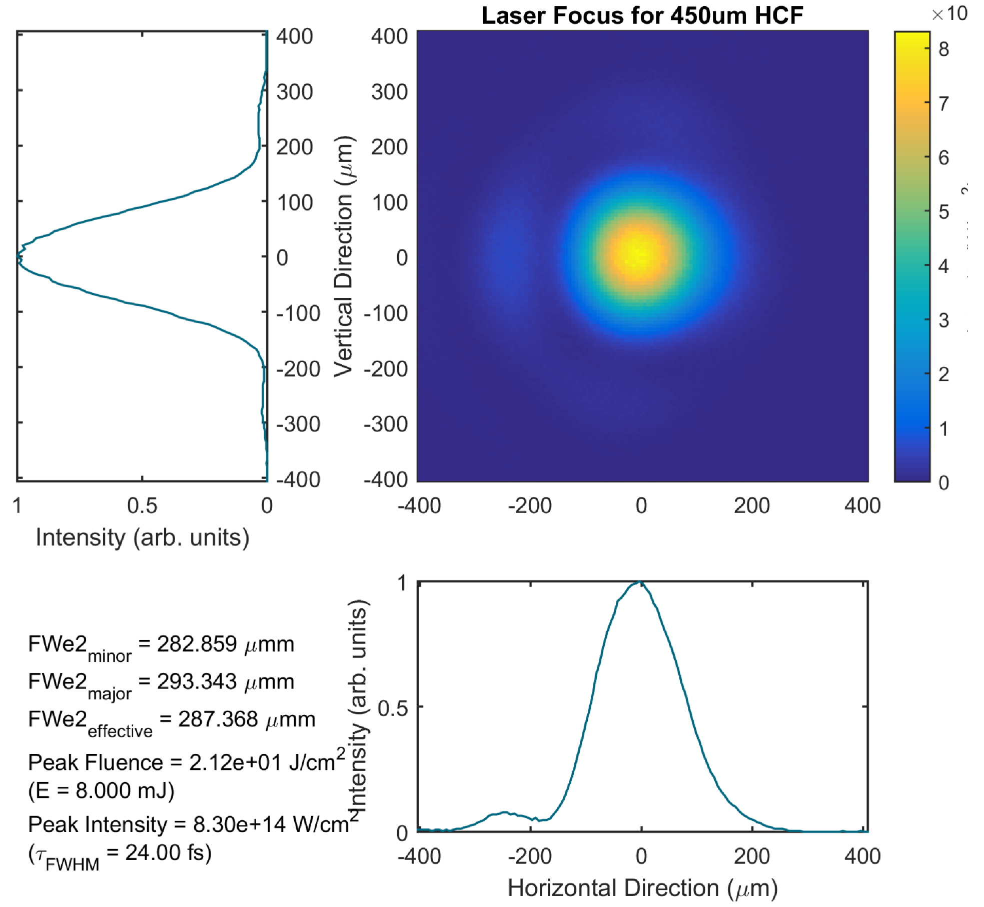

Figure 5.5. Spatial beam profile in focus in front of the HCF. Beam size optimized for a fiber ID of 450 μm

it should be ok using a smaller core, even more so if we use the pressure gradient technique.

As a side note, it has been very hard to determine the nonlinear refractive index for light noble gases accurately. Therefore the maximum gas pressure, or in other words the minimal fiber length for sufficient spectral broadening cannot be determined beforehand accurately.

Therefore 3 HCFs had been chosen for testing to determine the optimal size suited for our laboratory conditions. Table 5.2 shows them together with their upper limit for the B-integral $\frac{\lambda L}{A}$. Fiber #48 could not be used due to extremely poor performance, possibly from a mechanical defect. The ideal fiber with an ID of 633 μm would need to be 4 m long to get at least the same broadening as the 3 m, 536 μm fiber. Unfortunately this would not fit on the optical table.

Serial Number	ID (μm)	length (m)	$\lambda L/A$
#43	450	2	~ 10
#48 (defective)	450	3	~ 15
#36	536	3	~ 10

Table 5.2. HCFs for first implementation phase.

Optical Layout We can see the optical layout in Figure 5.6. First the compressed pulse went through a quarter-wave plate (QWP) to turn the polarization circular. Then a telescopic focusing system, consisting of one concave (f_{cc}) and one convex (f_{cx}) mirror, separated by the distance d, allowed for proper adjustment of the final beam size in focus:

$$w_0 = \mathrm{M}^2 \frac{\lambda f_{eff}}{\pi w} \;;\; \text{with } f_{eff} = \frac{f_{cc} f_{cx}}{f_{cc} + f_{cx} - d} \tag{5.21}$$

with M^2 being a measure for the beam quality. A two mirror focus system has the additional advantage to allow for astigmatism correction by solving the equation $f_{eff,sag} \overset{!}{=} f_{eff,tan}$ of the effective focal length, with each mirror's individual focal length depending on the incidence angle θ: $f_{tan} = f \cos(\theta)$ and $f_{sag} = f \cdot \cos^{-1}(\theta)$.

The stretched flexible fiber assembly itself was connected at the front to a tube with a vacuum system, where the beam enters through a thin, AR-coated window. At the output there was a symmetric arrangement, just instead of a vacuum pump there was a pressure controlled gas inlet.

To properly couple in the fundamental mode the beam needs to be aligned precisely coaxial to the HCF. But thermal and nonlinear effects led to a slow and

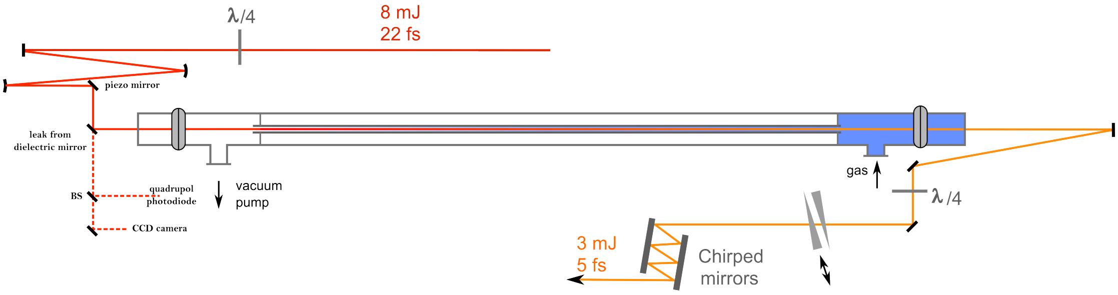

Figure 5.6. Layout of the optical setup around the HCF post-compression for the first implementation.

fast beam pointing derivation and fluctuation respectively. To counteract this two additional mirrors were installed after the focus system to allow for a small leak being used as a reference. A quadrant photodiode detected any pointing fluctuations and gave feedback to an active piezo mirror. Additionally, by installing a camera simultaneously with a beam-splitter, this allowed monitoring the beam profile and beam pointing as it was in focus at the entrance to the HCF. With the stabilization feedback on, we achieved a reduction in pointing fluctuation on the order of 40% (Figure 5.7).

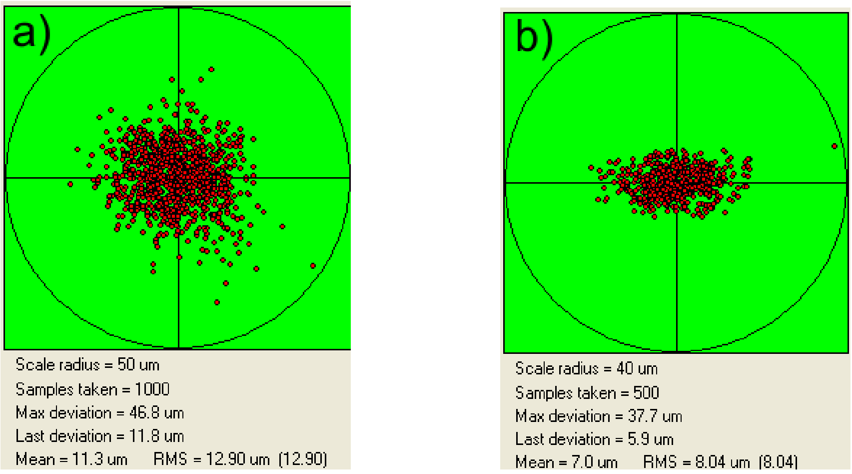

```
Scale radius = 50 um
Samples taken = 1000
Max deviation = 46.8 um
Last deviation = 11.8 um
Mean = 11.3 um     RMS = 12.90 um  (12.90)
```

```
Scale radius = 40 um
Samples taken = 500
Max deviation = 37.7 um
Last deviation = 5.9 um
Mean = 7.0 um     RMS = 8.04 um  (8.04)
```

Figure 5.7. Beam pointing fluctuations without (a) and with (b) far-field stabilization enabled, measured at focus with a CCD camera for a beam profile optimized for a 450 μm ID fiber.

Ideally the circular polarized beam should not be reflected off any surfaces at non zero incidence angle, as this leads to a differential phase shift and elliptical polarization. During spectral broadening this ellipsoid will be rotated and a significant energy will be eventually lost to the wrong linear polarization. Unfortunately, the limited space around the vacuum tube and the entrance window did not allow for a beam sampling in final focal conditions without inserting two mirrors at 90°.

Subsequently a concave mirror collimated the beam and a broadband QWP reversed the polarization state to linear p-polarization. Thin wedges at Brewster's angle installed on a translation stage allow for an adjustable glass insertion and therefore a fine tuning of the dispersion. Finally ultra-broadband CMs in the double angle technique configuration [64] compensate the spectral phase and compress the pulse.

5.2.2. Results

Nonlinear Transmission Effects Unfortunately, directly at the beginning, several problems attracted our attention which commonly arise when operating a high intensity and high average power laser chain. First, the GRISM compressor showed strong thermal effects that led to a shift in focus of several centimetres during the first 30 minutes of operation. As the HCF itself is fixed, this means that the focus position for optimal fiber incoupling needed to be adjusted after GRISM warm-up.

The bigger problem was nonlinear effects in the entrance window to the HCF. Using large core fibers implies that the convergence of the beam towards the focus is very low. Therefore a large distance between the entrance window and the HCF is required to obtain sufficiently large beam sizes on the window. Such that the peak intensity does not cause Kerr-lens focusing inside the window. Specifically in our case, the half-focused beam developed several hotspots, which led to strong phase distortion and a degraded beam profile in focus. Actually, propagation through air up to the entrance window already caused nonlinear phase distortions.

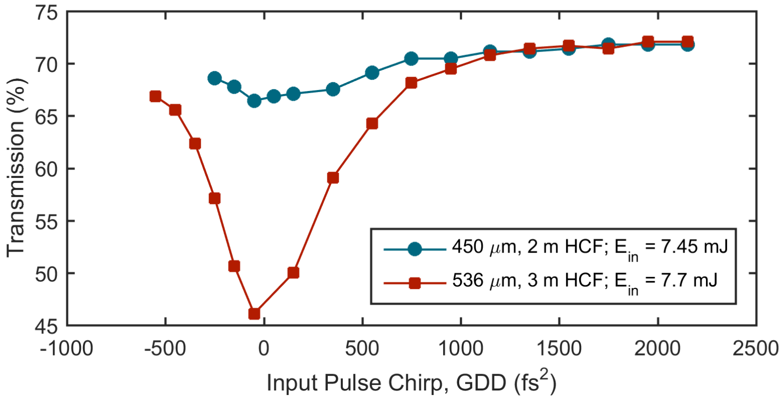

Figure 5.8. Transmission of the evacuated HCF setup with respect to input pulse chirp

We can see in Figure 5.8 the vacuum transmission of the 2 m, 450 μm and the 3 m, 536 μm fiber with respect to the pulse compression. By scanning effectively through the pulse peak intensity, a large drop in transmission could be observed for the large fiber, that made it practically impossible to use. The transmission drops to around 45%. When reducing the input energy to 2 mJ, the transmission stayed almost constant over the full chirp range.

Limited by the optical table length and the available focusing optics, the entrance window had to be installed only 95 cm away from the focus point in case of the 3 m, 536 μm fiber. This could be pushed to 135 cm for the 2 m, 450 μm fiber. For the smaller fiber, the beam size was consequently a factor of 1.7 time larger and the intensity reduced by a factor of 2.85. The estimated B-integral inside the window was 1 rad and 0.37 rad respectively, easily explaining the results of Figure 5.8.

Spectral Broadening For spectral broadening we hence used only on the smaller 2 m, 450 μm fiber. In the introduction we have seen that chirping the input pulse should not lead to a stronger maximal broadening, and we clearly observe this in Figure 5.9. We started by spectral broadening using circular polarized, compressed pulses (24 fs) in pressure gradient mode. In Helium, we observed that the transmission dropped directly when increasing the gas pressure. The pressure was increased either until 3 bar or until the beam started to break up due to filamentation. And we observed a maximum broadening factor of ~ 3 for a slight input chirp of 200 fs^2. The input pulse compression could not be determined with absolute precision and looking at the data, best pulse compression was probably somewhere between 0 and 200 fs^2.

In retrospect, this direct strong drop in transmission was likely been caused, at least partially, by pollution, which we will talk about in more detailed in the next section.

The spectral broadening did not follow the predicted shape (black line in Figure 5.9a) in part because the transmission dropped with increasing pressure. But in large part also because of the aforementioned pollution. At very low gas pressure, the pollution led directly to strong ionization and broadening. But with increasing gas pressure, this stays constant assuming a constant pollution concentration.

By strongly chirping the input pulse to 1000 fs^2, the transmission could be kept high in Neon for higher pressure. Neon has an ionization potential only slightly lower than Helium, but a twice larger nonlinear refractive index. In the end, spectral broadening did not surpass and actually came not even close to the broadening of a compressed pulse in Helium.

Due to the strong drop in transmission, the ID seemed obviously too small. Unfortunately during this implementation phase, we had no other option but to

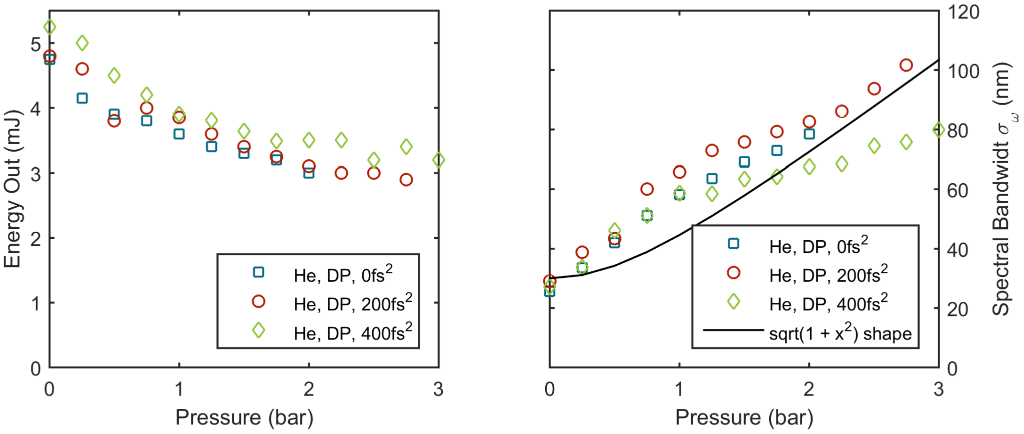

(a) Helium

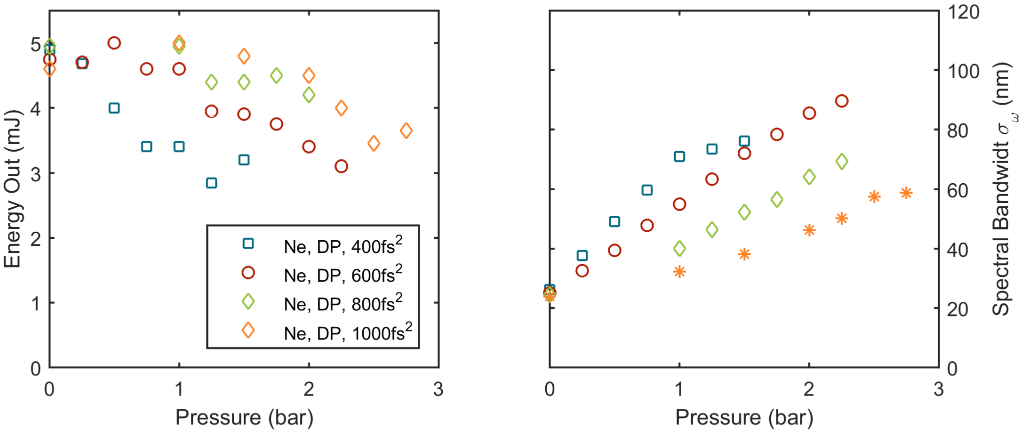

(b) Neon

Figure 5.9. Transmission and spectral broadening versus pressure for different gases and input pulse chirp. Differential pumping in the 2 m, 450 μm fiber. Input pulse energy was 7.5 mJ

try getting the best pulse out of this fiber. For this we carefully optimized the pulse compression, including higher order chirp, while trying to maximize spectral broadening and transmission.

In the end, we were able to obtain an octave-spanning spectrum, with a FTL duration of a single cycle, or 2.6 fs and an output energy of 3.4 mJ. Considering the input energy of 7.9 mJ, this is a rather lousy transmission (43%). The larger fiber should have achieved a better value. Anyway, the spectrum is shown in Figure 5.10. We can remark a well-balanced, smooth spectrum.

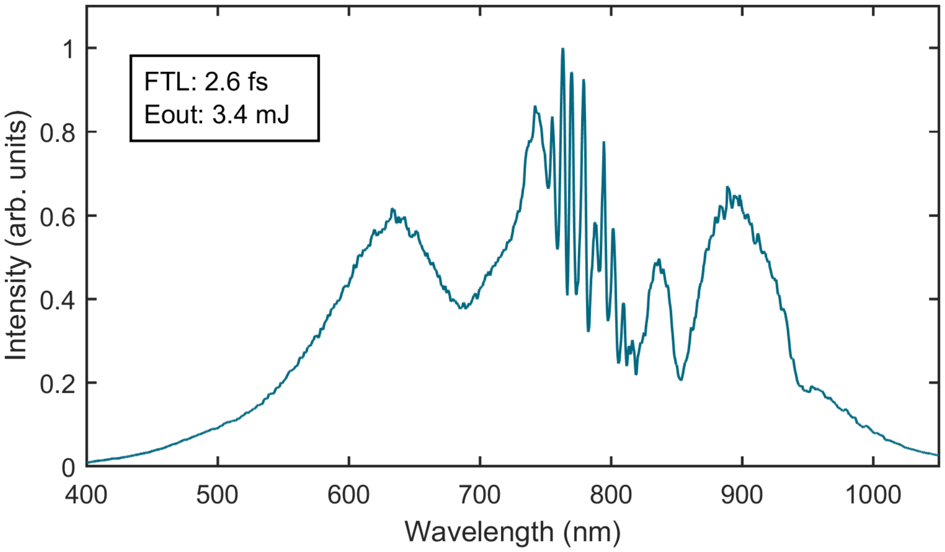

Figure 5.10. Spectrum obtained with differential pumping of 1.63 bar Helium in 2 m, 450 μm HCF. Input pulse circular polarized with 7.9 mJ and 24 fs.

Stability We also validated that the use of circular polarization increased the transmission by 20% at similar spectral broadening, indicating once more that we are operating above the limit of the 450 μm fiber. Furthermore, the spectral fluctuations were reduced from 7.8% in case of linear polarization to 4.7% when using circular polarization. For this 100 spectra were recorded at short intervals and an integration time of each sequence of 10 ms.

FROG Measurement The pulse was compressed by thin wedges and 10 CMs (Ultrafast Innovations: PC42). It was then send into a frequency resolved optical gating (FROG) device (similar to [65]) for temporal characterization. The shortest pulse duration obtained was 4.3 fs and the FROG trace is shown in Figure 5.11. We can see an excellent agreement between the retrieved and recorded FROG trace. The quality of the retrieval is also visible by comparing the retrieved spectrum and the spectrum recorded at the entrance to the FROG. The pulse duration was far from the Fourier limit corresponding to the more than octave spanning spectrum.

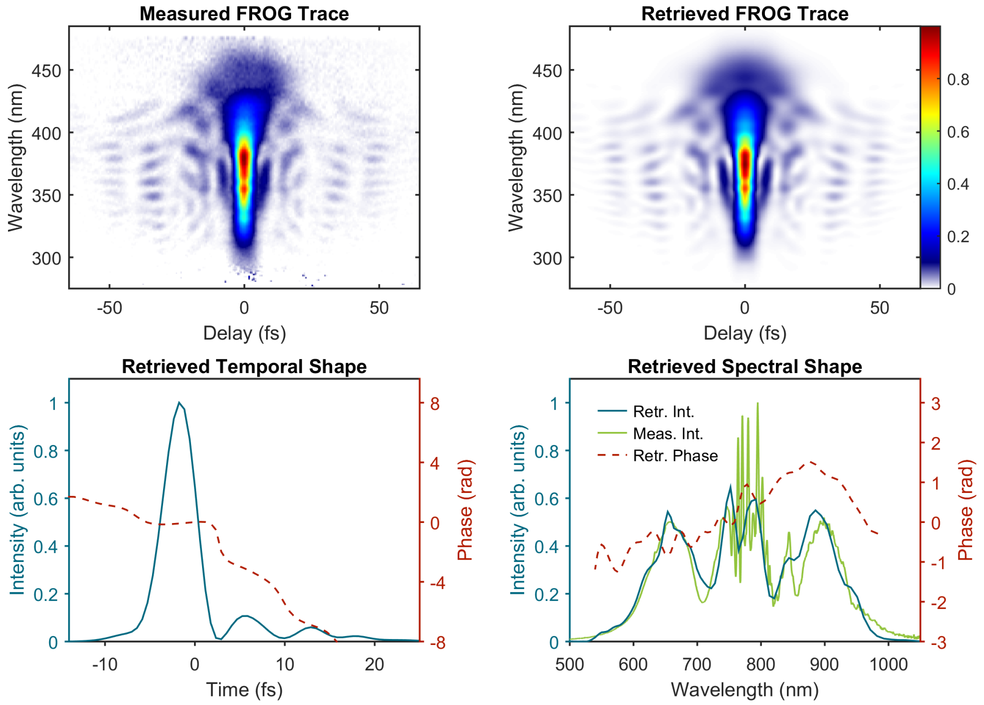

Figure 5.11. FROG measurement of compressed 3mJ pulses revealing pulse duration of 4.27 fs. Spectrum measured at the entrance to the FROG shown in light green to compare to retrieved spectrum. Retrieval error of 0.23% on a grid size of 512x512

Spatial Distribution after HCF We also noted that the spectrum inside the FROG was considerably narrower than after the fiber. This is because the single-shot FROG requires a flat top like beam profile. Consequently only a small portion of the full beam with almost constant energy distribution was expanded and used for the FROG measurement. However different spectral components have the same mode size inside the HCF and therefore diverge differently. The blue part of the spectrum will be concentrated only in the core of the enlarged beam. Sampling only a small part of the beam leads then to the observed spectral clipping. We can see the spatial distribution of the different spectral components in more detail in

Figure 5.12. We can clearly remark that the blue part was indeed centred in the core. And the spectral bandwidth is at each position considerably narrower than the spectrum of the full beam.

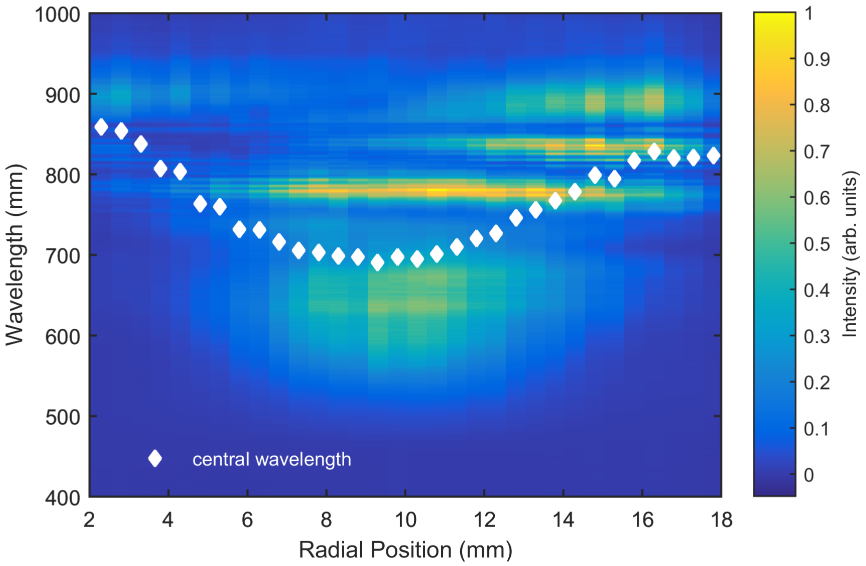

Figure 5.12. Radial spectral distribution after HCF. Spectra recorded by moving spectrometer fiber by a translation stage through the expanded beam. Concentration of blue components in the centre clearly visible. Spectral centre of mass drops from 850 nm at the side to 700 nm in the centre.

D-Scan For laser-plasma experiments the pulses are typically refocused using an off-axis parabola. Consequently, the difference of divergence after the HCF should exactly reverse itself so that in focus, all spectral components overlap again. To more accurately characterize the temporal shape of the laser pulse on target, the full beam needs therefore to be focused into a nonlinear crystal of a measuring device.

The new D-Scan device by Sphere Ultrafast Photonics sounds ideal for this measurement as it is experimentally simple and proven to be able to measure near single cycle pulses [66, 67]. Most importantly the full beam gets refocused into a second harmonic generation (SHG) crystal for characterization.

A D-Scan trace for optimal broadening conditions is shown in Figure 5.13. A pulse duration of 3.9 ± 0.1 fs was achieved. In the end the pulse duration was in part limited by the employed CMs (PC42), which have a sharp phase drop around 500 nm. In any case, directly after the CMs a pulse energy of 3 mJ could be measured leading to a pulse peak power of 0.7 TW.

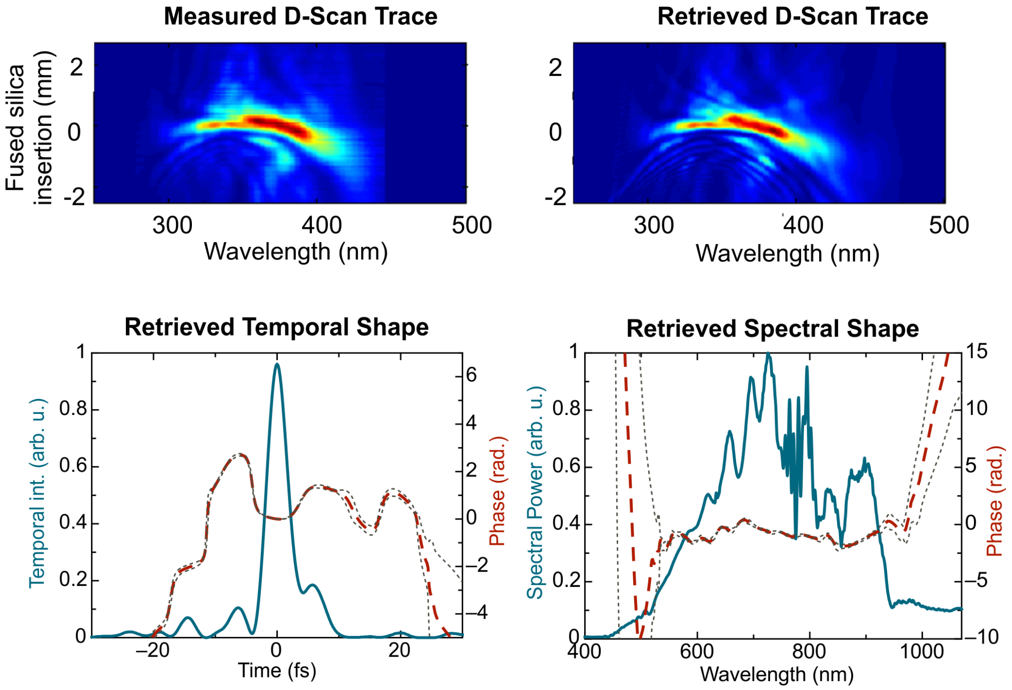

Figure 5.13. D-Scan trace for optimal HCF broadening. Pulse duration of 3.9 ± 0.1 fs. Dotted grey curves give confidence interval for the phase.

CEP Finally, the CEP stability after the HCF had to be characterized. The measurement with our home made f-to-2f interferometer was done integrating over 4 shots and then feeding back onto the oscillator in a slow loop with a cycle time of 100 ms. The CEP could be stabilized to 360 mrad RMS over the course of 10 minutes (Figure 5.14). This was not an easy task and we noted a significant increase compared to the CEP stability after the second CPA. Before the fiber the stability was 250 mrad RMS. This increase could be attributed to a certain level of photo-ionization inside the HCF and to the energy fluctuation that directly translate onto the B-integral. This phase noise usually adds up arithmetically [68]. Additionally, the pointing stability adds also a certain level of phase noise and could ideally be improved.

As the slow feedback directly feeds onto the pump power for the oscillator, it disturbs its operations. Consequently it could not be stabilized for a much longer time. A remedy would be to use more modern stabilization ideas, like a feedback on the Dazzler, which has been introduced in the previous chapter.

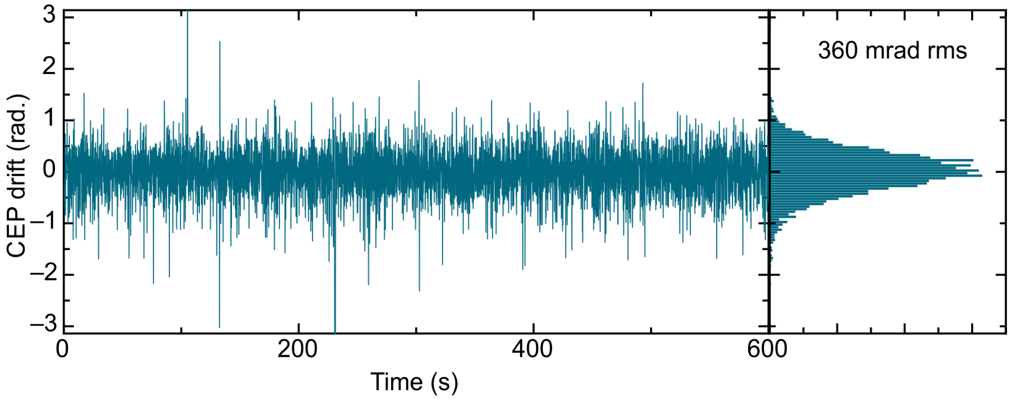

Figure 5.14. CEP stability after the HCF.

5.2.3. Conclusion

In previous experiments, including those of other groups, either not significantly more than 1 mJ or no CEP stability was achieved for a few-cycle HCF compressor. Here we showed for the first time, the generation of CEP-stable, sub-4 fs pulses with 3 mJ energy. To date, this is the highest pulse energy for CEP-stable sub-5 fs pulses. We published these results in [69].

On the other hand, the B-Integral inside the incoupling windows imposed unacceptable restrictions on our choice of the ideal HCF. The whole implementation was limited by the smaller fiber, which showed certain level of photo-ionization and self-focusing. Additionally the spectral phase and as such the pulse duration was limited by the CMs employed at that time. The next section will show how we addressed both these obstacles in a future implementation.

5.3. 2nd Implementation

After learning about the challenges and difficulties in operating a high energy post-compression setup, this second implementation was supposed to give a significant improvement in performance. Not only in hard measurable pulse characteristics, but also in easiness of daily operation.

We also have slightly improved input pulse now containing consistently above 8 mJ, but this also led to a stronger degradation of the beam profile.

5.3.1. Experimental Setup

First a simply, yet very powerful improvement was made to allow for an adjustment of the longitudinal focus position along the fiber axis. At the end of the last amplifier a telescopic beam-expander bring the beam to the final size right before the GRISM compressor. To adjust the final focus position in the range of just a few centimetre it is sufficient to add the equivalent of a very weak lens somewhere before the final focusing system. For this the second lens of the telescope is placed on a translation stage (before the GRISM). By moving this lens, the telescope is brought out of collimation, which has the same effect as adding a weak lens. Due to the thermal effects inside the GRISM, a slight change in energy out of the 2nd CPA, led to a focus shift. With this technique we could from then on easily adjust the focus position in daily operation.

To further mitigate the nonlinear effects in the incoupling window, we designed a large vacuum chamber that is directly connected to the HCF. All the focusing optics were inside this chamber. In fact this also includes the CMs for final pulse compression, so not even the large collimated beam goes compressed through any window.

Pollution inside the HCF atmosphere and therefore also of the chambers is of huge importance. Already air has a nonlinear refractive index many times higher than Helium. But in particular, the ionization level is much lower, and even more so in hydro-carbonates which easily pollute surfaces. It was for this reason critical to build the chamber to a standard that is otherwise usually only used in ultra-high vacuum applications. The Teflon tube from the gas bottle to the chamber had been even replaced by a stainless steel tube.

The beam pointing correction subsystem was also improved. With the previous system we could not stabilize the near-field without deteriorating the far field feedback performance. For this a new system from TEM-Messtechnik was integrated.

With a first calibration run, this system measures the effect each active mirror has on the far- and near-field. It then calculates the inverse transfer matrix and can then in a single step independently correct the far- and near-field. An in general better feedback electronics led to a pointing stability roughly 30% better. But very importantly, we now also actively stabilize the near-field. When the near-field changes due to thermal effects in the laser chain, the optical axis does not align any more with the fiber axis. Therefore the beam cannot any more couple efficiently into the lowest order mode and spectral broadening gets chaotic. This improvement is very important for the laser plasma experiment, which can require long beam-times in excess of 10 hours.

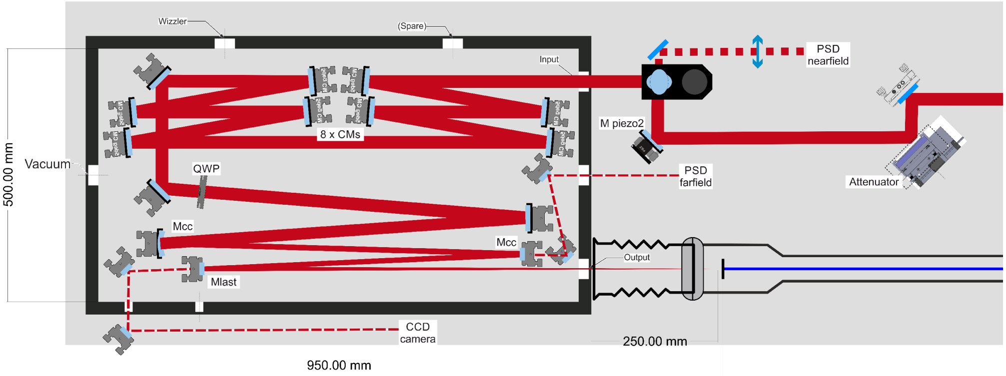

Figure 5.15. Optical layout of HCF input chamber.

The final optical setup on the input side is shown in Figure 5.15. The not fully compressed beam passed through a large aperture window into the vacuum chamber. 8 highly dispersive CMs (Ultrafast Innovations, HD58) provided roughly 2000 fs^2 of negative dispersion, meaning that the pulse travelling through the window was still stretched to around 200 fs. The B-integral was reduced therewith $\sim$ 100 times.

The polarization was then converted to circular by a QWP and the beam was brought to final focal spot size by the telescopic focusing system. A leak from the second last mirror was sent onto the position sensitive detector (PSD). And a camera monitored the real focus condition by a leak from the last flat mirror M_{last}. The beam could be block by a diffusive fused silica plate on a translation stage between the last mirror and the HCF. So the beam shape and position could be verified on camera without the risk of damaging the fiber.

For initial alignment the beam could be attenuated after the GRISM compressor by a half silver-, half un-coated wedge on a translation stage. This allowed alignment with full energy inside the GRISM – very important so it can be thermalized properly.

To maintain excellent wavefront after the HCF setup, nonlinear phase on the output side should be also prevented. Therefore a gas chamber was put in place to extend the beam before passing through a window. The setup is shown in Figure 5.16. The beam was expanded by a telescope. We had also two mirrors (BS1 and BS2) on translation stages that could be moved inside the beam-pass to couple it out for diagnostics. The first sends the divergent beam straight out and allows for HCF alignment and energy measurements. The second mirror sends the beam onto a near- and far-field camera as well as on a spectrometer. Two active mirrors allow for adjusting the beam onto the near- and far-field references. An ultra-broadband QWP (Bernhard Halle Nachfl., 450-1050 nm) turned the beam back to linear polarization.

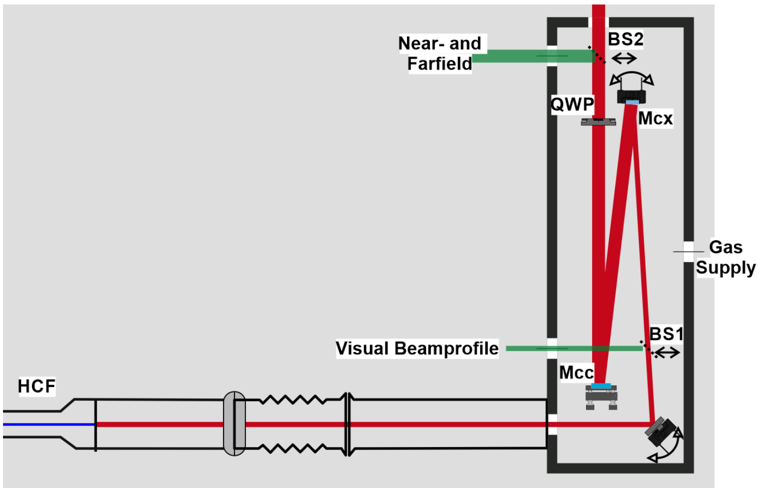

Figure 5.16. Optical layout of HCF output chamber.

In the end the fiber length was limited by the damage threshold of the first mirror after the fiber. To be able to install the longest fiber, we performed damage test on silver mirrors from different manufactures. But in the end they all showed a very similar damage threshold. The Layertec and Femtolasers enhanced silver mirrors where both at around $\sim 140\,\mathrm{mJcm^{-2}}$. This should have been enough for the 3 m long fiber, which had a predicted fluence level of $\sim 90\,\mathrm{mJcm^{-2}}$, but with this fiber the last mirror consistently got damaged after a short while. Likely because the spectrum during the test was narrower and did not reach as far in the blue, where the silver absorbs stronger. A 2.7 m fiber would have been probably ideal, but we settled for 2.5 m. The HCF is summarized in Table 5.3. It has a lower value for $\frac{\lambda L}{A}$ than the fiber used during the 1st implementation.

For this implementation also new chirped mirrors for final compression have been bought. They (Ultrafast Innovations, PC70) provide a slightly higher bandwidth

Serial Number	core diameter, ID (μm)	length (m)	$\frac{\lambda L}{A}$
#60	536	2.5	~ 8

Table 5.3. HCFs for the second implementation phase.

in the infra-red, but more importantly have a better behaved phase further in the blue.

5.3.2. Results

One of the main question is of course, if we can now use the large fiber without degradation from the nonlinear effects in the input window. Figure 5.17 compares the current implementation to the previous setup without vacuum chambers. No drop in transmission around pulse compression is present any more. But there is still a trend of lower transmission towards negative pulse chirp. This is normal and comes from the nonlinear effects inside the second CPA in particular inside the GRISM. And since we have slightly more energy available, this is probably also the reason for the general lower transmission. The beam profile has a slightly lower intensity overlap with the fundamental mode of the fiber.

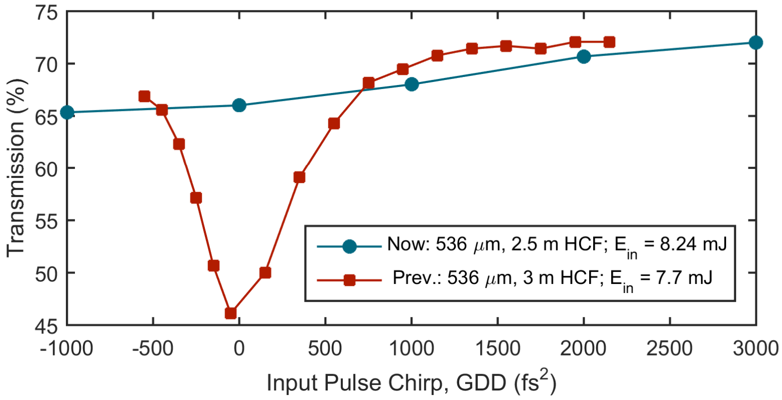

Figure 5.17. Transmission of the evacuated HCF setup with respect to input pulse chirp. Comparison of current system to previous implementation without vacuum chambers.

Spectral Broadening The second major question was, if we could obtain controlled and smooth SPM broadening without losses due to self-focusing and ionization. For this we continuously increased the gas pressure and calculated the transmission and recorded the output spectrum. Figure 5.18 shows this scan, which stands in sharp contrast to the previous implementation that was shown in Figure 5.9. The pressure scan shows a flat transmission curve without any major drop. In fact even at the highest pressure the transmission did not drop more than 8%. Also the spectral broadening showed a controlled development very close to the theoretical $\sqrt{1+x^2}$ curve. Only for the highest pressure in case of a compressed input pulse we see a stronger increase in broadening, which indicates likely the onset of self-focusing. This would also explain the energy drop for this data point.

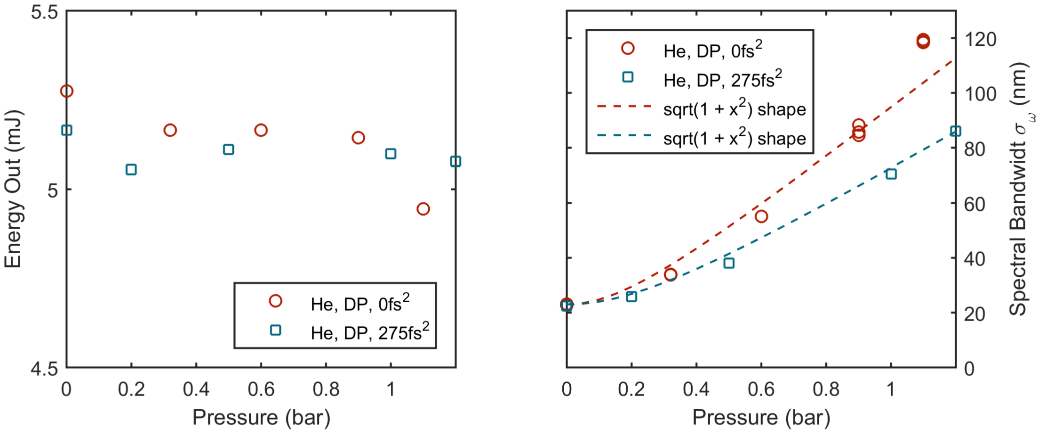

Figure 5.18. Transmission and spectral broadening versus pressure in Helium for two different input pulse chirp. Differential pumping in the 2.5 m, 536 μm fiber. Note: Energy scale starts not at 0.

In conclusion the scaling law seems to be well respected and we get 20% more broadening at 64% higher energy in comparison to the previous implementation!

D-Scan For temporal characterization we trusted again in the D-Scan. This time the D-Scan is positioned under vacuum. In fact, the beam goes directly from the output gas chamber into a large vacuum beamline, that will be the topic of Chapter 6. This also meant no propagation through air and therefore fewer dispersion on the pulse. Accordingly we could employ fewer CMs, which should result in a better phase behaviour. A total of twelve PC70 CMs have been used.

The shortest pulse duration of 3.40 fs has been obtained at a gas pressure of 1800 mbar, but then self-focusing effects led already to a significant energy drop. The D-Scan trace is shown in Figure 5.19. And we see clearly that the pulse duration is limited by the bandwidth as well by the phase of the chirped mirrors.

We usually operate rather in the regime with the highest peak power, which occurs at a gas pressure around 1200 mbar to 1400 mbar, just before self-focusing becomes prominent. At 1400 mbar we obtained a pulse duration of 3.53 fs (D-Scan trace shown in Figure 5.20). On a usual day with good laser performance we get a pulse energy of 5.1 mJ after the HCF for this pulse duration. This drops to 3.72 mJ after the full set of CMs[1] and corresponds consequently to a compressed pulse with a peak power of 1.06 TW. The record peak power obtained was 1.13 TW. With this achievement we reached our goal of TW few-cycle pulses with a kHz laser chain.

Going after the HCF out-coupling chamber directly into a vacuum beamline also helps us with the management of the third order phase of the pulse. In Figure 5.21 we see two D-Scan traces in similar fiber condition, but one with the beamline under air and the other in the evacuated case. We can clearly see that the trace is more horizontal for the vacuum condition. This means that the pulse had less TOD and resulted in a shorter pulse duration. Air has a TOD to GDD ratio that is different to that of fused silica

---

[1] As it was not possible to measure the pulse energy under vacuum, this value was deduced from the measured transmission (HCF until after CMs) in air (0.8) and the energy measured after the HCF sampled through the BS1 and the first exit window.

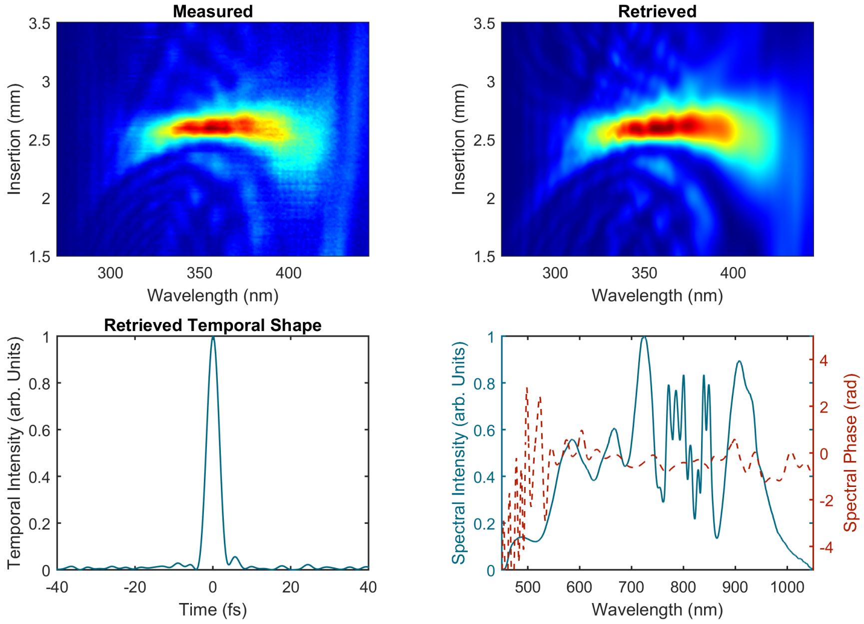

Figure 5.19. D-Scan trace of 3.40 fs pulse at a gas pressure of 1800 mbar.

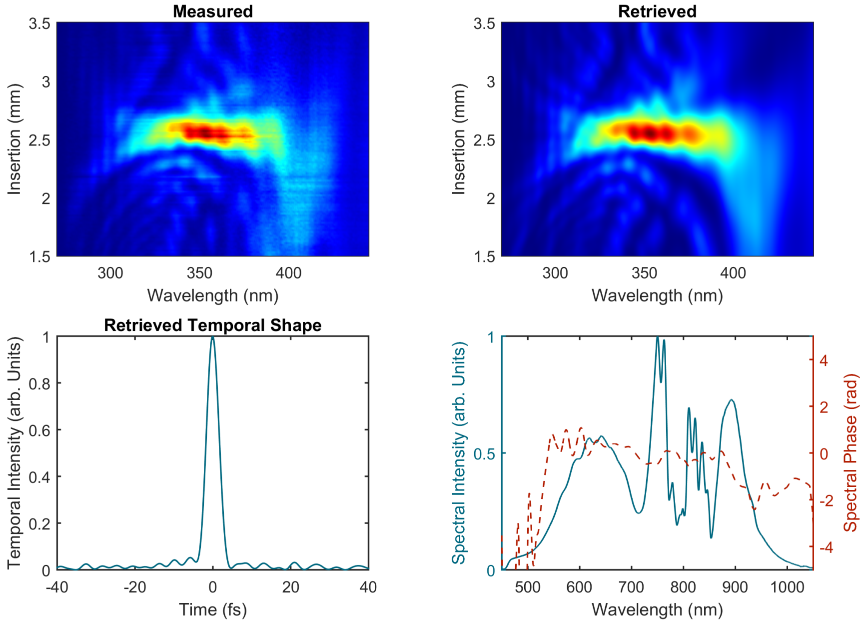

Figure 5.20. D-Scan trace of 3.53 fs pulse at a gas pressure of 1400 mbar.

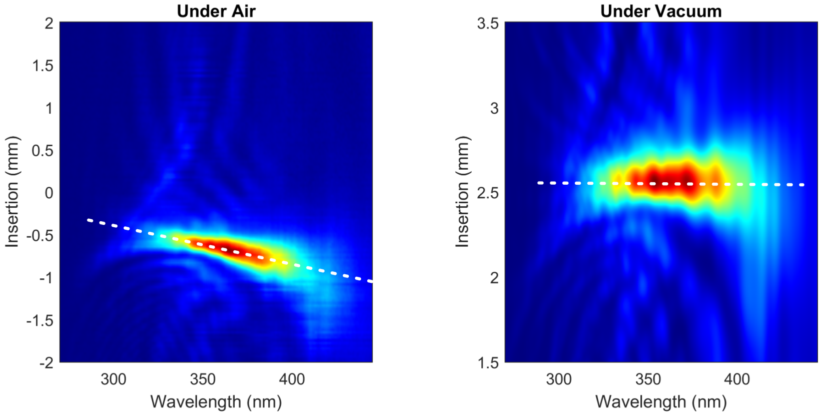

Figure 5.21. Comparison of D-Scan trace with beamline under air and under vacuum. TOD clearly visible by tilted trace for the case of the beamline under air.

Tuneability Thanks to the well-respected scaling law, we can actually tune the pulse duration continuously from the fundamental 24 fs to close to 3.5 fs and this while keeping the output pulse energy almost constant. In Figure 5.22 we can see 5 D-Scan traces obtained sequentially while increasing the gas pressure. The pulse energy stayed almost constant for all pulse durations.

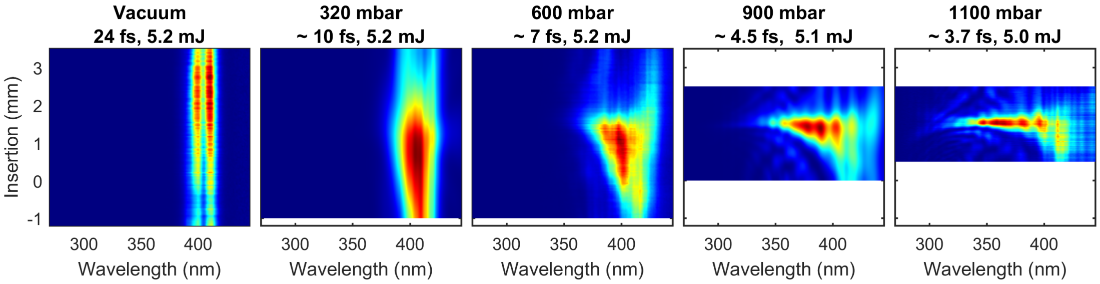

Figure 5.22. D-Scan trace with increasing gas pressure in HCF. Displayed energy from pulse directly after HCF.

Pollution The improvements in cleanliness and high vacuum compatibility have paid off. Particular the replacement of the Teflon tube with a complete stainless steel tubing system allowed us to operate at low gas pressures and therefore made the tunable fiber possible. After a long pause, it still becomes necessary to flush the system. This usually becomes evident when putting only 50 mbar inside the fiber and the transmission already drops drastically and the spectrum broadens. After flushing and re-pumping the system 50 mbar did not show any effect. The system then remained clean for the rest of the day.

Spatial and Spectral Homogeneity Due to the spatial filtering properties of the HCF, we believed the wavefront should be flat and the spatial distribution should be homogeneous. This is of course with the exception of the predicted wavelength dependence of divergence as discussed in the previous section.

In Figure 5.23 we see a spatially resolved spectrum of the refocused beam with the HCF under vacuum. We see a slight kink of the spectral components towards the lower wavelengths. This is likely coming from the GRISM compressor. It was extremely difficult to align the GRISM compressor so that all interfaces were parallel. This kink was likely coming from a never perfect alignment. In fact, we sometimes needed to tweak the tilt of the last prism to correct the beam profile before the fiber. The fiber filter effect grows with increasing spatial frequencies. Lower order defects on the other hand are not filter very well. Therefore a part of the GRISM defects were seen until the end of the chain.

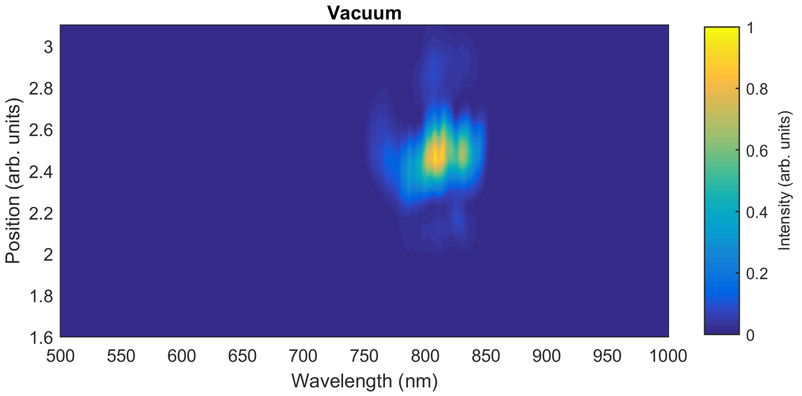

Figure 5.23. Imaging spectrum taken at focus. HCF under vacuum.

But this does not cause problems at broad spectrum. At full gas pressure we got a fairly flat spectral distribution (Figure 5.24). The different spectral components were refocused to a similar spot size, therewith reversing the differential divergence.

CEP At the end, only the CEP stability was to be proven. Unfortunately the first pump laser of the amplifier chain (Jade 2 for Femtopower) became very unstable. As the CEP is directly linked to the amplified power by the nonlinear B-integral, it became very hard to stabilize it. During the first implementation we had a CEP

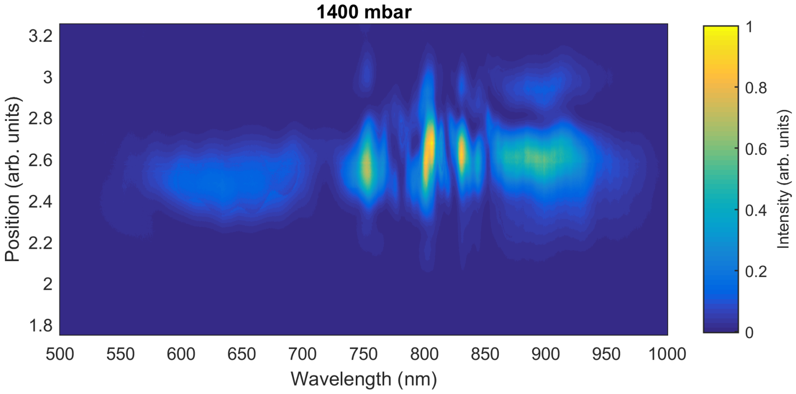

Figure 5.24. Imaging spectrum taken at focus. HCF pressure 1400 mbar.

phase error of 360 mrad RMS. With the new vacuum in-coupling setup, the large HCF diameter and vacuum beamline we would expect an improvement. Because of the pump laser this was not the case though and we measured a CEP phase error of more than 500 mrad RMS and in fact it became difficult to talk at all about a stable CEP.

By now the pump laser has been replaced with an Ascend from Spectra Physics, but we have not gotten to a full system test yet. First results on the Femtopower look promising though and we measured a single shot CEP stability of 180 mrad RMS with the new Fringeezz-Dazzler combination.

5.4. Conclusion and Outlook

In this chapter we have seen how to effectively overcome the gain narrowing limit of traditional amplifier by spectral broadening the pulse in a gas filled HCF. With this technique we were able to reach near single cycle (3.5 fs equals 1.38 cycles at 760 nm central wavelength) pulses with a peak power in excess of 1 TW. To the best of our knowledge, this is the largest pulse power for CEP-stable sub-5 fs pulses ever achieved. The beam shows a good spatial profile that should allow focusing down to a few λ spot size to reach the relativistic intensity regime.

For our group, these results are a big leap forward in pulse peak power but also in duration, having reached near-single-cycle pulses. It well justifies the enormous effort in upgrading the laser chain and HCF setup. Previously 1.6 mJ, 4.8 fs (0.3 TW) had been reported in 2011 by X. Chen, a former group member[61].

Ideally a slightly longer HCF could be used as we are operating very close to the self-focusing limit. In a longer fiber the gas pressure could be reduced while maintaining similar spectral broadening. This would reduce consequently self-focusing issues. But unfortunately the current laser lab space does not allow this.

Compressing higher pulse energies will require ever larger HCFs. In fact we have seen that it scales linear. This unfavourable scaling law will eventually exclude the HCF post-compression technique for new high power laser chains. A very interesting new approach to HCF compression might prevent this. Hermance *et al.* split the input pulse temporarily by a birefringent plate. Both pulses travelled then through the HCF and the spectrally broadened pulses were eventually recombined [70]. Doing this, the dimension of the HCF can be reduced by the number of replicas. So far it has been demonstrated successfully with 4 pulse replicas [71].

6. Integrated Vacuum Beamline for Laser-Plasma Experiments

For controlled laser plasma experiments the main laser beam needs to be accurately controlled and delivered onto a target at high intensity. This chapter deals with the beam-shaping, control and final delivery onto a tight focus by a low F/# parabola.

When dealing with near-single-cycle, intense pulses already propagation trough air considerably disperses the pulse. Each meter of propagation through air would require an additional CM. In total we had roughly 12 m of propagation from the HCF chamber until the parabola and therefore clearly requiring a vacuum setup just from the linear pulse propagation perspective. We have also seen in Chapter 5 that the CMs do not properly compensate the TOD of air.

But once the pulse is compressed it can also cause nonlinear effects in air, which would degrade the wavefront quality. Not to speak of that the pulse needs to travel eventually through a glass window to reach the vacuum around the laser plasma interaction.

An additional benefit of going directly into vacuum after the HCF setup comes from making the beam intrinsically more stable as any influence from air fluctuations is shielded. By having the whole beamline under vacuum gives us also the possibility to measure the spectro-temporal pulse properties at basically any point and it should give us an accurate estimate of the final condition in focus.

6.1. Optical Layout

We see the optical setup of the beamline to scale in Figure 6.1. The p-polarized beam enters the vacuum through a single 3 mm thick, 30 mm clear aperture AR-coated window directly from the HCF setup at the bottom. It travels through a wedge pair and is then compressed by CMs. The wedges are on a translation stage to tune the compression and one wedge is on a rotation stage to introduce spatio-temporal coupling (STC). The simultaneous translation of both 5°, 25 mm long fused silica wedges are sufficient to introduce $\pm 75\,\mathrm{fs}^2$ of second order dispersion. Ideal for direct use in a D-Scan measurement for sub-10 fs pulses.

Currently only 12 PC70 CMs (Ultrafast Innovations) are necessary to compensate the dispersion from the SPM inside the HCF and a total of around 10 mm

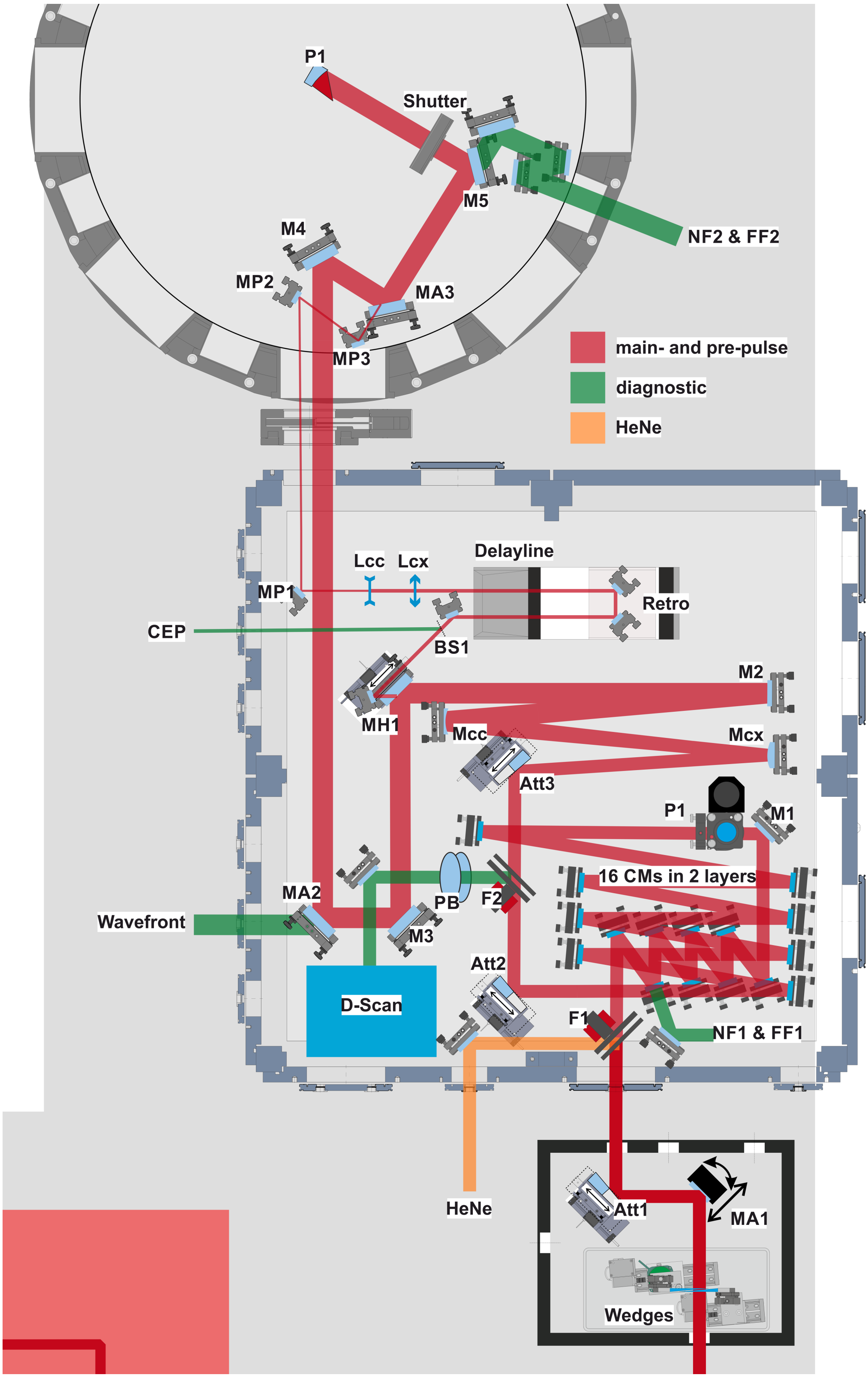

Figure 6.1. Integrated vacuum beamline for solid target laser plasma experiments. Laser enters the first vacuum chamber on the bottom.

M1 - M4	flat mirror for main beam
Wedges	Two 5 deg FS wedges on translation stage for dispersion scanning. One wedge on rotation stage for wavefront rotation (lighthouse) in the horizontal plane.
MA1	Active mirror with pitch and yaw movements for far-field alignment and sideways translation for near field alignment in the horizontal plane after a wavefront rotation has been applied by the wedges.
Att1 - Att3	Rectangular wedge on a translation stage with half the surface coated in silver and half left untreated. This that allows to either fully reflect or to attenuate the beam to around 0.7% per device. This allows for a total attenuation of $3 \cdot 10^{-7}$.
HeNe	High spatial quality Helium-Neon alignment laser.
F1	Flip to switch between the HeNe alignment laser and the femtosecond beam.
CMs	Up to a maximum of 16 PC70 (Ultrafast Innovations) chirped mirror in two layers. Currently 12 CMs are in use.
NF1 & FF1	Near- and far-field reference. Optical system focuses a leak from the second CM onto a camera for the far-field reference and images the plane of MA1 onto another camera for the nearfield reference.
P1	Periscope. Can be changed for a HWP and rotating periscope instead of M1 to allow vertical wavefront rotation while keeping the polarization.
Mcx & Mcc	Beam-expanding telescope. Brings the final beam-size to 33 mm FWe2.
M2	Can be replaced by a deformable mirror.
MH1	Flat silver mirror with a 7 mm hole to separate the pre-pulse. Mirror is on a translation stage to change the energy of the pre-pulse by moving the hole through the main beam.
MA2	Active mirror with pitch and yaw movements for near-field alignment onto MA3. Additionally coated with a semi-transparent (0.1%) silver layer for wavefront measurements outside the chamber. Slightly wedged to prevent double reflection.
MA3	Active mirror with pitch and yaw movements for final far-field alignment. Additionally recombines pre- and main-pulse.
M5	Flat mirror coated with a semi-transparent (0.1%) silver layer. Slightly wedged to prevent double reflection.
Shutter	Fast shutter for sequence control.

Table 6.1. Legend for Figure 6.1.

Parabola	Low F# parabola for tight focusing.
NF2	Nearfield reference of MA3 plane to monitor position and correct recombination of main- and pre-pulse.
FF2	Final farfield reference to monitor focus position and proper overlap between main- and pre-pulse.
BS1	Beamsplitter in the pre-pulse arm for CEP measurement outside the chamber
Delay line	High precision translation stage to control the delay between pre- and mainpulse. Range: 660 ps; Repeatability: 7 fs
Retro	3 dimensional retro-reflector to maintain pre-pulse beampointing without concern for translation stage wobble.
Lcc & Lcx	Beamsize reducing telescope for final pre-pulse focal spot size adjustment.
MP1 - MP3	Flat mirror for pre-pulse. MP1 and MP3 are active mirrors for near- and farfield alignment.
F2	Flip to send the compressed, full energy beam towards the D-Scan device.
PB	Periscope with wedges for attenuation. Wedges at Brewster's angle for orthogonal polarization to enhance the polarization quality.
D-Scan	Spectrometer for fundamental and SHG in a 5 μm thick BBO crystal. Excellent input beam polarization quality required as a polarizer blocks the fundamental before the SHG spectrometer.
	All mirrors on the main beam are enhanced, high reflectivity, low dispersion silver mirrors either from Femtolasers or Layertec.

Table 6.1 Continued Legend for Figure 6.1.

propagation through material (3 mm window, 6.5 mm wedges in zero position, 0.7 mm QWP after HCF). The layout allows for an additional 4 CMs in case other transmissive optics are installed. A leak from the second CM is send onto two imaging cameras for an accurate near- and farfield reference for beam alignment, which can be controlled by an active mirror inside the wedge chamber.

The beam is then expanded by a telescope to the final width of 33 mm at FWe2, which optimizes the peak intensity in focus for our parabola of 44 mm clear aperture, but of which only 40 mm have a specified surface quality. We use a 1.3 F/#, $\sim 30°$off-axis parabola from Winlight with an effective focal length of 54.4 mm.

Right before the parabola a high speed shutter with an opening time less than 15 ms allows for sequence control. Having it right in front of the parabola ensures all previous optics are in a thermalized state and the focus plane does not shift during a sequence. Though with the current fluence on the optics, this would not have been necessary.

Attenuators To image the laser focus in conditions as close as possible to reality, the beam need to be attenuated to a level safe for objective or camera. For this installed three attenuators at the beginning of the beamline. The design consist of a long fused-silica wedge on a translation stage, where half the surface is coated by an enhanced silver layer and half side is left untreated. The laser normally reflects off the silver side, but by translating the wedge, only 0.7% is reflected off the untreated side at an incidence angle of 45°. With a total of three attenuators the full beam can be attenuated by $3 \cdot 10^{-7}$.

This method of attenuation ensures no distortion of the wavefront and a rather flat spectral response. The use of high precision translation stages was supposed to not alter the beam direction, which is important when focusing with a parabola and would lead to astigmatism. But the attained wobble of $\sim 100\,\mu$rad was not small enough and therefore the beam direction needs to be corrected by the farfield reference each time the attenuator status is changed.

Deformable Mirror Mirror MA2 is slightly wedged and coated by a weakly transmissive silver layer that lets 0.1% of light through (at 500 nm). This leak is send out and can be used for wavefront measurement. To correct any aberrations, mirror M2 can be replaced by a deformable mirror. We tested the ILAO from Imagine Optic which comes additionally with an iterative algorithm to optimize the final focus.

But this also adds a lot of complexity, and since the beam profile is already very good thanks to the HCF and its spatial filtering, this option was not used during the experimental campaigns.

6.1.1. D-Scan

For temporal characterization we use a D-Scan device from Sphere Ultrafast Photonics, because of its simplicity and easy alignment. The measuring head is under vacuum where the SHG signal is created. Both the fundamental and the SHG spectra are then fed out with a fiber to spectrometers outside.

Having the D-Scan under vacuum is only possible because it is so easy to align. Just with 1 motorized mirror, the signal going into the SHG fiber can be optimized, which concludes the alignment.

Measuring under vacuum is very important and ensures to measure the pulse properties optically as close as possible to the real conditions on target. After the point of measurement only enhanced, low dispersion silver mirrors (except the parabola) are used so very few dispersion is introduced. This is particular important with such a broad spectrum, where a GDD of only 8 fs^2 or the equivalent 0.2 mm propagation in fused silica would already double the duration of a 3.5 fs pulse.

The beam is send into the D-Scan measuring head by a flip just after the CMs. It is then attenuated by two wedges installed on a periscope and a 55°angle of incidence. This way the wedges operate in s-polarization and attenuate the beam. The angle of incidence is chosen so that the unwanted polarization (p-pol) is at Brewster's angle. Inside the D-Scan measuring head a polarizer filters out the fundamental beam after SHG and it is very crucial, that the fundamental is well filtered. Therefore a perfectly linear polarization is required. But since we operate the HCF in circular polarization the finite retardation error of the waveplates degrade the polarization quality.

6.1.2. Pre-pulse

For controlled solid target HHG experiments one requires a prepulse to generate the right plasma conditions. In general the prepulse creates a plasma that then expands into vacuum and at a defined delay the main pulse arrived and interacts with defined plasma gradient. Therefore the pre-pulse needs to be intense enough and be synchronized to the main pulse. Furthermore it should create an plasma that is homogeneous to the mainpulse and expands equally.

For this we installed a mirror with a small cylindrical hole at 45°on a translation stage that lets pass a 7 mm cut-out of the main beam. By translating the mirror and moving the hole effectively through the radial beam profile of the main pulse we can change the pre-pulse energy from $\sim 0\,\mu$J to around 170 μJ. For our experiments we usually settled for 100 μJ

To adjust the delay between pre- and mainpulse, it is then reflected off a retro-reflector on a high precision translation stage. The retro-reflector ensures that the beam is send at the same angle out as is, i.e. no wobble from the translation stage is transferred onto the pointing of the pre-pulse.

A telescope reduced the beamsize so that the focus is large enough to generate a homogenous plasma for the mainpulse. We see a size comparison of the focused main- and pre-pulse in Figure 6.2. At 100 μJ we get a fluence of around 50 $\mathrm{J\,cm^{-2}}$ in focus.

Eventually both pulses are recombined by another holed mirror.

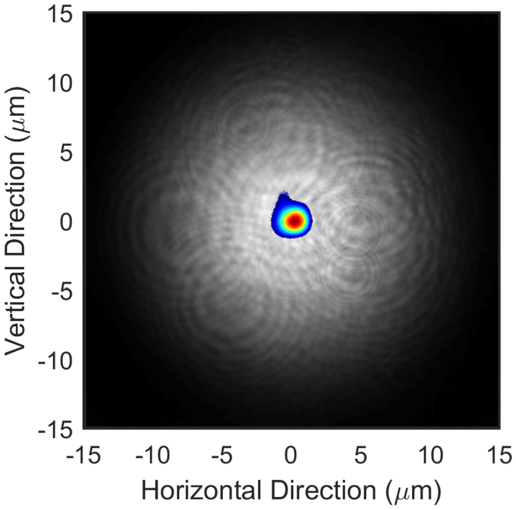

Figure 6.2. Relative size comparison of pre- and mainpulse.

Online Spatial Monitoring As the overlap is so crucial, we added another leaky mirror together with a near- and farfield imaging system just before the parabola. This way the pointing of the pre-pulse can be corrected on the fly should it have deviated. But this additional beam monitoring is also very useful to align the main pulse during the daily routine. And also to change, for example, only the nearfield, to direct the XUV emission. We see the two images from the far- and nearfield camera in Figure 6.3.

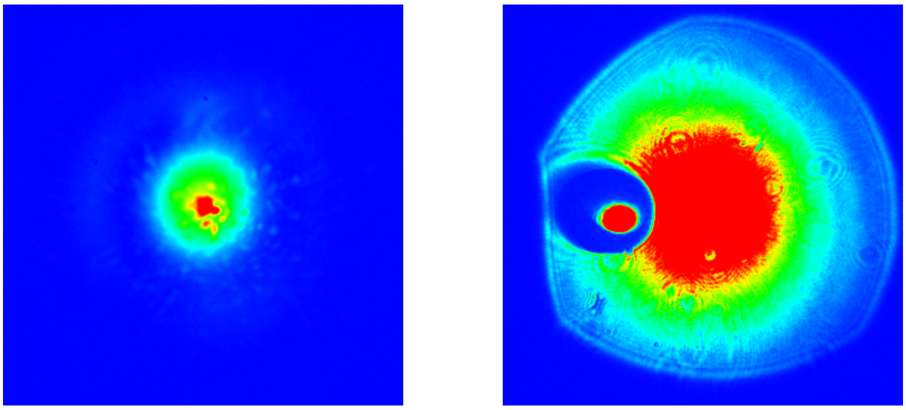

(a) Farfield **(b)** Nearfield

Figure 6.3. Final beam monitoring for position and pre-pulse overlap with mainpulse. For the farfield the mainpulse has been selectively attenuated.

6.1.3. CEP

For the relative CEP measurement we use a home-made f-to-2f interferometer with a fast spectrometer from Fastlite (Fringeezz) that can feed back directly onto the Dazzler at half the laser repetition rate. As the spectrum is already over octave spanning, we do not need to broaden it prior to SHG inside the f-to-2f interferometer and we therefore require only rather few energy. But unfortunately also no suitable broadband beam-splitter exists that has a low reflectivity and does not affect the mainpulse. We therefore rather introduced a wedged beamsplitter in the pre-pulse arm with a reflectivity around 4% (uncoated fused silica at close to normal incidence). As the beam after the fiber has the blue components in the centre, the pre-pulse must not be generated too far at the edge. This beam-sample is then send outside and directly fed into the f-to-2f interferometer.

6.1.4. Spatial-Chirp and Wavefront-Rotation in Focus

In the next part we will see how a spatio-temporal coupled light field can lead to the generation of single attosecond pulses. In particular we are talking about a linearly, spatially dispersed focus, where the different spectral components focus along a line. This created an elongated beam profile and a temporal wavefront rotation as shown in Figure 6.4.

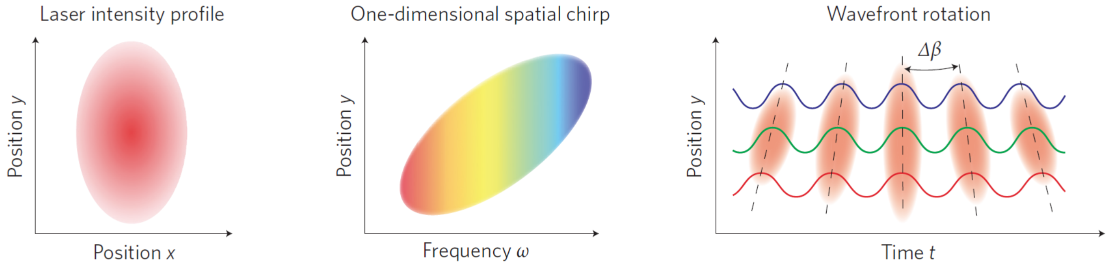

Figure 6.4. Angular dispersion leads to an elongated beam profile in focus (left), where the different spectral components do not focus in the same spot, but rather are swept along the profile from red to blue (middle). In the temporal domain this is equivalent with a wavefront rotation (right). Reprinted from [72]

Experimentally this can be easily accomplished by tilting one of the two wedges for pulse compression (D-Scan wedges). By doing so, the angular dispersion of the first wedge is not compensated and a residual dispersion remains. This means that the different spectral components have a slightly different k-vector and focus therefore in different spots.

The difficult part is, that this needs to be done under vacuum with high precision and control of the laser beam. In fact, while rotation one wedge, this also deflects and moves the laser beam. For this we installed a near- and farfield monitor after the wedges and have a motorized mirror on a translation stage. This way, we can correct horizontal displacement and angular tilt directly after the wedge setup.

The actual dispersion is then measured with an imaging spectrometer directly in focus.

6.2. Final Laser Paramteres at Focus

In conclusion we can deliver high quality, high contrast pulses onto a tight focus for solid laser plasma interaction. The contrast has not been verified at full spectrum, but only the coherent contrast can change.

In Figure 6.5 and Figure 6.6 we see a typical beam profile of the main focus with a width of 1.7 μm FWHM. 40.8% of the pulse energy was enclosed in the FWHM area of the beamprofile. A fairly good value. For comparison, an ideal Gaussian beam has 50% of its energy inside its FWHM area.

The vacuum beamline has a transmission from after the CMs until the parabola of around 80%. This leaves from a compressed pulse energy of typically 3.5 mJ after the CMs around 2.9 mJ before the parabola. For an intensity estimation we subtract generously another 15% for parabola losses and assume 2.5 mJ in focus. By taking the real beam profile into account, but assuming a FTL Gaussian pulse, we get a peak intensity of $1.6 \cdot 10^{19}\,\mathrm{W\,cm^{-2}}$ equalling to a $a_0 = 2.8$. This is clearly an upper limit as the real temporal profile and possible STC are not taken into account. In Table 6.2 we see a summary of typical laser durations and corresponding intensities on target. We are clearly in the relativistic regime with a normalized vector potential ranging from around 1 to 2.8 depending on pulse duration.

Due to the principle of HCF post-compression, it is not possible to easily change the pulse energy. If the double CPA output energy were to be reduced, the HCF could not provide sufficient spectral broadening. And after the HCF it is not trivial to install a broadband variable attenuator for the full bandwidth and without affecting the pulse negatively. The only possibility we have is by closing an iris

Pulse Duration (fs)	24	10	7.5	5	3.5
Intensity in focus ($\cdot 10^{19}\mathrm{W/cm^2}$)	0.24	0.58	0.77	1.15	1.64
a_0	1.1	1.6	1.9	2.3	2.8

Table 6.2. Upper limit estimates for laser intensity and normalized vector potential in focus for different pulse durations.

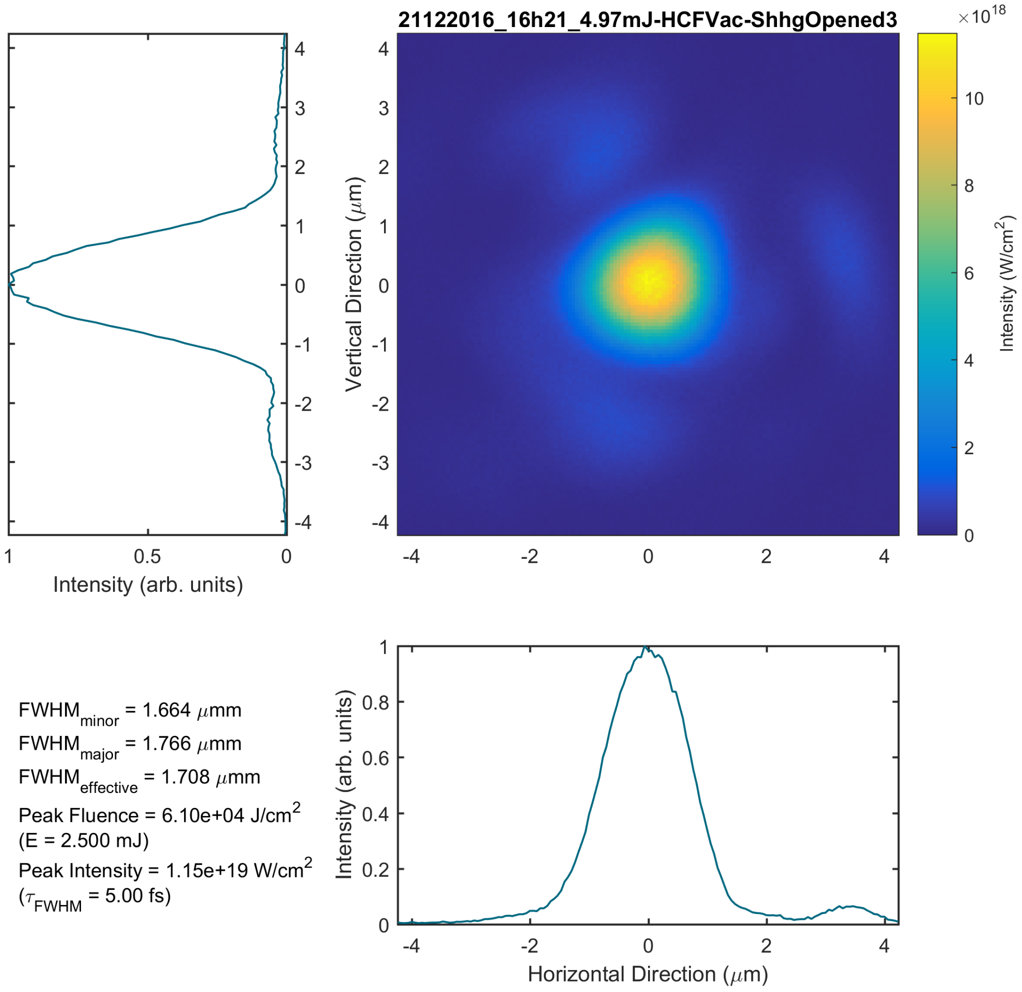

$\text{FWHM}_{\text{minor}}$ = 1.664 μmm
$\text{FWHM}_{\text{major}}$ = 1.766 μmm
$\text{FWHM}_{\text{effective}}$ = 1.708 μmm
Peak Fluence = 6.10e+04 J/cm^2
(E = 2.500 mJ)
Peak Intensity = 1.15e+19 W/cm^2
(τ_{FWHM} = 5.00 fs)

Figure 6.5. Typical beam profile in focus after the parabola.

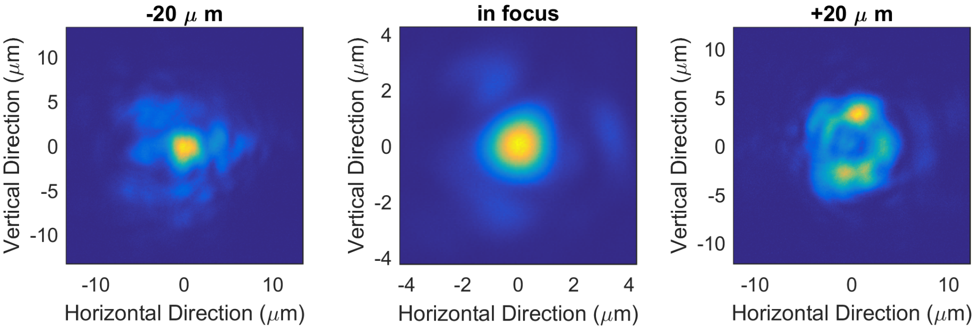

Figure 6.6. Caustic of a typical beam profile in focus after the parabola.

inside the beam, though this also changes the beam width and increases the focal spot size. Therefore we installed a 22.5 mm and a 15 mm iris on a flip to reduce the energy to 50% and 25%, as well as to reduce the intensity to 42% and 11% respectively.

Part II.

Relativistic HHG and Electron Acceleration on Solid Targets

7. Solid Laser Plasma Interaction

Solid density laser-plasma interactions are a fascinating research field with specific properties in the vast parameter space of plasmas in general, ranging from very low density and low energy plasmas in interstellar space to the highest densities and electron temperatures in cores of stars. And also fusion energy research belongs to this fourth state of matter. As explained in the introduction, this medium also provides unique opportunities to generate the shortest ever light pulses to probe ultrafast processes.

7.1. Fundamentals

When an intense laser pulse hits a solid surface it quickly ionizes it and interacts with the created plasma in a nonlinear way. In the introduction (Chapter 2) we only talked about linear wave propagation, but in a regime of a high intensity laser interacting with a gradient plasma new phenomena appear. Energy can be transferred onto the plasma and consequently can lead to particle acceleration, plasma wave excitation and high harmonic generation.

In this thesis, we do not want to go in-depth into laser plasma physics, but rather view it from an optical perspective by only treating the necessary plasma fundamentals. For this we start by looking at the vacuum plasma interface onto which the laser is focused. We always talk about a p-polarized laser pulse incident at an oblique angle. In particular during our experiments, the beam was focused at 55°onto an optical fused silica surface (maximum electron density roughly$400n_c$).

The initial plasma is either created by the rising edge of the main pulse or for more controlled experiments by a separate but synchronized pre-pulse. The single photon energy at our wavelength is only around 1.6 eV and therefore too low to ionize fused silica directly. But with increasing intensity multi-photon ionization (MPI), tunnel ionization and eventually barrier-suppression ionization (BSI) becomes possible, where the laser electric field deforms the Coulomb potential so much, that the electron is freely accelerated away from the core. At our pre-pulse intensity, usually around $1 \cdot 10^{15}\,\mathrm{W\,cm^{-2}}$, the first 5 electrons of SiO_2 are directly ionized by BSI. The exact ionization state is not of great importance. Part of the pre-pulse energy is transferred to the electrons and we can assume that it is proportional to the pre-pulse fluence around the usual intensity [73]. The initial ion temperature is on the other hand close to0 eV, but the electrons quickly transfer energy to the ions by collisional heating.

At the critical density, the plasma becomes opaque to the laser wavelength and reflects the incident pulse. Therefore we call this solid density plasma-vacuum interface a plasma mirror.

A detailed description of the plasma gradient formation with the isothermal expansion model is given in [8, chapter 10]. The plasma can be described by the two fluid model leading to a slow expansion into vacuum at the ion sound speed, driven by the electron pressure. A self-similar solution for the plasma density is:

$$n(x) = n_c \exp\left(-\frac{x - x_c(t)}{v_s t}\right) \tag{7.1}$$

where n_c is the critical density, v_s the ion sound velocity and x_c the position of the critical surface. We see that the plasma gradient scale length $L_g = v_s t$ expands at a constant velocity, the ion sound speed. As this speed is proportional to the square root of the electron temperature (Equation (2.41)), it relates likewise to the pre-pulse fluence.

When now a p-polarized laser pulse propagates towards the plasma gradient at an oblique angle, the electric field will drive electrons to oscillate with a component normal to the target. When this happens along a gradient, these oscillations induce charge density fluctuations. When the local plasma frequency matches that of the laser, the plasma resonantly responds and plasma waves are excited.

The propagating wave will not actually reach this point. At oblique incidence angle, reflection already occurs where the local plasma frequency is $\omega_p = \omega \cos\theta$ and therefore at a density of $n = n_c \cos^2(\theta)$. Instead it is the evanescence field that tunnels behind this point and excites plasma waves at the critical density.

This mechanism is called resonance absorption and allows the transfer of energy from the laser into the plasma. It will become of interest again, as of course also the inverse is possible and plasma waves are converted to electromagnetic waves.

We also remark, however, that the notion of a wave propagating in the density gradient and being reflected only makes sense if the plasma gradient is sufficiently soft. In particular, the gradient scale length should not be much smaller than the laser wavelength. In fact there is an optimum plasma gradient for a given incidence angle and for an angle of, let's say, 55°this turns out to be $L_g \approx \lambda/7$ [74].

At steep plasma gradients, another absorption mechanism has been described by Brunel and is now called Brunel absorption or vacuum heating [75]. A large amount of energy can be absorbed by this mechanism when a laser interacts with a very steep density gradient. Electrons are periodically accelerated towards vacuum by the laser electric field. Once the laser field changes sign, together with the space charge created by the plasma, they are pulled back into the plasma. As soon as they cross the critical density they are shielded from the influence of the laser and their energy is lost to the plasma.

The density gradient needs to be shorter than the excursion length of the electrons in vacuum otherwise resonance absorption will become the main mechanism. Brunel absorption is responsible for most of the energy transfer at gradient scale length below 0.1λ and transitions to resonance absorption at longer gradients [73]. The exact transition varies with the laser intensity as this defines the electron excursion length.

7.2. High Harmonic Generation

High harmonic generation, seen in the spectral domain, is the result of attosecond pulses interfering spectrally to form the characteristic harmonic spectra. This is of great interest as the generation of attosecond pulses would allow novel techniques to resolve ultrafast processes in matter.

HHG has come a long way with the first observation in 1977 and quickly caught the attention of the scientific community [76]. In the first experiment Burnett *et al.* focused a CO_2 laser onto a solid target and observed harmonic emission up to the 11th order. Carman *et al.* reproduced this in the following years and achieved harmonic generation up to order 49 [77]. But these were all experiments with large nanosecond lasers, and with the advancement of femtosecond technology high harmonic generation was observed in gases starting in 1987 [78, 79, 80], and it was predicted that the harmonic spectra corresponds to coherently emitted attosecond pulses twice every cycle [81]. Without the necessary technology at the time, it was proposed that an absolute control of the CEP could lead to the generation of a single very short pulse [82], and its influence, without an actual control over it, was also demonstrated in principle in 1997 [83].

The first actual measurement of an attosecond pulse followed in 2001 and showed a pulse duration of 530 as [84]. HHG in gases became a very straightforward and versatile tool and new records for the shortest attosecond pulse quickly outperformed each other. Recently duration down to 53 as were measured [85, 86]

The advancements in femtosecond laser technology allowed this to be achieved at a high-repetition-rate using table top installations, leading to the first attosecond time-resolved measurements in atoms [87] and condensed matter[88]. These applications need a lot of statistics which makes it vital to operate at a high-repetition-rate. They typically run for many hours at a repetition rate of 1 kHz or more, equivalent to tens of million of laser shots. This makes it impractical and effectively impossible to perform these measurements on large-scale installation operating at much lower repetition rates (<10 Hz).

HHG on solids have been much harder to come by with the novel laser technology. Early nanosecond experiments were based on resonant absorption and consisted in generating harmonics by mixing plasma wave frequencies with laser frequencies. Harmonic generation on solids using femtosecond lasers rely on an entirely different mechanism. Starting in 1994 the theoretical groundwork was laid and a mechanism called relativistically oscillating mirror (ROM) was described [89, 90, 91], but it required unprecedented high laser intensities of more than $10^{18}\,\mathrm{W\,cm^{-2}}$. The first actual experiments with a table top femtosecond laser produced high harmonics up to order 15-17 were performed with laser intensities close to $10^{17}\,\mathrm{W\,cm^{-2}}$ [92, 93].

A revealing experiment came later, when a clear cut-off at the maximum plasma frequency was observed when irradiating a thin slab [94]. Eventually these results were explained by a mechanism called coherent wake emission (CWE) [95], which has a rather low conversion efficiency, but is already observable at much lower intensities. Both mechanisms will be described in detail below. Actually high harmonic radiation was also detected in transmission in [94], although the plasma should have been opaque to any light below the maximum plasma frequency, indicating that the radiation must have been generated inside the plasma gradient on the rear side of the target. This process is described theoretically in [96].

Solid high-harmonic generation (HHG) and its applications remain very challenging. As opposed to HHG in gases, relativistic-intensities pulse with high temporal contrast are required for efficient conversion. The solid target needs to be refreshed between each shot with high precision on the positioning accuracy. And without much surprise, the only ever temporal measurement of attosecond pulses from a solid target was done by Nomura *et al.* [97].

Nevertheless, in the future they might become an important tool again as we still need higher XUV flux and intensities to perform true attosecond pump-probe experiments. Gas as a generation medium is not ideal, as the emitted attosecond pulses do not exhibit a flat spectral phase, requiring additional optics inside the XUV path. But most importantly, HHG in gases do not scale easily to higher XUV intensities. Besides having a low efficiency, the generation process is intensity limited and breaks down above $10^{15}\,\mathrm{W\,cm^{-2}}$. At higher intensities the gas is ionized, which first leads to a depletion and poor phase matching and eventually completely prevents the generation mechanism. And this means in order to reach higher fluxes one needs much larger installation with a large laser focal spot.

Solid HHG on the other hand does not have this limitation. On the contrary, the conversion efficiency is predicted to increase with laser intensity until it reaches saturation. In fact very large conversion efficiencies have been predicted by using highly relativistic laser pulses ($a_0 > 10$) reaching even the few percent range for the bandwidth required to produce attosecond pulses (Figure 7.1) [98].

But so far relativistic HHG on solids have not been observed at a kHz, something

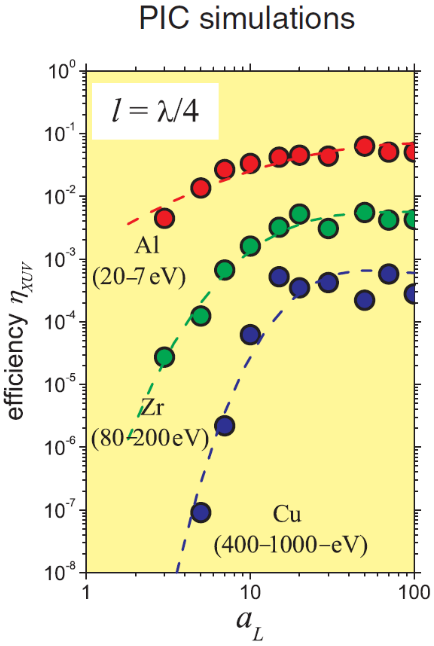

Figure 7.1. Attosecond pulse generation efficiency depending on filter and laser intensity. Reprinted from [98]

that seems essential for using them in a broad range of applications.

7.2.1. Generation Mechanisms

In this section I would like to introduce and compare the two known generation mechanisms and clearly show how the generated attosecond pulses differ from each other. The comparison was in part inspired by the excellent PhD tutorial written by C. Thaury and F. Quéré [99].

Relativistic Oscillating Mirror We start with the intuitively much easier to grasp ROM regime, which was also described first historically. To drive this regime the laser needs to have relativistic intensities.

A simple description goes like this. As depicted above, the incident laser is reflected off at the critical density, a mirror like surface, if you will. This surface is driven by the incident laser to oscillate at relativistic velocities. We therefore get a periodic Doppler shift of the reflected laser light. It periodically compresses and stretches the light field. New frequencies are generated, and when applying a spectral filter, this corresponds to a train of attosecond pulses, each of which is emitted at the periodic outwards movement of the reflection surface.

As intuitive as this sounds, this description is not entirely accurate and the attosecond pulses are rather created at the top of the relativistic electron jets accelerated outwards by the laser field at every cycle. 3D Particle-in-cell (PIC) simulations do describe the process properly but only at the cost of huge computing requirements. To account for the inconsistencies, Baeva *et al.* introduced the γ-spikes model as an analytical solution [91]. They showed that the spectral intensity should decay as $n_H^{-8/3}$, where n_H is the harmonic order. The spectral extent scales as γ^3, where γ is the Lorentz factor. This has been also reproduced in experiments [100]. In the end, we still rely on PIC simulations for accurate parametric studies.

The plasma scale length cannot be too steep as the electrons would not interact long enough with the pulse to reach relativistic velocities [101].The ROM regime therefore starts around a gradient of typically $\lambda/20$. Both experimentally and in 2D PIC simulations an optimum has been observed around $\lambda/10$ [102, 103].

The generation efficiency is highly nonlinear until it reached a saturation at highly relativistic intensities of $a_0 > 10$ [98]. It appears that there is no upper limit on the intensity, which should allow to easily scale the XUV intensity with novel laser technologies reaching ever higher intensities.

For moderately relativistic intensities, the attosecond pulses are generated with a close to 0 emission time, which does not depend on the intensity, meaning that the pulse train is very periodic [104]. This also means that the emitted beam has a flat spatial phase, as the emission time is the same at the periphery of incident beam, where the intensity is lower. This is no longer true for super relativistic intensities, as the radiation pressure dents the plasma surface [105].

The spectral phase of the individual attosecond pulses is very flat and we can assume a FTL pulse duration [98]. This makes them ideally suited for direct use in attosecond time resolved applications. The only temporal measurement of attosecond pulses generated on solid targets did not provide any phase information and the generation mechanism was most likely dominated by CWE [97]. Therefore, an experimental confirmation of FTL behaviour or any temporal information on ROM harmonics at all, remains elusive.

Coherent Wake Emission CWE is a completely different mechanism and happens already at low intensity starting somewhat around $10^{15}\,\mathrm{W\,cm^{-2}}$. It has a rather constant but low conversion efficiency that remains almost independent of laser intensity in simulations [106] and only shows a very weak intensity dependence in experiments [95]. It is therefore the dominant process for sub-relativistic laser intensities, where the laser field is not strong enough to accelerate electron jets to relativistic velocities.

CWE is deeply linked to Brunel Absorption and it is the energy absorbed through this mechanism that gets converted into high harmonic radiation. As we have already seen in the previous section, electrons are first pulled out and then accelerated back into the plasma. Once they cross the critical surface, the energy is contained inside the plasma. Electrons that travelled further outwards, will arrive at the critical density with a higher delay, but also a higher velocity and once they cross the critical density, they keep their speed. This means that the faster electrons will at some point overtake the slower ones. This is depicted in Figure 7.2.

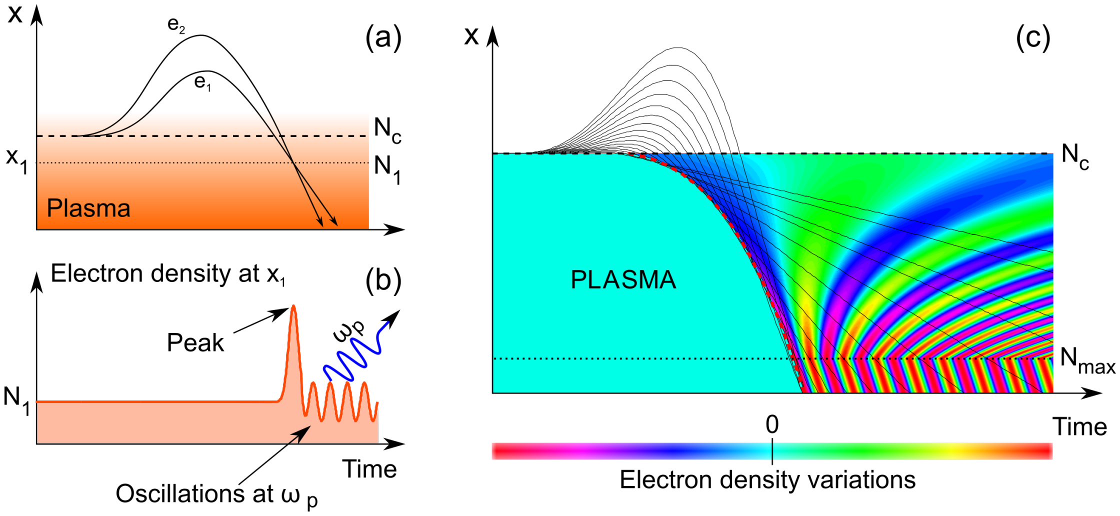

Figure 7.2. Principle of CWE mechanism. a) Trajectory crossing of electrons with different excursion depth and return velocity inside the plasma. b) Density peaks created by the trajectory crossings cause plasma oscillations that radiate in the inhomogeneous part of the plasma. c) Density peak travels along the red dashed line into the plasma. Reprinted from [107]

Where those trajectories cross, an electron density peak forms, which also travels into the plasma. In its wake, plasma oscillations are excited at the local plasma frequency and radiate light through linear mode conversion, or inverse resonance absorption, in the density gradient at the local plasma frequency. This crossing point moves inwards into the plasma with time.

There exists an optimal plasma gradient scale length with maximal harmonic emission. The conversion from electrostatic to electromagnetic waves is a linear mode conversion that happens only in an inhomogeneous plasma. Therefore no CWE harmonics can be generated for $L_g = 0$. Also at too long gradients the process breaks down. [99]. The optimal seems to be between $L_g = \lambda/100$ and $L_g = \lambda/50$.

As the generation happens inside the gradient, this makes the emission spectrum highly dependent on the plasma conditions. First, no frequencies above the maximum plasma frequency can be generated. Therefore, observing high harmonic orders above this threshold is a clear indication that they cannot have been generated by the CWE mechanism. For our experiments with fused silica targets, the maximum plasma frequency is around harmonic order 20 with an 800nm laser. Also the density gradient shape is important. As the different frequencies are generated at different times and different depths along the gradient, this defines how they interfere to eventually form the attosecond pulses. In fact the crossing points follow approximately a quadratic function in time. We call this the emission time for each harmonic number. These waves interfere constructively to form the attosecond pulses and their individual emission time defines the spectral phase. This creates a chirp to the attosecond pulses, which temporally stretches them, in contrast to the ROM regime.

The emission time depends on the gradient scale length as well as on the driving laser intensity [104]. With a higher laser intensity, the Brunel electrons return quicker and with a higher velocity to the plasma and therefore the harmonic wavelengths are emitted earlier. On the other hand, as they are created inside the gradient, it makes sense that the shape has an influence. The longer the gradient, the later the pulse is emitted. And actually the longer the gradient, the stronger the dependence on the intensity. This is all expressed in the emission time t_c [108]:

$$\frac{t_c}{T_L} = 0.307 + 0.725 \left(\frac{x_\omega}{a_0 \lambda_L \sin(\theta)} \right)^{1/3} \tag{7.2}$$

where T_L is the laser period, λ_L the laser wavelength, θ the incidence angle and x_ω the depth at which the harmonic frequency ω is created. For an exponential plasma shape, x_ω is proportional to the gradient scale length L_g and we absorb fixed parameters to a constant:

$$\frac{t_c}{T_L} = 0.307 + 0.725 \left(\frac{L_g}{a_0} \right)^{1/3} \cdot \text{const.} \tag{7.3}$$

Not only each attosecond pulse possesses a chirp, but also each pulse within the train has a varying relative delay to the fundamental carrier wave. This leads to a certain non-periodicity of the attosecond pulse train, also called the femtosecond chirp. In fact the emission time of the attosecond pulse as a whole depends just the same on the gradient scale length and intensity.

During an interaction of a relative short laser pulse ($\lesssim 50\,\text{fs}$), the plasma gradient does not evolve much and the main effect stems from the change in intensity due to laser pulse envelope. At higher intensities the delay is shorter. The delay between two consecutive pulses is proportional to the derivative of Equation (7.3). Assuming a Gaussian envelope for a_0, the first derivative of Equation (7.3) becomes a monotonically increasing function. The delay between consecutive pulses in the train therefore continuously increases throughout the pulse. This effect is stronger for shorter driving pulses.

Normally, the spectral width of the individual harmonics correlates to the duration of the pulse train. If we see the harmonic spectrum as the results of interferences of the individual attosecond pulses of the pulse train, the non-periodicity causes a broadening of the harmonics. When positively chirping the driving laser, the different emission time can be compensated and narrow harmonics can be obtained [109]. For negative chirp, just the opposite happens and the apparent spectral broadening gets stronger. All these effects are clear indications for the CWE regime.

The same is true for the spatial phase. For a Gaussian spatial beam profile the intensity is higher in the centre. The XUV beam will therefore be emitted with a defocusing spherical phase, which increases its divergence. ROM harmonics, on the other hand, are normally emitted with a flat phase or with an opposing phase for very high laser intensities. This has also been confirmed in an experimental measurement using ptychography [110].

Transition The transition between both regimes has been observed experimentally. In increasing the intensity from the sub-relativistic to a relativistic regime, harmonics above the maximal plasma frequency appear [111, 112]. In another experiment the transition was observed at a fixed intensity with increasing the plasma scale length [102]. In the ROM regime the harmonics showed a lower divergence and frequencies above the plasma cut-off. We will see other distinctive transition features in the chapter devoted to experimental results.

7.2.2. Single Attosecond Pulse Generation

The ultimate goal is to produce single attosecond pulses. Only single attosecond pulses can provide a univocal timestamp to pump-probe experiments resolving ultrafast processes. Over the years, many techniques evolved to achieve this goal. One needs to either only generate a single attosecond pulse or to isolate a single pulse from the pulse train.

To generate an isolated attosecond pulse, the harmonic generation process needs to be temporally gated such that it only occurs efficiently during one laser cycle. Short of using a single-cycle waveform controlled driving laser pulse, more elaborate schemes have been suggested and demonstrated in the case of gas harmonics, such as amplitude gating and spectral filtering [98], time dependent polarization gating [113], ionization gating [114].

The attosecond lighthouse is a recently proposed [115] and validated [72] scheme to generate single attosecond pulses in the CWE regime by separating the pulse train. It was developed to spatially gate single attosecond out of a linear generation process and few-cycle driving pulses. Even with near single-cycle duration (FWHM) in intensity, efficient generation is possible over multiple field oscillations leading to an attosecond train. The attosecond lighthouse applies a wavefront rotation in focus on the driving laser, which emits each attosecond pulse in a different spatial direction.

Assuming, however, we have a relativistic near single cycle pulse, it could be directly used in the ROM regime to compress the incident field into a single attosecond pulse.

8. Experimental Setup

The current experimental setup builds on a long history and expertise under the leadership of Rodrigo Lopez-Martens involving the work of three PhDs dedicated to SHHG. Antonin Borot and colleagues started in 2007 to set up the experimental chamber and to perform the first experiments with 25 fs and 5 fs pulses in the CWE regime. They conceived a high-repetition-rate solid target [116, 26] and an extreme ultraviolet (10 nm - 124 nm) (XUV) spectrometer. With this setup, they were able to perform the first HHG experiments from a kHz solid target with 1 mJ, 25 fs pulses [30] paved the way for HHG using high-repetition-rate lasers. They went on to demonstrate the coherent control of electron motion in plasmas with attosecond precision, by looking at the CWE signal as a function of CEP for few-cycle driving pulses [109].

Together with John Wheeler, who joined as a postdoc, they performed the first attosecond lighthouse experiments to generate a continuous spectrum (an indication for a single attosecond pulse) in the CWE regime [72].

Under the lead of the next PhD student, Maimouna Bocoum, who started in 2012, large improvements were made to the experimental setup, including an improved XUV spectrometer (larger collection angle and bigger spectral range), new diagnostics for the detection of fast electrons and a time-delayed prepulse for controlling the plasma scale length. The double CPA described in Chapter 4 enabled the study of the CWE regime with a higher intensities and better control of the plasma gradient scale using 24 fs pulses. In particular, we developed a new technique to characterize the plasma density gradient. [117]. This, in turn, enabled us to observe the anti-correlated emission of CWE harmonics and fast electrons (energy up to 0.5 MeV) [118]. This effect was also confirmed by PIC simulations that also showed, that the emission of fast electrons should, on the contrary, correlate with the emission of ROM harmonics at higher intensities.

After building the HCF post-compression setup and the few-cycle vacuum beamline I took over the SHHG experiments in order to explore the relativistic regime using near-single-cycle pulses for the very first time. With better control over the pre-pulse together with more diagnostics for a proper overlap this allowed finally to precisely control the plasma gradient. And the vacuum beamline gave more defined and stable experimental conditions. Thanks to this, we finally achieved the multi-parameter optimization to generate relativistic SHHG. We could then continue to explore the near single-cycle regime to generate continuous spectra at a proper CEP of the driving laser.

In Figure 8.1 we can see the conceptual layout of the target and diagnostics. The main pulse is focused together with the pre-pulse on a rotating fused silica substrate at an angle of incidence typically between 45° and 60°. During all my experiments the angle of incidence was fixed at 55°. As a target substrate we use fused silica as it is easily available with a high surface quality and leads to very little pollution of the vacuum chamber during use. Fused silica has an electron density of around $6.6 \cdot 10^{23}\,\mathrm{cm}^{-3}$ or $\sim 400 \cdot n_c$ for 800 nm. The maximum plasma frequency is at 30.2 eV and corresponds to harmonic order 19.5 for an 800 nm central wavelength driving laser.

In the specular direction, we installed an XUV imaging spectrograph that resolves the vertical divergence and spectrum. This can be replaced by a spatial XUV detector to get the full XUV beam profile. Additionally we have a spatial electron detector positioned between the target specular and normal directions. In principle, this can be also replaced by an electron spectrometer, but unfortunately, we did not have time to use it during my experimental runs.

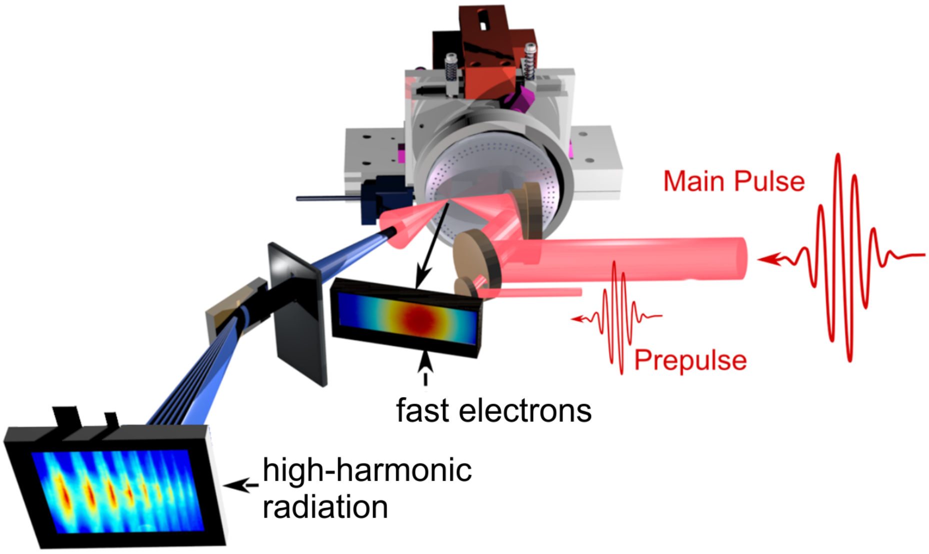

Figure 8.1. Conceptual optical layout for SHHG experiments with simultaneous detection for fast electrons (spatial) and high harmonic radiation (spectro-spatial). Reprinted from [119]

8.1. High-Repetition-Rate Solid Target

Ensuring reproducible laser-plasma interaction conditions from shot to shot at 1 kHz is not an easy task. After each shot, the target surface is destroyed and must therefore be quickly moved in order to refresh the interaction area, which is challenging to accurately achieve at 1 kHz. With a typical Rayleigh range of equal or less than 5 μm, standard rotational motion devices cannot provide the precision required to keep the target in focus. Back in 2008 Borot *et al.* started developing a high-repetition-rate solid target positioning device [26, 116], which a few years later, enabled observation of SHHG at 1 kHz for the first time [30].

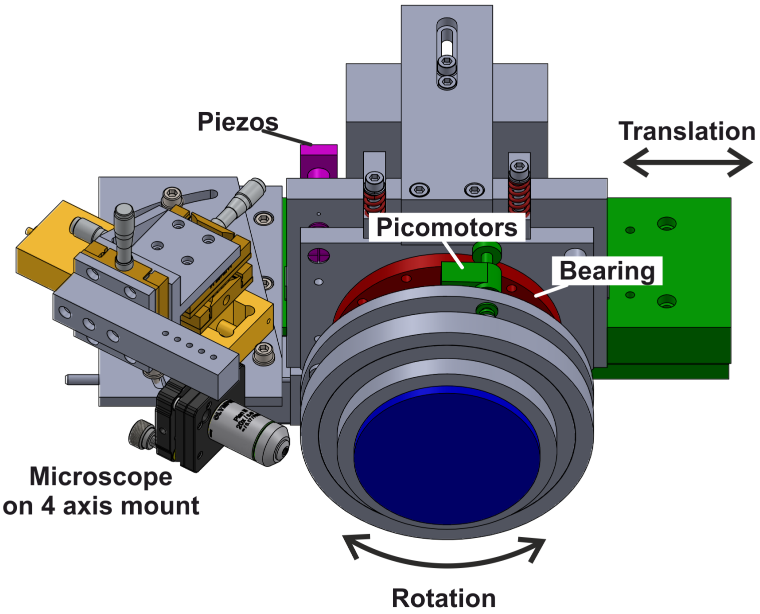

Figure 8.2. Current implementation of kHz solid target. Substrate shown in blue, bearing in red.

The current version of the target is shown in Figure 8.2. A high quality, optically polished and flat fused silica substrate is mounted on a large rotating bearing. The rotation is controlled by a server motor, such that the speed and position can be precisely controlled. This whole assembly is mounted on a motorized translation stage that moves parallel to the substrate surface. By synchronously rotating and translating the target, the laser will form a spiral like shot pattern on the target surface. The rotational speed needs to be adjusted, such that impact craters do not overlap. Typical images of the impact craters are shown in Figure 8.3 under different plasma gradient conditions. Actually the size of the resulting impact crater depends not only on the pulse energy but also strongly on the density gradient created by the pre-pulse. A soft plasma gradient that extends deep into vacuum ($L_g \gtrsim \lambda$) will reflect the main-pulse with limited damage to the surface (Figure 8.3 a). We can see the shape of the pre-pulse that ablated the target and a small dot in the centre corresponding to the main pulse. On the other hand the interaction with steep plasma gradients will lead to shock wave formation resulting in large and deep impact craters (Figure 8.3 b). In this last case, we see that the 150 μm spacing between shots was almost insufficient and impacts crates start to overlap.

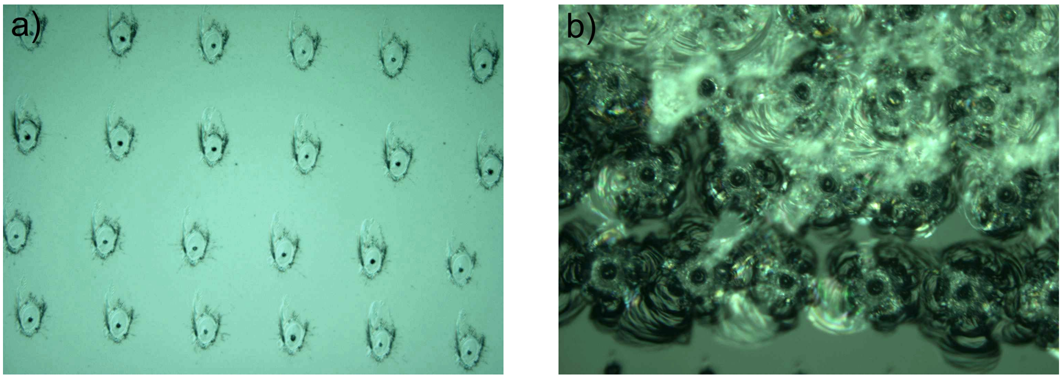

Figure 8.3. Impact craters on target surface for soft (a) and steep (b) plasma gradients at otherwise identical laser parameters. Shot spacing of around 150 μm. Photographed with a microscope in transmission mode. The magnification was the same for both images.

At the side of the target we installed a microscope objective to image the laser focus onto a CCD camera with a magnification of around 80. This can be moved into the beam pass by translating the whole target assembly. The objective itself is mounted on a four axes positioner. The first rotation stage aligns the optical axis and the three translation stages with the laser beam axis and can be adjusted from 40° to 60° target incidence angle. The other three translation axes can then move the objective in and out of focus as well as sideways.

For the target plane to stay in focus it needs to be well aligned normal to the axis of rotation. This can be adjusted by the picomotors between the bearing and the target disc. In order to diagnose the stability of the target surface, one arm of a Mach-Zehnder interferometer, driven by a frequency stabilized HeNe laser, is reflected off the target and the other arm off a fixed mirror. After beam-recombination on a CCD camera, the interference pattern enables precise reconstruction of the relative movement of the target surface over time[26]. By monitoring the stability over one rotation, the pico-motors can be used to iteratively align the target. With this method a passive stability of the target surface of around 400 nm RMS in depth and around 25 μrad RMS in orientation can be achieved.

This is mainly limited by the bearing itself. The stability is sufficient to drive SHHG experiments in reproducible conditions at 1 kHz.

Operation at 1 kHz, means that the target surface is quickly used up. During experiments we used target substrates with a diameter of 10 cm. This only provides enough space for 350,000 shots or actually only around 5 min of continuous operation. We used a fast mechanical shutter for our measurements to operate in burst mode, where each data point was usually the average of 100 consecutive shots (100 ms continuous operation). Target rotation, shutter and all diagnostic devices were accurately triggered and timed using a micro-controller device. I included the possibility to perform automated parametric scans, for example varying the delay between pre- and main-pulse to control the plasma gradient (gradient scans). In addition, the parameter over which the scan was made, could be randomized to avoid any systematic bias (laser drift or mechanical drift of the target positioner).

8.2. XUV Detection

In order to observe the transition of CWE to ROM regimes, we were particularly interested in being able to detect harmonic frequencies around the maximum plasma frequency (ω_p) (30 eV photon energy for a fused silica target). This way we get an intense signal from the lower harmonics and can distinguish relativistic HHG with spectral components above the maximum plasma frequency with the XUV spectrometer. The detection range was therefore chosen from 100 nm down to around 25nm (photon energies from 12 eV to 50 eV).

For XUV photon detection we use a large, single stack micro-channel plate (MCP) together with a phosphor screen from PHOTONIS. The phosphor screen (P46 with a fast decay time of 300 ns) is then imaged by a high sensitivity CCD camera. Unfortunately our desired wavelength range is not easy to cover with a flat spectral response. We see the MCP wavelength dependent efficiency in Figure 8.4 and note a rather poor response in our range of interest. At the same time it has a rather high efficiency in the lower wavelength beyond our range of interest. We will see later that this becomes problematic when higher diffraction orders from the spectrometer grating overlap with our range of interest.

Ideally, the response in the range of interest could be boosted. A possible coating option from PHOTONIS (MgF_2) does boost the efficiency in the middle of the range, but also falls slightly towards the maximum plasma frequency. A wavelength that is of particular interest to discern the ROM from the CWE regime. The coating has also higher demands on the handling of the MCP, which should not be exposed to ambient humidity. Experimentally, this is not ideal, since the vacuum chamber needs to be frequently opened for changes in setup. Nevertheless, this option should be considered for future experiments.

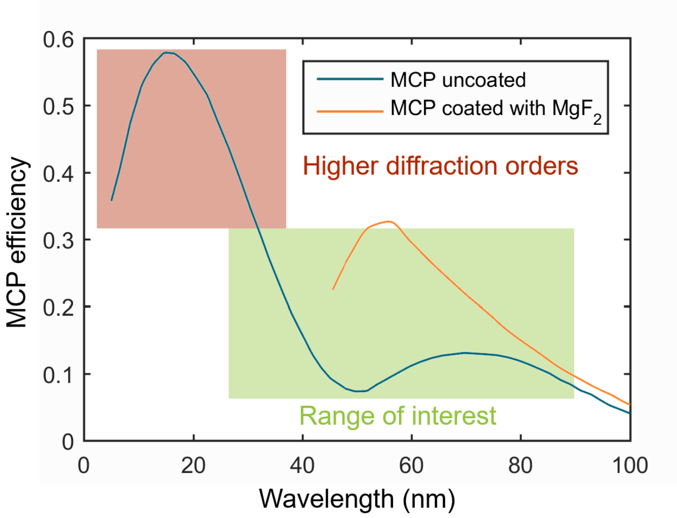

Figure 8.4. Uncoated (blue line) and MgF$_2$ coated (orange line) MCP detection efficiency in dependence of incident photon wavelength. Data from Photonis commercial presentation.

8.2.1. XUV Spectrograph

For the XUV spectrometer, we use a spherical grating at grazing incidence in the specular direction from the target. It is an aberration-corrected flat-field grating from Hitachi (001-0639). The diffraction is along the horizontal plane. Due to the strong astigmatism from the grazing incidence, the beam is only refocused in the plane of diffraction and the beam divergence information is kept in the vertical plane. Ambient light is shielded with rectangular apertures either side of the grating.

The diffraction efficiency is increased by blazing the grooves towards the direction of diffraction for the wavelengths of interest. We can see the grating response in Figure 8.5a. By the nature of a blazed grating, the reflectivity is also enhanced for higher diffraction orders at a fraction of the fundamental optimized wavelength. In fact, the higher diffraction orders are optimized towards the same direction as the first order. And we note in Figure 8.5a that the reflectivity drops only by 40% from the first to the fourth order. Taking also the MCP response into account, which has a much higher efficiency at lower wavelength, we get an overall response that is totally dominated by higher diffraction orders in the wavelengths range of interest. This can create a rather large background due to incoherent plasma emission. With a strong harmonic signal this is not such a problem, but does cause trouble to detect in particular the transition from CWE to the ROM regime. A coated MCP would certainly also help here.

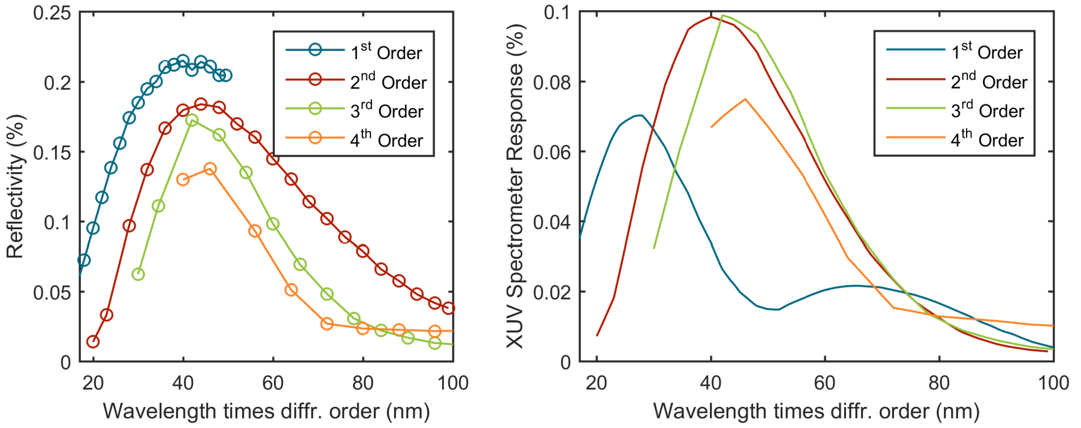

(a) Hitachi Grating Efficiency. Data provided from measurement at Lawrence Berkeley National Laboratory.

(b) Overall Spectrometer Response. First order diffraction efficiency for the grating extrapolated to longer wavelength using the shape of second order diffraction efficiency.

Figure 8.5. XUV spectrometer response.

This strong higher order diffraction also caused difficulty in the spectral calibration. Usually plasma emission lines can be easily used for accurate wavelength calibration. To do this, the pre-pulse is send onto the target long before the main pulse arrives. All the harmonic emission is then suppressed and only strong plasma emission lines can be observed. On the other hand, the electron temperature and density needs to be known in order to estimate the relative strength of the atomic line emission. Without taking into account the higher order diffraction, it was impossible to find a reasonable electron temperature matching the recorded spectra.

This comes as no surprise looking at the data in Figure 8.6, where we recorded the plasma emission using a thin aluminium filter (100 nm) to block wavelength below 17 nm. Without this, even more high-order emission lines were visible. We then took theoretical atomic line spectra and adjusted the electron temperature to match the recorded spectrum by taking into account the full spectrometer response and all higher order diffractions that fall onto the MCP. With an electron temperature of around 80 eV we got a very good match to almost all emission lines and excellent overlap of the zero points. We note, that basically only higher order diffraction lines are visible.

After proper wavelength and divergence calibration we see an example spectrograph in Figure 8.7. We resolve the vertical divergence from around ±30 mrad.

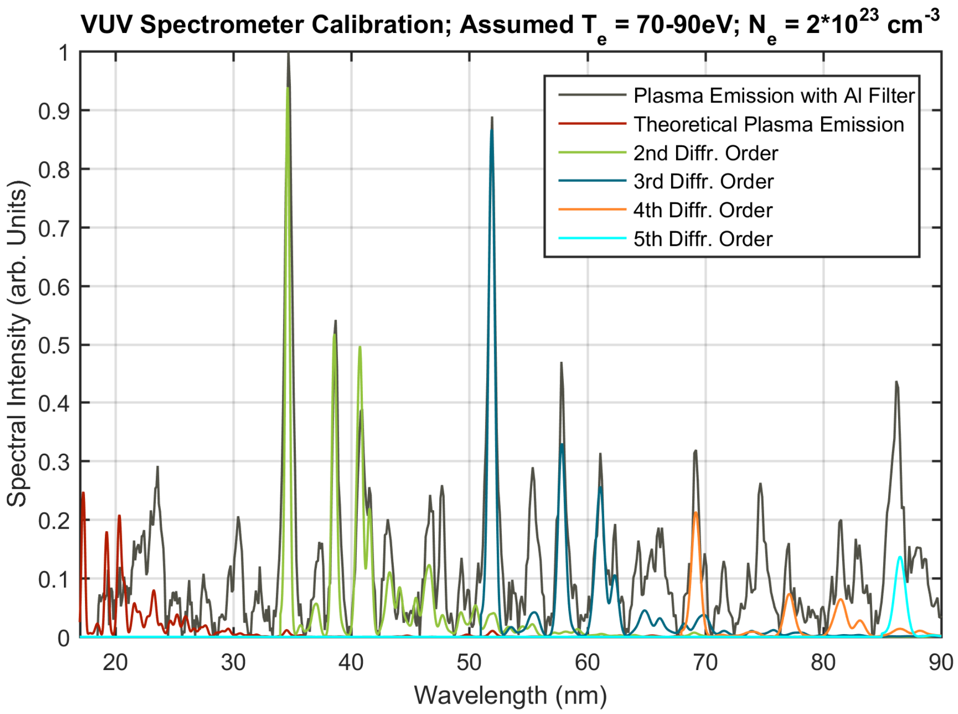

Figure 8.6. Observed plasma emission lines with Al-filter inserted before the XUV-spectrometer and comparison to theoretical plasma emission lines from Si and O ions with an electron temperature around 80 eV. NIST Atomic Spectra Database: https://physics.nist.gov/PhysRefData/ASD/lines_form.html

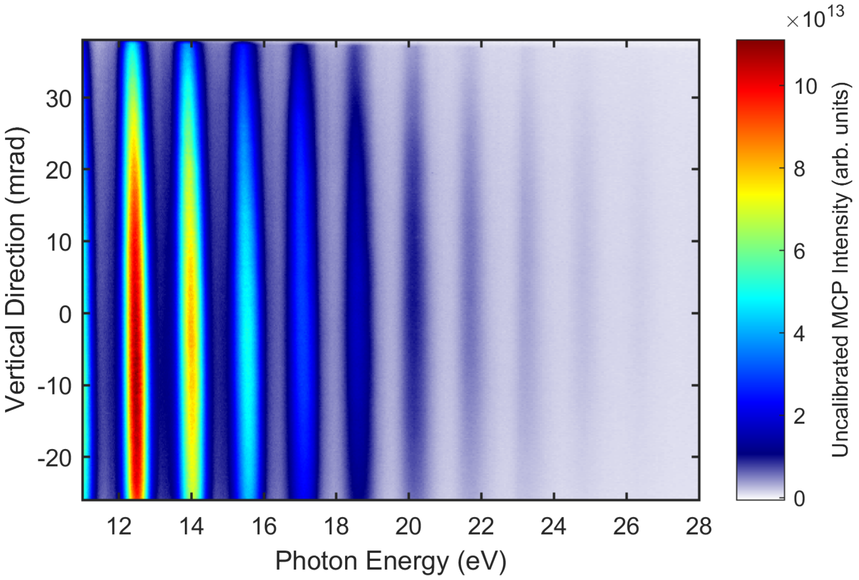

Figure 8.7. Example spectrogram recorded with high harmonic emission from the solid target. The divergence and wavelength are calibrated, while the intensity is shown in raw MCP emission intensity.

8.2.2. Spatial XUV-Beam Measurement

For the spatial XUV beam measurement, we installed a MCP together with an imaging CCD camera on a translation stage, so it could be shifted into the specular beam just in front of the XUV spectrometer. This way, we could obtain both a spectral and spatial measurement with rather similar conditions, in particular without opening the chamber.

This measurement turned out to be much more difficult than initially thought. We had a large background coming probably from rather low energy electrons. Moreover, a single stack MCP is not opaque to visible light and therefore the incoherent plasma emission was producing an additional background. Finally, the phosphor emits in the green and therefore an interferometric filter in front of the camera shields to some extent the signal from ambient light. When shooting with the shortest pulses, however, the laser spectrum overlapped with the phosphor emission and the light transmitted through the MCP completely saturated the camera.

The solution consisted mainly in installing strong magnets in front of the MCP to deviate the electrons and pulsing the MCP with a sharp falling edge HV pulse in order to cut out the much longer plasma emission from the target. In addition, the voltage between the MCP stack and the phosphor screen was increased to better differentiate between ambient and actual signal light. An aluminium filter was also used, but since it only starts to transmit from harmonic number 10 onwards, the strong lower order harmonics were blocked (the MCP starts to detect from harmonic number 6) and only an extremely weak signal reached the detector. Nevertheless, this was the only working solution when using the shortest laser pulses.

For the future a better setup needs to be developed, possibly with some kind of optic that only reflects the XUV towards a detector. For example with grazing incidence AR coated fused silica plates.

8.3. High Energy Electron Detection

In order to spatially detect fast electrons emitted from the interaction, we installed a Lanex screen between target normal and specular directions, while leaving enough space to simultaneously use the XUV spectrometer. The screen was imaged by a CCD camera. The varying distance from the laser-plasma interaction to the detection point on the Lanex screen was taken into account by using spherical coordinate transformation. This enabled a proper rendering of the emitted electron signal.

The Lanex screen consists of a scintillator material (Gd_2O_2S:Tb) deposited on a flexible polymer substrate. It emits in the yellow-green around 545 nm. They can be produced in large size, ideal for covering the whole emission around the target. Lanex screens are typically used for medical applications, but have also been extensively tested for scientific electron detection [120, 121]

The front side of the Lanex screen (facing target) is covered by a $\sim 13\,\mu$m thick aluminium foil to block the visible light and lower energy electrons below ~ 200 keV.

For proper measurement of the total detected charge, the whole imaging system was calibrated at the Photo-Injector facility at Laboratoire de l'Accélérateur Linéaire, a linear electron accelerator. The electrons had an energy of about 3.7 MeV and the electron bunch charge was calibrated with an integrating current transformer (ICT).

Unfortunately, the theoretical response does not remain flat for electron energies below 2 MeV, where the signal increases three fold (Figure 8.8). Therefore, there remains an uncertainty in the measured electron charge as function of their energy.

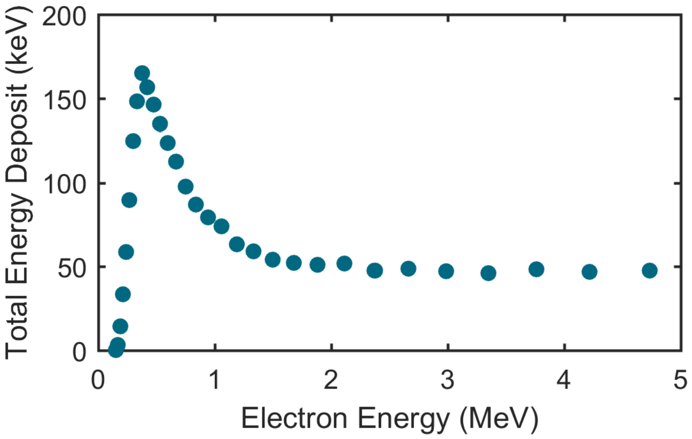

Figure 8.8. Lanex response versus electron energy. The response is proportional to the total deposited energy. Data from [120]

8.4. Plasma Gradient Measurement

As seen in the previous section, the SHHG mechanism strongly depends on the plasma gradient scale length. It is therefore important to control and measure it accurately.

The established measurement method is frequency domain interferometry (FDI) [122], which resolves the plasma expansion very accurately but is also fairly complex to implement experimentally. During normal experiments, a short pre-pulse ($< 100\,\text{fs}$) creates the plasma that then expands with constant velocity into vacuum. The FDI technique works by sending a probe beam, consisting of a much shorter reference pulse and a replica, onto the plasma. The reference pulse arrives shortly before the plasma is created. The replica arrives at defined time, thereby experiencing a face shift upon reflection off the expanding plasma surface. By spectrally resolving the interferences between the reference and replica, this phase shift, and therefore the plasma gradient scale length, can be retrieved.

We developed an in-situ technique, called spatial domain interferometry (SDI) [117], which is extremely simple to implement and does not need any additional hardware except a spatial mask and a camera. The setup is shown in Figure 8.9. A honey comb mask is introduced in the main beam, thereby creating a diffraction pattern in focus on target. The mask pattern is then reproduced on the near-field beam profile of the main beam reflected off the target and can be imaged on a simple screen recorded by a camera. The pre-pulse only overlaps with the centre part of the main beam diffraction pattern on target. Only the central diffraction spot therefore experience a phase-shift relative to the plasma expands. Once the delay between pre-pulse and probe is large enough and the induced phase-shift

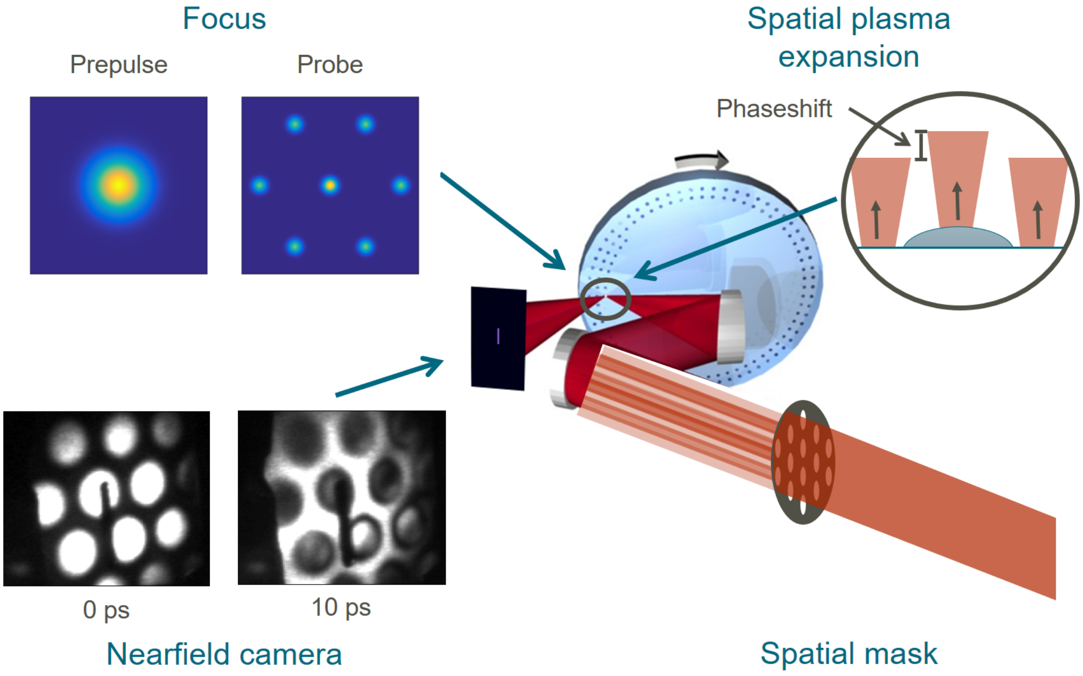

Figure 8.9. Implementation of the SDI measurement principle in our setup. A spatial mask is inserted into the main laser beam. The XUV-spectrometer slit acts as a screen for the nearfield that is imaged by a camera.

reaches a value of π, the pattern imaged on the screen will invert. For a 2π phase-shift, the original pattern emerges again. This continues until the coherence length of the probe beam is reached. As the plasma expansion velocity speed is constant, it can therefore be retrieved by measuring the delay between subsequent inversions.

An actual measurement is shown in Figure 8.10 where the plasma expansion speed is estimated to be $10.8\,\mathrm{nm\,ps^{-1}}$ for a pre-pulse fluence of $14.5\,\mathrm{J\,cm^{-2}}$. This value agrees well with FDI measurements under similar conditions.

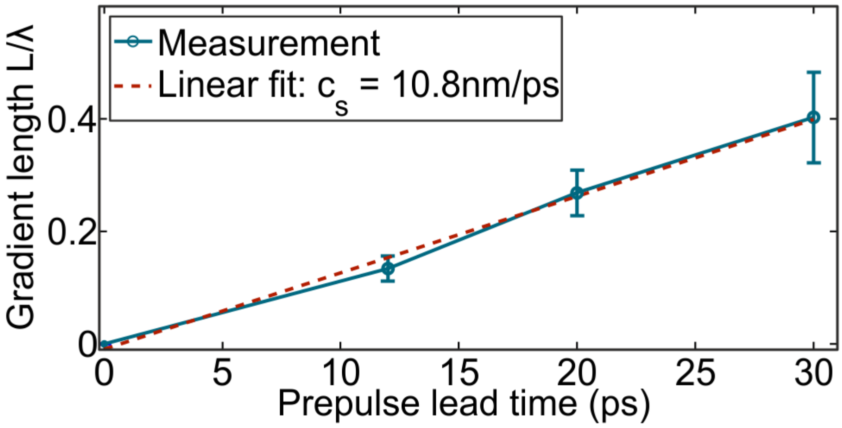

Figure 8.10. Measured plasma expansion velocity and retrieved gradient scale length using the SDI technique. Reprinted from [117]

Even though this setup is experimentally very simple, we did not make a measurement during each experimental run. The electron temperature depends linearly on the deposited energy from the pre-pulse. Therefore the expansion velocity should scale to the square root of the pre-pulse fluence $c_S \propto \sqrt{H_e}$. Assuming an unchanged beam profile, the expansion velocity can be therefore easily extrapolated just by measuring the pre-pulse energy before each run. For this we take:

$$c_S = 1.9 \cdot \sqrt{E_p}\,\frac{\mathrm{nm}}{\mathrm{ps}\cdot\mu\mathrm{J}^{\frac{1}{2}}} \tag{8.1}$$

A typical pre-pulse energy of $100\,\mu\mathrm{J}$ yields an expansion velocity of $c_p = 19\,\frac{\mathrm{nm}}{\mathrm{ps}}$. As the plasma expansion does not depend on the intensity, we expect consistent results for different pulse durations coming out of the HCF.

8.5. Optimizing Focal Position

Here I shortly introduce a reliable method to quickly find a rough estimate of the optimal focus plane on target. As the CWE mechanism behaves rather linear with intensity, being out of focus does not necessarily decrease the signal. The typical approach to find the focus plane by optimizing the harmonic signal, therefore, fails.

For this we introduce a double-hole mask into the driving laser beam. The two holes are placed either side of the beam profile to create two distinct beam that will overlap at focus. When moving away from the focus, the two beams do not overlap and each one will create an XUV beam in their respective direction. Only in focus do the two beams overlap and generate an XUV beam on the optical axis. By optimizing this signal in the centre of the spatial detector, the position of focal plane can be estimated with a precision comparable to the Rayleigh range. A measurement is shown in Figure 8.11.

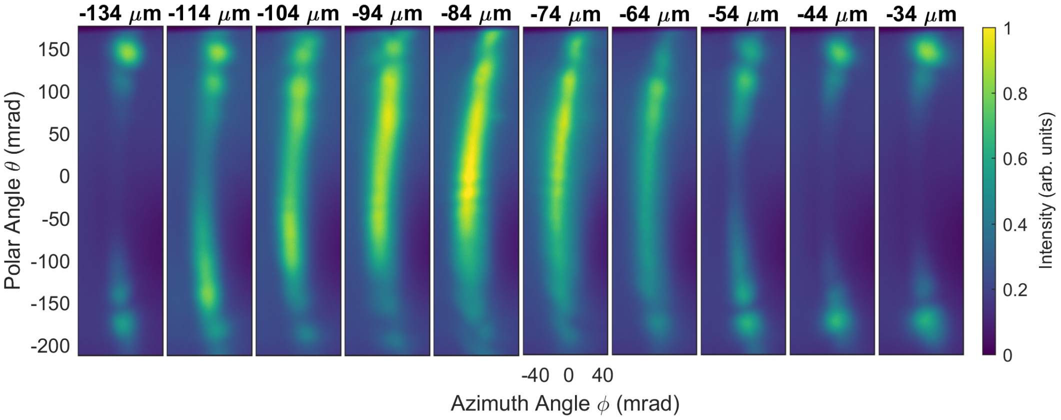

Figure 8.11. Spatial image of CWE beam generated using a double-hole aperture in the main laser beam (without pre-pulse). Only in focus (around parabola position $-84\,\mu$m) does SHHG take place on axis.

9. Experimental Results

After finishing with the HCF post-compression setup and vacuum beamline, we had roughly half a year to realign and perform the first experiments on the solid target with the upgraded laser chain. This chapter details the first results in a regime completely new to us. We had a laser peak intensity at focus around one order of magnitude higher than in previous experiments using few-cycle pulses by Borot [123]. And almost an order of magnitude shorter pulse duration than for similar pulse energies [119], as well as a precisely controlled plasma scale length.

9.1. Transition from CWE to ROM regime

The first set of experiments were devoted to demonstrate ROM generation by varying the plasma scale length and corroborating results with predictions and previous experiments.

Gradient influence As seen in Section 7.2.1, the emission time in the CWE regime depends on the plasma gradient as well as on the intensity. Assuming a well compressed driving laser pulse, the emission time dependence on the intensity leads to an aperiodic pulse train and broader harmonic peaks in the spectral domain, which is not the case for ROM harmonics. We have also saw that steep gradients favour CWE, whereas ROM harmonics appear at longer gradients. We started by performing gradient scans to see the transition from CWE to ROM, as reported previous studies [102].

The driving laser pulse duration was chosen to be 24 fs. This duration seemed ideal for observing the thinning out of individual harmonic peaks with increasing plasma gradient scale. It is also long enough, to confer a deeply modulated structure to the CWE spectrum, yet short enough, that the cycle to cycle variation in emission time, still plays an important role. The laser peak intensity was estimated to be $0.23 \cdot 10^{19}\,\mathrm{W\,cm^{-2}}$ ($a_0 = 1$). At this intensity, both generation mechanism should be equally dominant.

Figure 9.1 shows a gradient scan for a pre-pulse lead time ranging from 0 ps to 7 ps. From the SDI measurement, this translates in a change of plasma gradient scale length from 0 to $\lambda/7$, where λ is 800 nm. In all figure the gradient scale length deduced from the SDI measurement is shown: $L_{SDI} = L_g - L_0$, where L_g

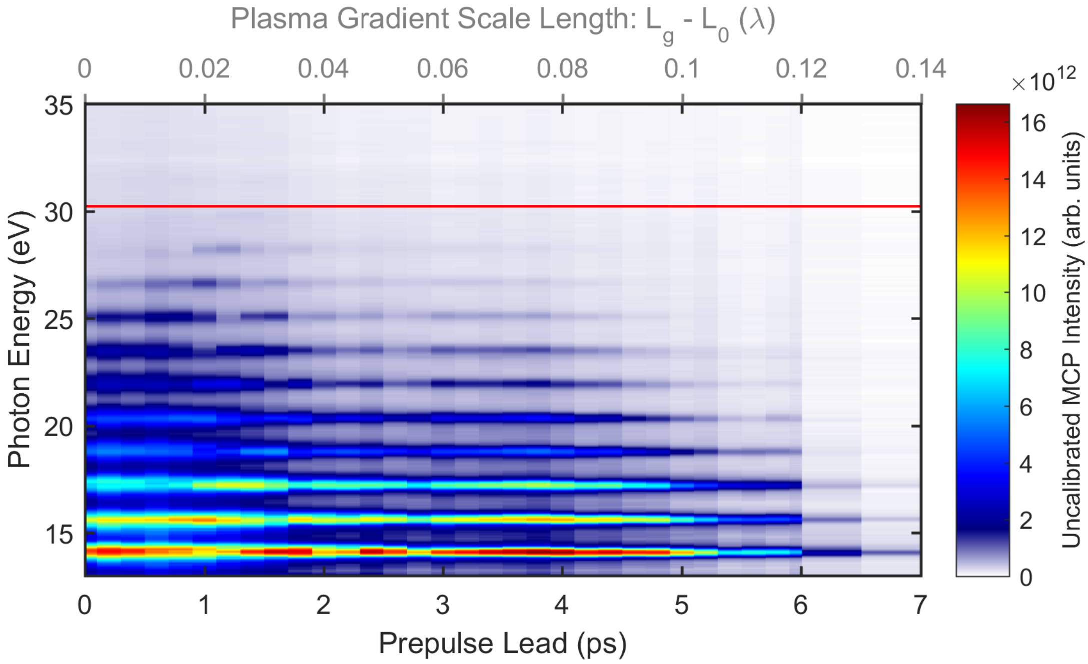

Figure 9.1. Angularly integrated harmonic spectra for different plasma gradient length (gradient scan) created by a varying pre-pulse lead time. Harmonics were generated with a 24 fs driving pulses and a peak intensity of $a_0 = 1$, recorded over a sequence length of 100 ms. The red line denotes maximum plasma frequency. Background subtracted using data acquired at larger pre-pulse lead time, where the harmonic signal disappears.

is the actual plasma gradient scale length and L_0 the contribution from the rising edge of the main pulse (or in general the contrast of the laser), which cannot be measured with the SDI technique. For simplification we neglect L_0 for our gradient scale lengths of interest, justifies by the fact that we did observe CWE harmonics.

We can start to distinguish a thinning out of the harmonics at a gradient of 0.025λ ($\lambda/40$). A maximum generation efficiency seems to occur for the presumed ROM regime between 0.04λ ($\lambda/25$) and 0.1λ ($\lambda/10$). The fact that we observe CWE harmonics, also validates the laser contrast to some point, although we do not see an optimal or a drop towards 0 or negative pre-pulse lead time. This indicates that we do in fact pre-ionize the target by the pedestals of the main-pulse. According to theory the gradient created by only the main pulse has to be at least $\sim \lambda/150$. Nevertheless, it still justifies, to use the SDI measurement directly without a constant offset in the figures.

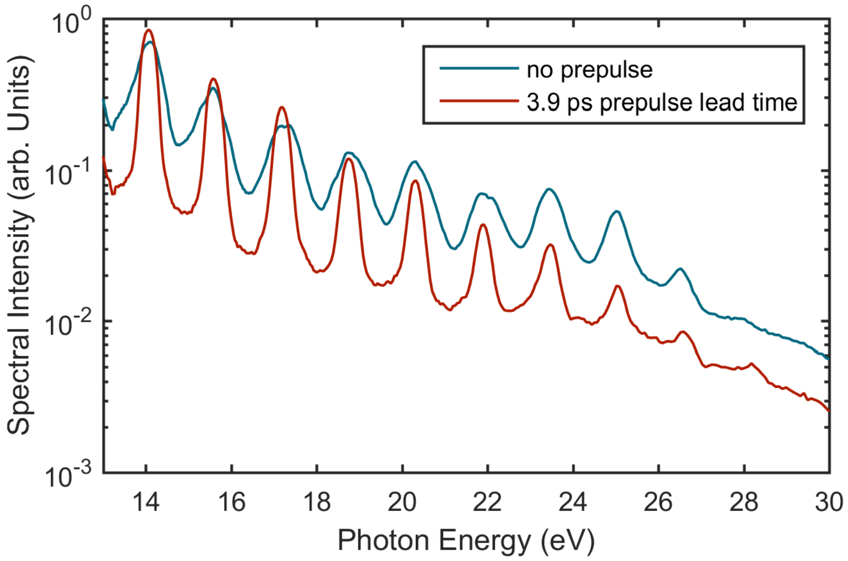

Figure 9.2. Angularly integrated and calibrated harmonic spectra with a 24 fs and $a_0 = 1$ driving pulse for the steepest plasma gradient $\sim \lambda/150$ (blue line) and gradient of $\lambda/13$ (red line). Sequence length of acquisition: 100 ms.

Figure 9.2 compares harmonic spectra recorded at the steepest gradient ($\sim \lambda/150$) and softer gradient of $\lambda/13$. The thinning out of the harmonic peaks now becomes obvious. We also remark, that no harmonics are visible above the maximum plasma frequency (above 30 eV) for softer gradients. This is not very surprising, as the laser intensity was only just around the relativistic threshold. As we have previously seen (Chapter 7), the harmonic order beyond which the spectrum cuts-off, scales as $n_{cutoff} = \sqrt{8}\gamma^3$. Which under our conditions yields a cut-off harmonic number of only about 5.

Intensity influence Another important and distinctive influence is the laser intensity. Whereas the CWE regime exhibits close to linear dependence on laser intensity, the ROM regime is highly nonlinear (at intensities below the saturation level, anyway). To test this, we inserted a 22.5 mm aperture inside the laser beam, which reduced the energy by 50%. At the same time the focal spot size increased by a factor of 1.3 this lead to a reduction in peak intensity by 58%. Because of the reduced XUV beam divergence, we therefore expect a drop in CWE intensity of less than 30%. In fact, seen from an exclusively linear perspective, i.e. without the spatial phase properties due to the emission time, we would not expect a drop in signal at all on the MCP screen. In that case, the shape of the aperture mask would only be reproduced on the XUV beam. As the XUV spectrometer records only a certain centre part, no change could be detected with only the spectrometer.

To test this, the same gradient scan was therefore repeated at the lower laser intensity as shown in Figure 9.3. The colour scale is kept the same, which allows a direct comparison of XUV intensities. For the steepest gradient, we indeed do not observe a drop in signal. This is also clearly visible in a direct comparison of the spectra recorded for the steepest gradients at two different laser intensities, shown in Figure 9.4. The XUV intensity is almost the same in both cases underlining the linear generation properties. We only notice a broader harmonic structure at lower intensity, as expected from the CWE emission time properties [108]. On the contrary, for longer gradients that should in principle favour the ROM mechanism, the signal drops sharply (Figure 9.3), indicating a highly nonlinear behaviour, a strong sign that we observe some form of transition from CWE to ROM.

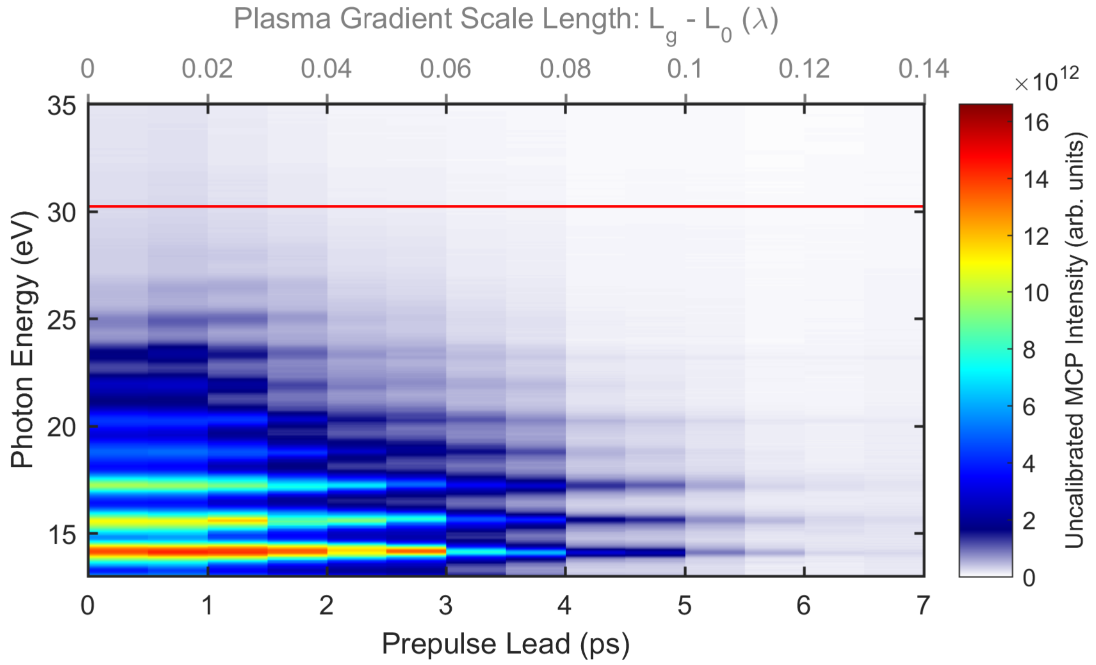

Figure 9.3. Angularly integrated harmonic spectra for different plasma gradient length (gradient scan) created by a varying pre-pulse lead time. Harmonics were generated with 24 fs driving pulses and a reduced pulse energy with a peak intensity of $a_0 = 0.6$, recorded over a sequence length of 100 ms. The red line denotes maximum plasma frequency. Background subtracted using data acquired at larger pre-pulse lead time, where the harmonic signal disappears.

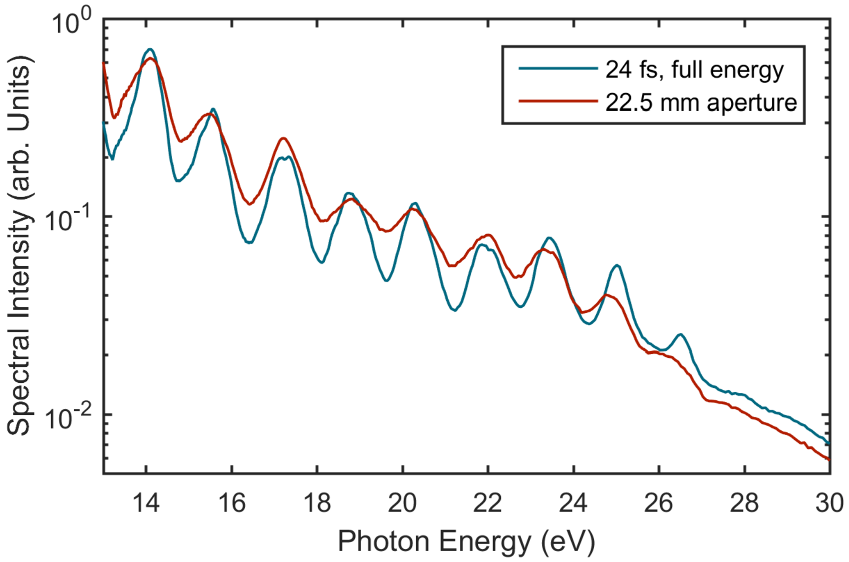

Figure 9.4. Angularly integrated and calibrated harmonic spectra for steepest plasma gradients and two different laser intensities ($a_0 = 1$ and $a_0 = 0.6$). The intensity was reduced by introducing an aperture inside the main laser beam.

Harmonics above the maximum plasma frequency In order to observe harmonics above the maximum plasma frequency, which can only be generated by the ROM mechanism, we increased the laser intensity by reducing its duration. Figure 9.5 shows a gradient scan recorded using 9 fs and $a_0 = 1.8$. As the overall laser energy remains the same, we did not expect a drop CWE signal intensity, although this seemed to be the case. Nevertheless, we again observed a clear thinning out of the harmonic peaks starting around $\lambda/40$. There seems to be an optimal gradient for ROM harmonics centred around 0.065λ, for which harmonics above the plasma frequency appear. In an enhanced view, shown in Figure 9.6, one can distinguish three to five harmonic orders above the plasma frequency, even though they are quite weak.

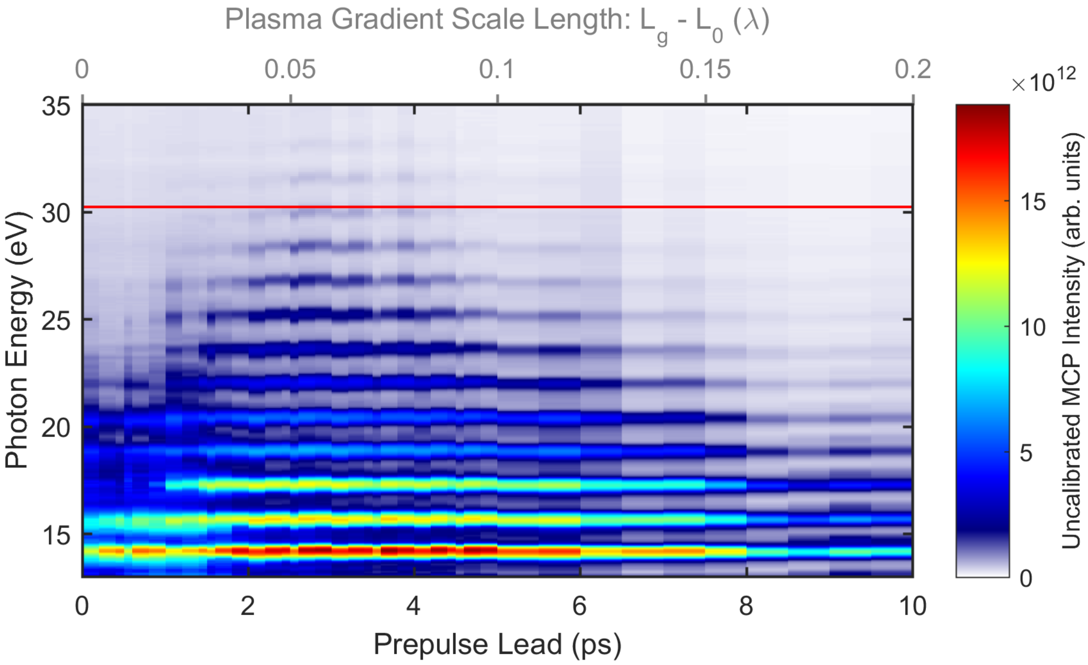

Figure 9.5. Angularly integrated harmonic spectra for different plasma gradient length (gradient scan) created by a varying pre-pulse lead time. Harmonics were generated with a 9 fs driving pulses and a peak intensity of $a_0 = 1.8$, recorded over a sequence length of 100 ms. The red line denotes maximum plasma frequency. Background subtracted using data acquired at larger pre-pulse lead time, where the harmonic signal disappears.

Figure 9.7 shows the calibrated harmonics spectrum for a gradient of $\lambda/20$. The maximum plasma frequency is indicated by the horizontal red line and the green line indicates the theoretical scaling law for the harmonic order intensity $n_H^{-8/3}$ [91]. The harmonic spectral profile does seem to follow this trend even though at this

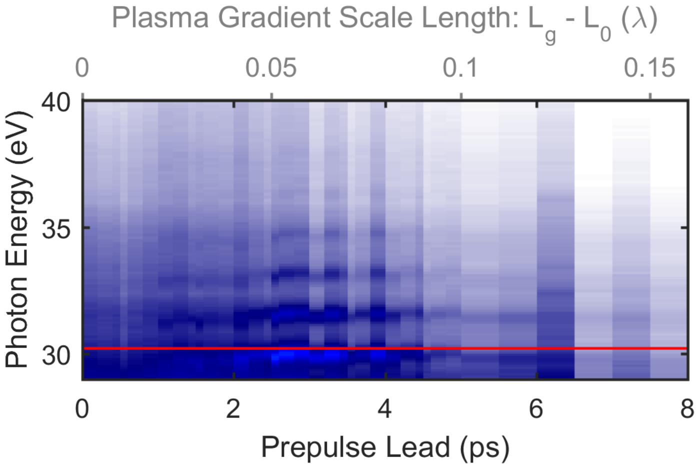

Figure 9.6. Enhanced colour representation of a cut-out of Figure 9.5.

laser intensity one would expect the harmonics to cut-off rather around order 12 instead of 16. One has to admit that our experiments seem completely unsuited to derive any scaling law, because we only see a limited number of harmonics and, as we will see later, the spectrum did decay more rapidly during other experimental runs on a different day.

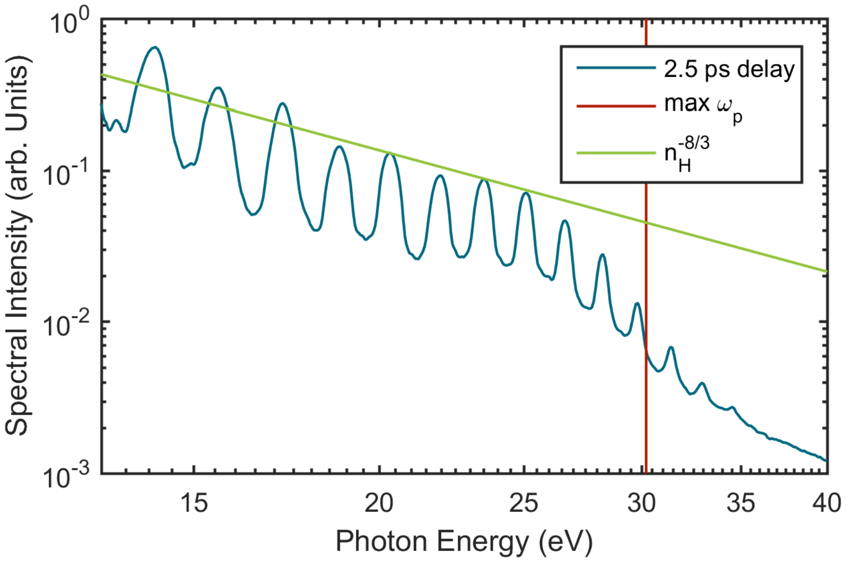

Figure 9.7. Angularly integrated and calibrated harmonic spectra for a plasma gradient of $\lambda/20$ and a laser duration of 9 fs. The estimated peak intensity is $0.64 \cdot 10^{19}\,\mathrm{W\,cm^{-2}}$; $a_0 = 1.8$. The red line denotes the maximum plasma frequency while the green line short the theoretical power law for the decay of the intensity of the spectral harmonic peaks.

Harmonic beam divergence When looking at the XUV spatial beam profile, the expected behaviour is also well reproduced. Figure 9.8 shows a gradient scan using a 9 fs driving laser and an $a_0 = 1.8$. For steep gradients, we observe a significant structure inside the XUV spatial beam profile, which is typical of CWE, as the full laser focus contributes to the generation process (little or no nonlinear spatial filter effects).

As the gradient increases so does the beam divergence. As seen previously the emission time dependence on the intensity increases with increasing gradient and we therefore get a stronger spherical phase imprinted on the harmonics beam leading to an increase in divergence.

For longer gradients as we transition into the ROM regime, the divergence now decreases and a homogeneous round beam appears. At our laser intensities, the ROM mechanism generates a flat spatial phase and the strong non-linearity should in principle affect some form of spatial filtering in the focal plane. As CWE and ROM beams overlap, it is difficult to determine an optimal gradient for the ROM mechanism. We do see, however, that the signal remains high even for gradients up to $\lambda/4$. This is in contrast with the spectrally resolved gradient scans presented earlier. The XUV spectrometer samples the beam through a few mm thick slit at the entrance in the centre. What the spatially resolved gradient scan shows, however, is that the beam slowly drifts to the side with increasing gradient, which explains why the harmonic signal drops already at shorter gradients.

It remains unclear if this effect is purely due to imperfect pre/main-pulse overlap at focus, or to the generation process itself. If the main-pulse does not hit exactly the centre of the pre-pulse, it will experience an inhomogeneous plasma expansion tilted towards one side. A simple estimation of the transverse plasma expansion made this the plausible cause. It is important to note, that this effect occurred despite the near- and far-field beam monitoring showing correct beam overlap.

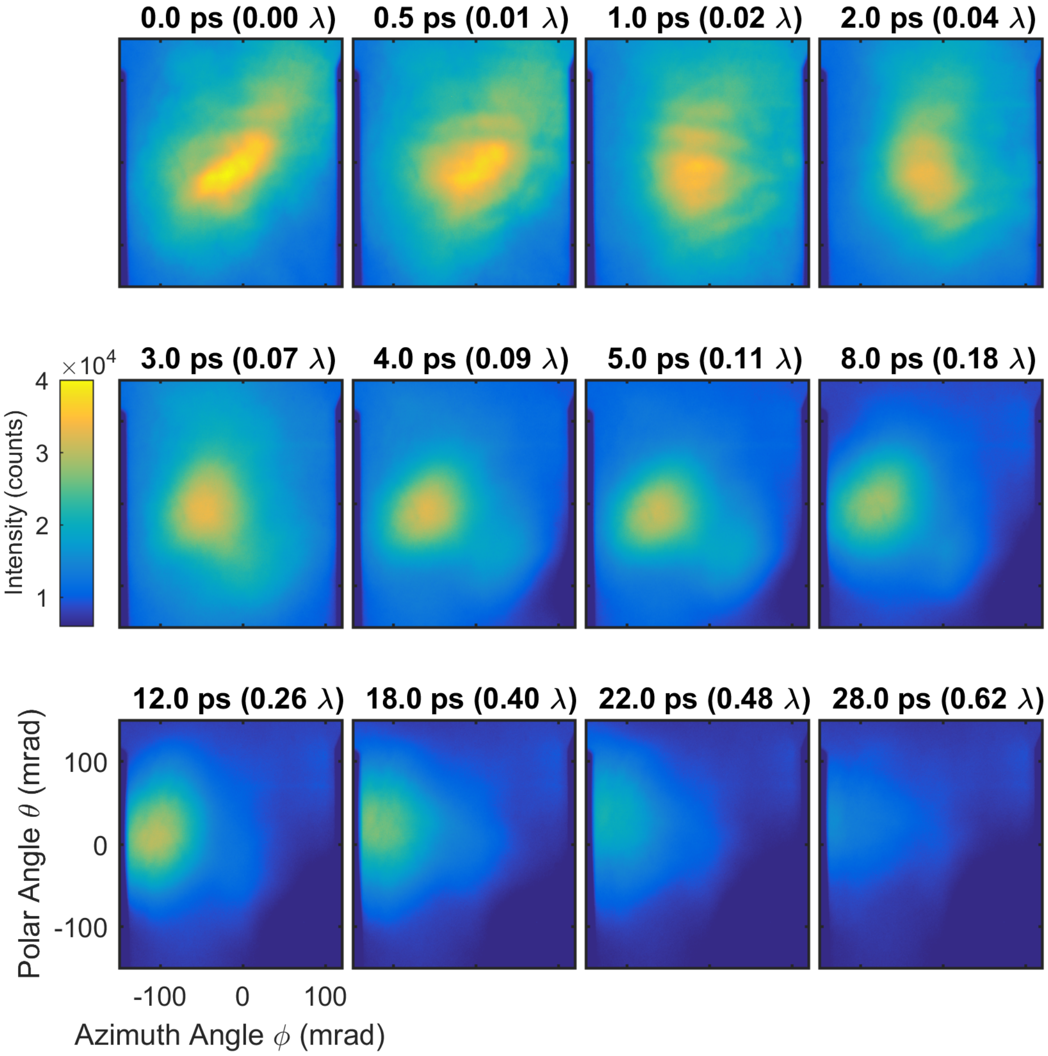

Figure 9.8. Non-normalized XUV spatial beam profiles recorded with a MCP placed looking at the target specular direction. The laser pulse duration was 9 fs with a peak intensity of $a_0 = 1.8$. Plasma conditions have been varied by the pre-pulse from the steepest to 0.62λ plasma gradient length

Interferences between CWE and ROM We have seen that CWE and ROM harmonics exhibit different emission times. In the transitional regime, where both mechanisms contribute to the observed harmonic signal, we expect to see interferences in the spectral domain as was observed in the spatial domain in [102]. To test this we recorded a high-resolution gradient scan using 9 fs driving laser pulses. The delay step size was 0.15 ps (0.003λ) and in order to prevent any systematic bias, the harmonic spectra were recorded for random delays. As can be seen in Figure 9.9 an interference pattern forms in the harmonics spectra, which shifts with increasing gradient. The peak and valleys of this interference pattern are marked with a dashed white line to guide the eye.

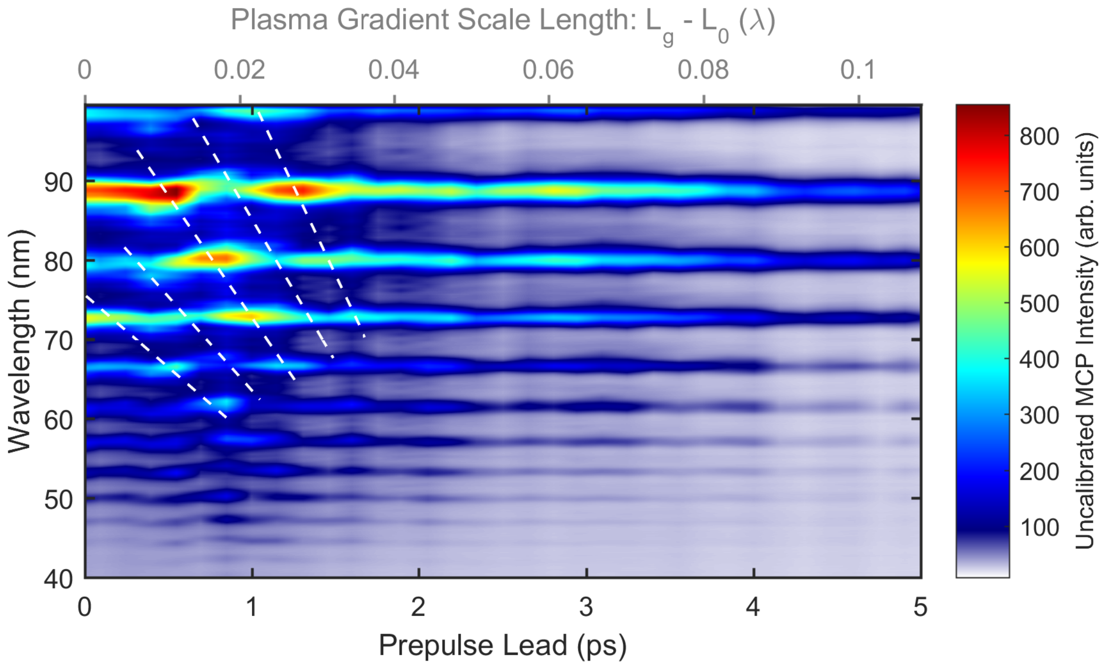

Figure 9.9. Gradient scan at 9 fs showing the interferences between CWE and ROM harmonics. Interpolated to better show the interference pattern.

From this, it is actually possible to retrieve the relative delay between attosecond pulses generated via CWE and ROM mechanisms. For a gradient of $\lambda/100$, the interference pattern has a spacing of roughly 1.2 PHz, which corresponds to a delay between the attosecond pulses of ±0.83 fs or $\pm 0.3 T_L$, where T_L is the laser period. It is important to note here that the sign of this delay is undetermined and only corresponds to an average time delay between pulses of the train. This delay slowly decreases toward longer gradients visible by the increased slope of the dashed-lines. For a gradient of $\lambda/35$ the delay retrieved is ±0.78 fs or $\pm 0.29 T_L$.

This method, of course, only offers a crude estimation. With even better resolved scans, this approach could be used in the future to properly determine the relative spectral phase between ROM and CWE attosecond pulses.

Time to space mapping of emission properties The different CWE and ROM emission properties can also be shown in another experiment. We have seen that in the CWE regime a compressed Gaussian pulse generates an aperiodic pulse train with increasing delay between consecutive pulses. At our laser intensities there is not such effect in the ROM regime. By rotating the driving laser wavefront in focus (attosecond lighthouse effect [72, 115]), we can map the temporal emission properties onto the spatial properties of the harmonic beam.

Attosecond pulses generated during the rising edge of the pulse are emitted upwards, while the ones generated at the trailing edge of the pulse are emitted downwards, which should be observable on the XUV spectrogram. We therefore expect that the top part of the XUV spectrogram should show the harmonics generated in the beginning. The vertical axis basically becomes the time axis of emission, convoluted by the divergence of the XUV beam. By applying only a small WFR the divergence is large enough that no individual attosecond pulses are emitted and the typical harmonic spectrum remains visible.

In the CWE regime we expect a *tilting* of the harmonics. At the beginning, and therefore the upper part of the spectrogram, the attosecond pulses are emitted with a shorter delay between them. At the end with a longer delay. A longer delay between pulses means in the spectral domain a faster modulation. The harmonics tilt towards the blue.

We can see this in an experiment with 9 fs pulses and a wavefront rotation (WFR) in focus of $\sim 5\,\mathrm{mrad\ fs}^{-1}$. We recorded the spectrogram for different gradient scale length. These are all shown in Figure 9.10. And a negative pre-pulse lead time we have the steepest plasma gradient. The harmonics appear tilted as was expected from the CWE regime. But towards longer gradients they straighten up, indicating the shift towards ROM mechanism with periodic pulse train.

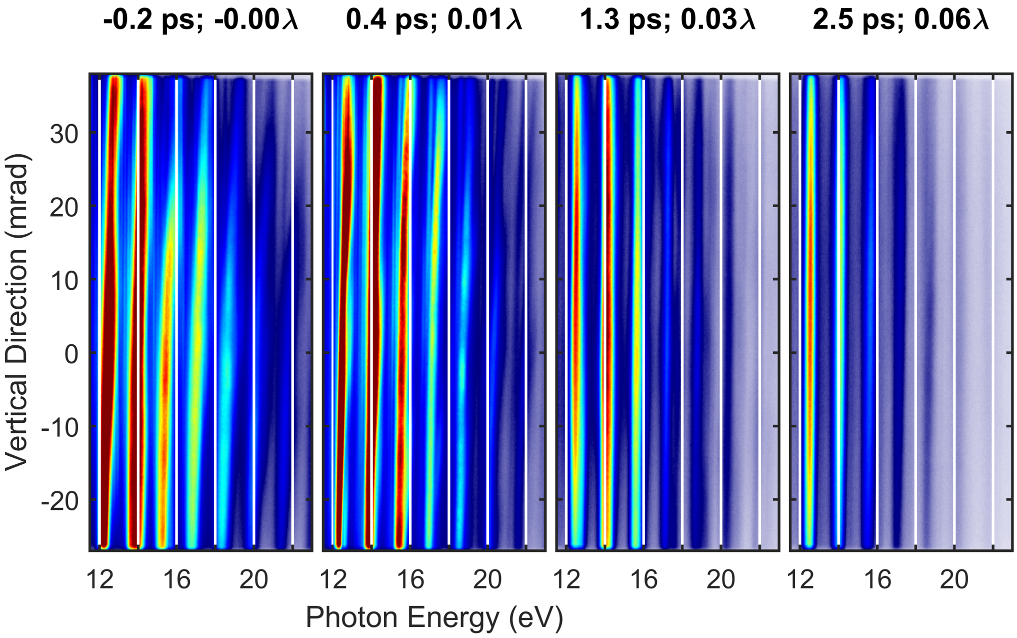

Figure 9.10. Spectrograms at different gradients for a 9 fs laser pulse with WFR applied.

9.2. SHHG with Few-Cycle-Pulses

So far I have shown results with many cycle driving laser pulses (24 fs and 9 fs). The few-cycle regime remains to be explored. For SHHG in this regime, we expect the generation of only one or a few attosecond pulses during the interaction, which should become clearly visible in our XUV spectrograms with much broader spectral features.

Keeping a constant laser energy while reducing the pulse duration will increase the laser peak intensity. We should therefore expect a higher ROM signal intensity. Figure 9.11 shows a spectrally resolved gradient scan recorded using 4 fs driving laser pulse (1.5 cycles with $a_0 = 2.2$). The CEP was random from shot to shot and therefore any CEP effects should wash out during one sequence. One can immediately note the much broader shape of the harmonic peaks and a clear optimum in generation efficiency for a gradient of around 0.08λ. The signal intensity for steep gradients is fairly low, which indicates considerably reduced contribution from CWE.

The absolute XUV intensity observed in a similar spectral range is less than a factor 2 higher compared to the case of a 9 fs driving laser pulse. For a highly nonlinear process, such as ROM, one would expect significantly more, for a two fold increase in laser intensity. Moreover the spectrum rolls off faster and components above the maximum plasma frequency become hard to see. It remains unclear if this was due to beam misalignment, i.e. higher harmonic order don't enter the spectrometer slit, or due to the actually physicals of the interaction.

The main motivation behind the use of few-cycle driving pulses is of course to generate isolated attosecond pulses, which require the stabilization of the laser CEP, in order to produce a stable and reproducible light waveform from shot to shot. At the time of experiments, however, the slow CEP out of the laser system could not be properly stabilized as explained earlier. Instead, we CEP locked the pulses from the oscillator, which insures a certain degree if CEP-stability for a short sequence of pulses (less than 50), of course the CEP changes from one sequence to the next are random. Nevertheless, by recording the relative CEP drift with the f-to-2f interferometer during experiments it was then possible to tag each data sequence to a known drift in CEP value. This approach allowed us to explore different attosecond pulse gating techniques, such as the lighthouse or amplitude gating.

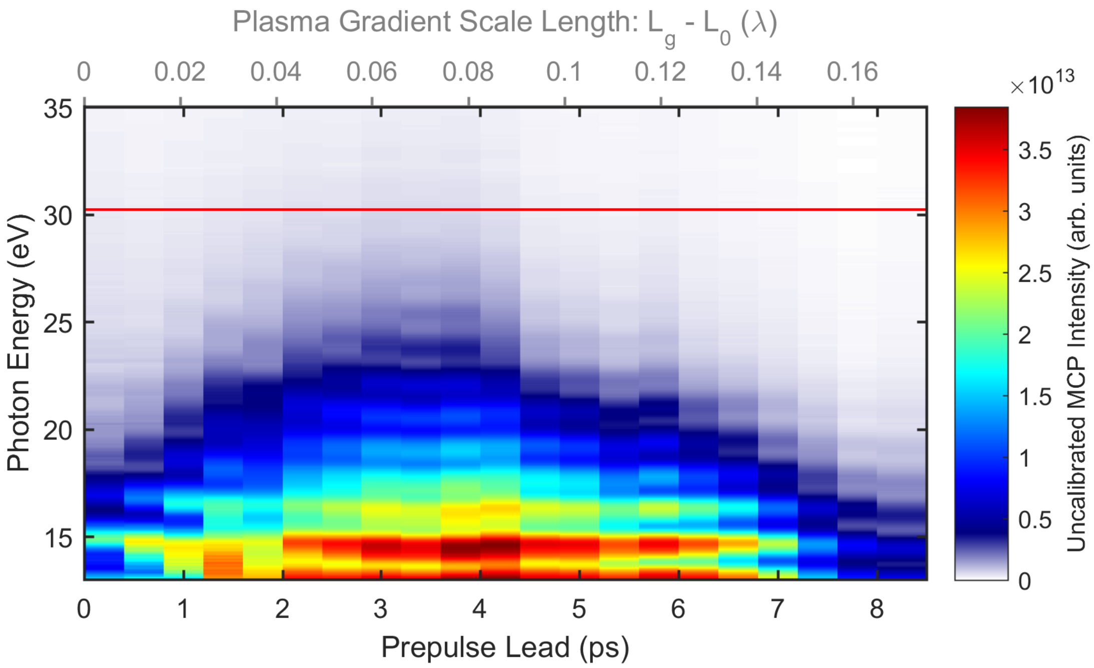

Figure 9.11. Angularly integrated harmonic spectra for different plasma gradient length (gradient scan) created by a varying pre-pulse lead time. Harmonics were generated with a 4 fs driving pulses and peak intensity of $a_0 = 2.2$, recorded over a sequence length of 100 ms and random laser CEP. The red line denotes maximum plasma frequency. Background subtracted using data acquired at larger pre-pulse lead time, where the harmonic signal disappears.

9.2.1. Single Attosecond Pulse Generation by CEP Gating

Due to the highly nonlinear nature of the ROM mechanism, we should in principle be able to generate single attosecond pulses by gating the emission stemming from the most intense cycle from the driving laser field. As illustrated in Figure 9.12, a 1.5 cycle pulse with a cosine waveform exhibiting two field maxima of intermediate strength, should generate two attosecond pulses. If the CEP of the pulse is shifted by π, the laser field changes to a cosine waveform, exhibiting a single field peak at the centre of the pulse with maximal strength, which should generate a single, more intense, attosecond pulse. We should observe the signature of this effect in the spectrogram provided that the CEP stays constant throughout one acquisition sequence.

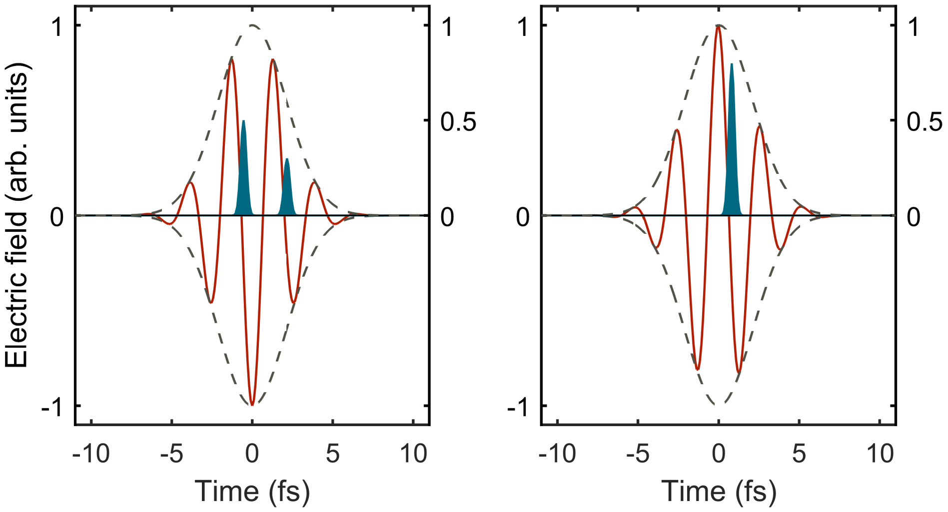

Figure 9.12. Artistic representation of the emission of either a single or a double attosecond pulse depending on the CEP for the highly nonlinear ROM mechanism.

This is exactly what we observed in the spectrograms recorded using near single cycle driving laser pulses (1.4 cycle 3.6 fs) (Figure 9.13). In this case, the sequence time had to be reduced to 30 ms (30 consecutive pulse) to ensure an acceptably constant CEP during one acquisition sequence. From one sequence to the next the CEP was random though. As can be seen in Figure 9.13 some spectrograms exhibited a modulated structure, whereas others showed a continuous like spectrum. This result has also been confirmed by single-shot acquisitions clearly indicating the generation of a single attosecond pulse for shots that had the correct CEP.

Figure 9.14 shows the angularly integrated harmonic spectra extracted from Figure 9.13 for different shot sequences (different CEP). When comparing the spec-

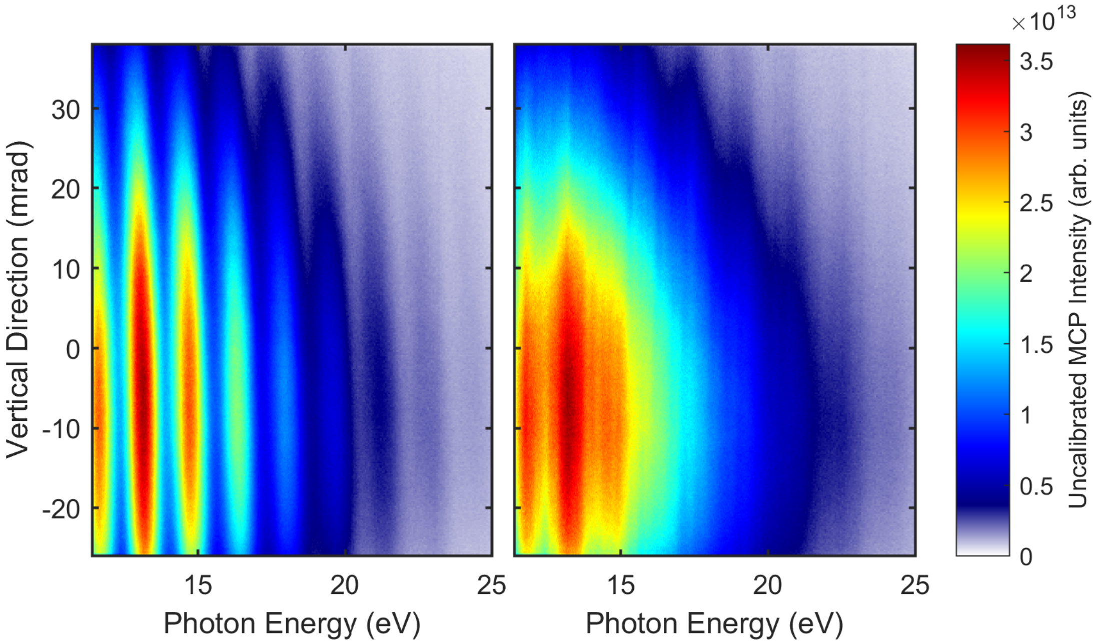

Figure 9.13. Two XUV spectrograms, presumably at two different CEP values shifted by π, shown for a laser duration of 3.6 fs and an estimated peak intensity of $1.6 \cdot 10^{19}\,\mathrm{W\,cm^{-2}}$; $a_0 = 2.7$. Sequence length reduced to 30 ms to insure stable CEP conditions throughout one acquisition.

tral intensities for both cases, one directly sees that the single attosecond pulse (continuum-like spectrum) contained more energy than the modulated harmonic spectrum (double attosecond pulses). In fact, it contains 15% to 30% more energy than the double pulse structure, depending on where the spectral integration is initiated. This result is in agreement with a non-linear process where higher intensities lead to increased conversion efficiency.

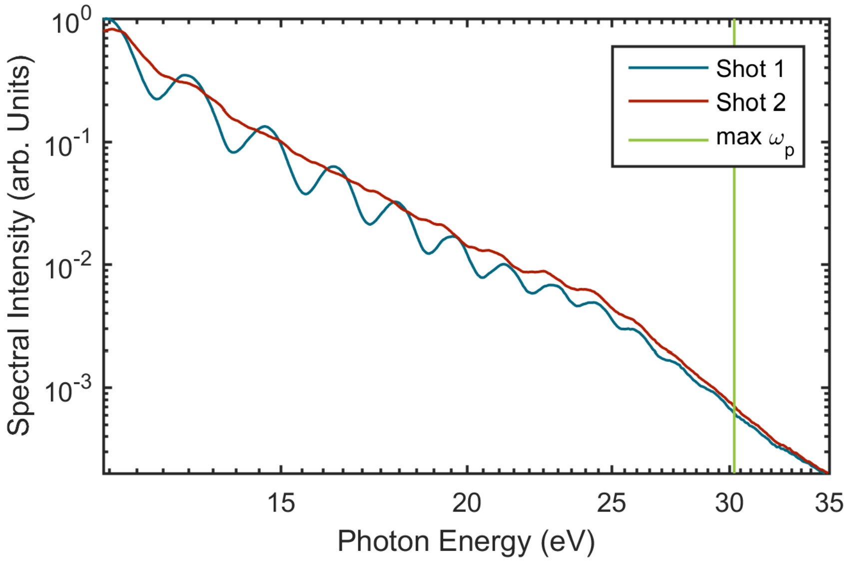

Figure 9.14. Angularly integrated harmonic spectrum from Figure 9.13.

The crucial question is whether this effect actual correlates to the CEP drift. If this were not the case, our interpretation for single attosecond pulse generation would not be true. To test this, we recorded around 200 sequences of 30 ms each, while continuously monitoring the CEP drift with the f-to-2f interferometer. By tagging the acquisitions to the recorded CEP drift, we were able to correlate the modulations in the harmonic spectrum to actual changes in CEP. From Figure 9.15 one can see there is an offset of π between the emission of modulated to continuous like spectrum.

This effects becomes even more evident in calculating the modulation depth for harmonic order 8. Figure 9.16 shows this modulation depth as a function of relative CEP offset. It varies between 1 and approximately 2, where 1 indicates a continuous spectrum and 2 a modulation depth of 50%. The modulation depth does not reach values higher than 2, probably because of finite CEP jitter between shots during the sequence. Single-shot acquisitions actually show a modulation depth up to a factor 12 or 92%, which corresponds to the beating of two attosecond pulses of almost identical intensity.

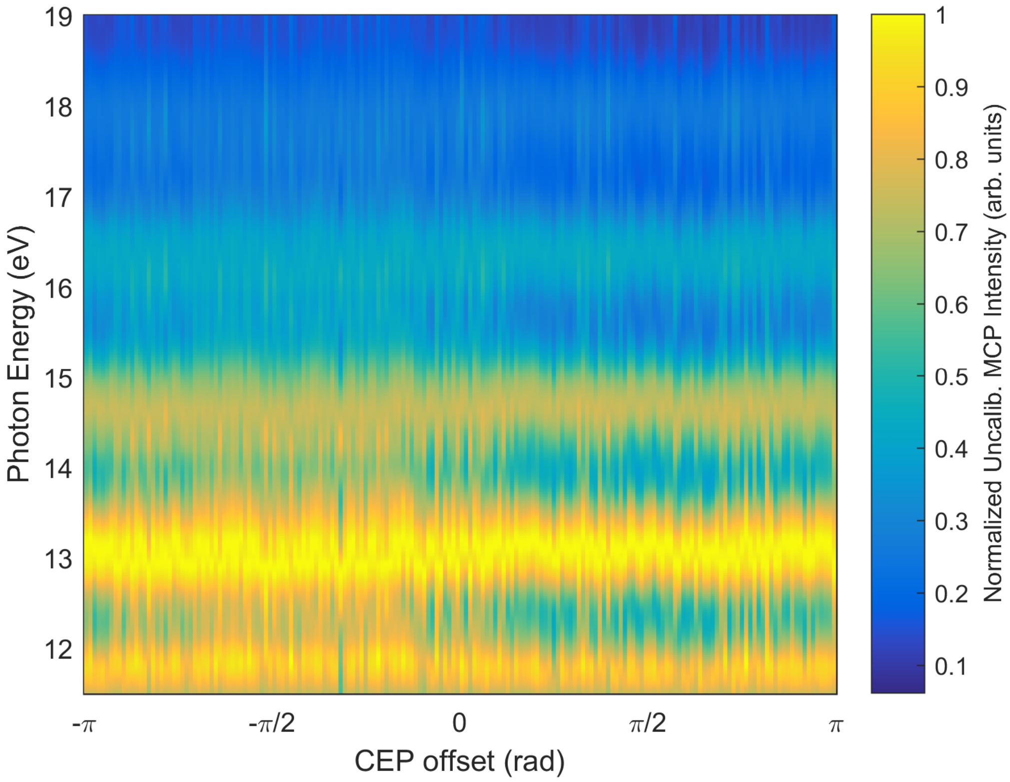

Figure 9.15. Angularly integrated harmonic spectrum ordered by their respective CEP offset value that was tagged with the f-to-2f interferometer. Recorded for a 3.6 fs driving laser ($a_0 = 2.7$) in plasma conditions for the ROM mechanism.

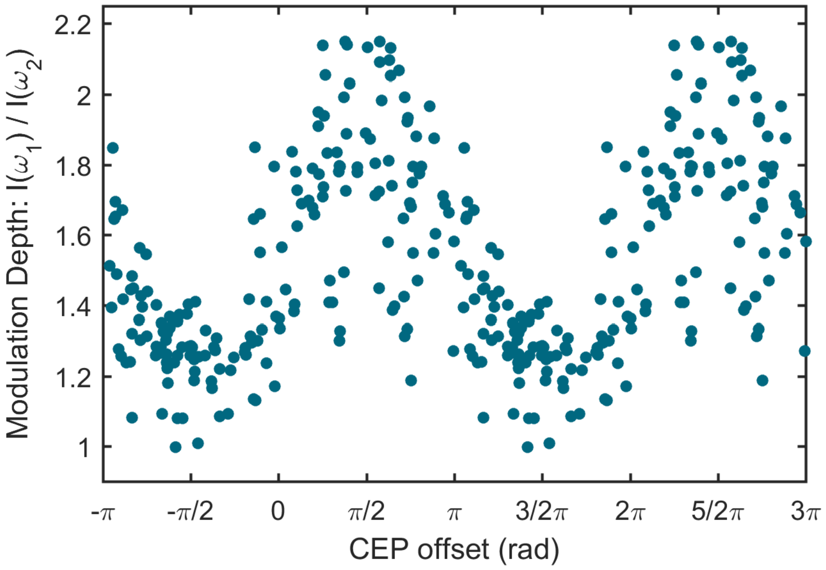

Figure 9.16. Modulation depths of the 8th harmonic from Figure 9.15 in dependence to the tagged CEP offset value. Data has been duplicated and attached at the side to better visualize CEP dependence.

Two dimensional PIC simulations performed by Maxence Thevenet at the Berkeley Lab in California, USA confirm this interpretation. The physical parameters for the simulation are summarized in Table 9.1. They match the experimental conditions very closely. The simulation has been run with four different CEP values (0; $\pi/2$; π; $3\pi/2$).

Figure 9.17 shows the harmonic spectral intensity for harmonic order 0 to 11 for different CEP values and a 3.5 fs driving laser pulse. The CEP variations for the short driving pulse clearly show an effect on the harmonic structure. A

Central wavelength	800 nm
Focus waist	1.53 μm
Duration	3.5 fs FWHM
CEP	$0; \pi/2; \pi; 2/3\pi$
Intensity	$a_0 = 2$
Incidence angle	55°
Max. plasma density	$400n_c$
Gradient scale length	$\lambda/10$

Table 9.1. Parameters for 2D PIC simulation.

CEP value of $3\pi/2$ led to a continuous like spectrum towards the higher orders. This CEP value corresponds to an optimal push-pull of the electrons by the laser. That means the laser pushes the electrons the strongest towards the plasma and then accelerates them the strongest outwards at the sign change of the laser field together with the space charge effects. A CEP value shifted by π, on the other hand, led to a deeply modulated harmonic structure, as was also the case in our experiment. As a reference the spectrum for a 9 fs driving laser pulse and the same pulse energy is shown in bright red. For this duration and intensity, the generation efficiency is clearly lower and the harmonic peaks are thinner.

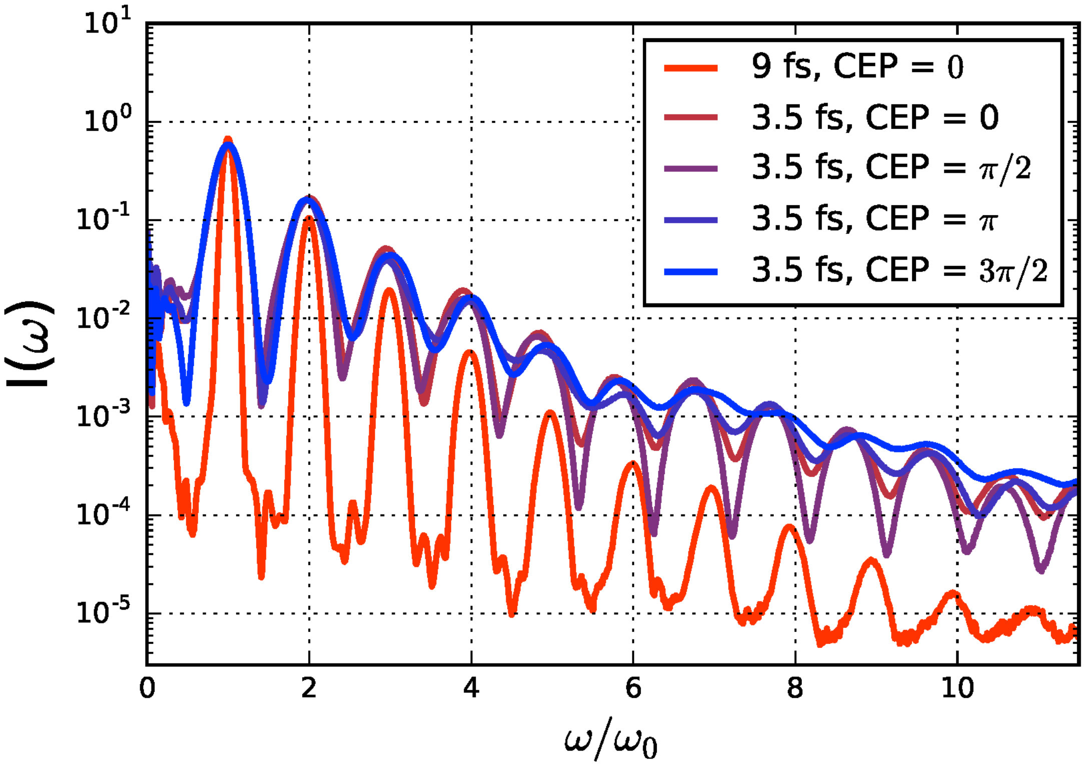

Figure 9.17. Harmonic spectral intensity calculated by 2D PIC simulations for 3.5 fs and 9 fs driving laser pulse duration. The intensity was $a_0 = 2$ and $a_0 = 1.24$ respectively. In case of the short pulse the simulation was run at 4 different CEP values of the driving laser.

Our interpretation of the harmonic spectrum in the experiment was that either a single or a double attosecond pulse was generated. In the simulation we have the advantage of having a direct access to the incident and reflected laser field. For 4 different CEP values and the short driving laser pulse, Figure 9.18 shows the incident field intensity on the left and the reflected field intensity on the right.

The first conclusion is indeed that a correct CEP value leads to the generation of a single attosecond pulse. In fact, the laser incident field is compressed in such a way, that directly a single attosecond pulse emerges, even without the usual spectral filtering. The FWHM duration is 189 as. The side peaks are at less than 10% of the main peak intensity, which justifies to regard it as a single attosecond pulse for nonlinear pump-probe applications. Comparing the incident and reflected field intensity shows the generation of an attosecond pulse of relativistic intensity. The conversion efficiency is indeed very high. The 2D simulation showed that 58% of the incident pulse energy is contained in the single attosecond pulse and 11% within the FWHM width. Translated into three dimensions, this corresponds to between 42% and 45% if one symmetrizes the pulse from either side. Because no filter is needed, the peak intensity for attosecond applications would be unprecedented high.

In conclusion this section showed convincingly the generation of single attosecond pulses through CEP gating on solid targets. Even though no temporal measurement was performed, the simulation showed the direct generation of a single attosecond pulse. No further filtering would be necessary for direct use in applications. This makes it particularly appealing. If the coherent contrast around the attosecond pulse is of importance, a spectral filter, like a thin aluminium sheet, would lead to a high contrast attosecond pulse.

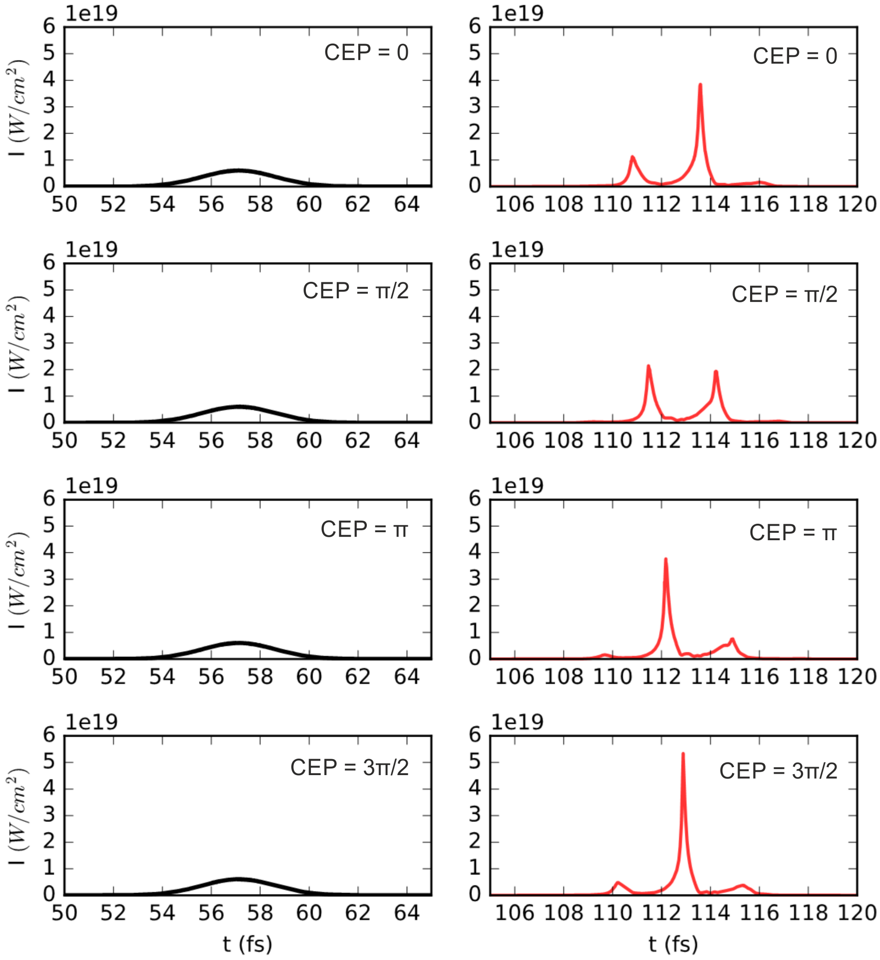

Figure 9.18. Incident (left) and reflected (right) field intensities calculated by 2D PIC simulations for a 3.5 fs driving laser pulse with an intensity of $a_0 = 2$ and four different CEP values.

9.3. Electron Acceleration

Even though electron acceleration was not intended to be a major topic of this thesis, the fast electron spatial diagnostic was always present in the set-up. It aided as an additional diagnostics for proper focus alignment and various other laser parameters.

Already during the experimental campaigns in the framework of Maimouna Bocoum's PhD, we observed a high energy ($\sim 0.5\,\mathrm{MeV}$) electron beam generated between target normal and specular directions [119]. As these electron bunches are potentially of extremely short duration, they could be interesting for applications such as femtosecond electron diffraction.

During these experiments, we observed the anti-correlated emission of CWE harmonics and electrons [118]. Short gradients favour CWE harmonics as explained in Chapter 7, whereas electron acceleration benefits from the charge separation field produced at longer gradients. The electron acceleration mechanism can be described by a simple push-pull mechanism. First the laser electric field pushes the electrons into the plasma while the ions remain static. This leads to the build-up of a space charge field. Once the laser field reverses sign, electrons are then accelerated towards vacuum with the addition energy provided by the space charge field. They exit the gradient and are injected into the laser field at its zero crossings, where they can then be further accelerated via vacuum laser acceleration [124].

At the time of the experiments, we were unable to observe ROM harmonics. We could however already see that optimal electron accelerations occurred efficiently at softer gradients, similar to the gradients for ROM harmonics. This sounds reasonable as the ROM harmonics are generated on top of fast electron jet, triggered by the driving laser field (γ-spikes).

As we are now able to reach the relativistic intensity we observed the correlated emission between ROM harmonics and fast electrons. Figure 9.19 shows a spectrally resolved gradient scan recorded for 9 fs driving pulses, where we now include simultaneous detection spatial electron distribution, recorded on the LANEX screen. We can see the formation of a strong electron beam ($\sim 30\,\mathrm{pC}$ at $L_g = 0.1\lambda$) close to direction of target specular at gradient around $\lambda/10$. Although it is not a sharp optimum, it correlates to the onset of ROM harmonics generation for a gradient between $\lambda/40$ and $\lambda/5$. The harmonic generation seems to be shifted slightly towards shorter gradients, especially the higher orders. It remains unclear if this is physical or is due to the XUV-beam wandering away from the spectrometer entrance with increasing gradients, as described earlier in Figure 9.8. This correlated emission opens up new possibilities for synchronous pump-probe experiments with femtosecond electron bunches and attosecond light pulses. This has also been previously observed by Fabien Quere's group at the CEA [125].

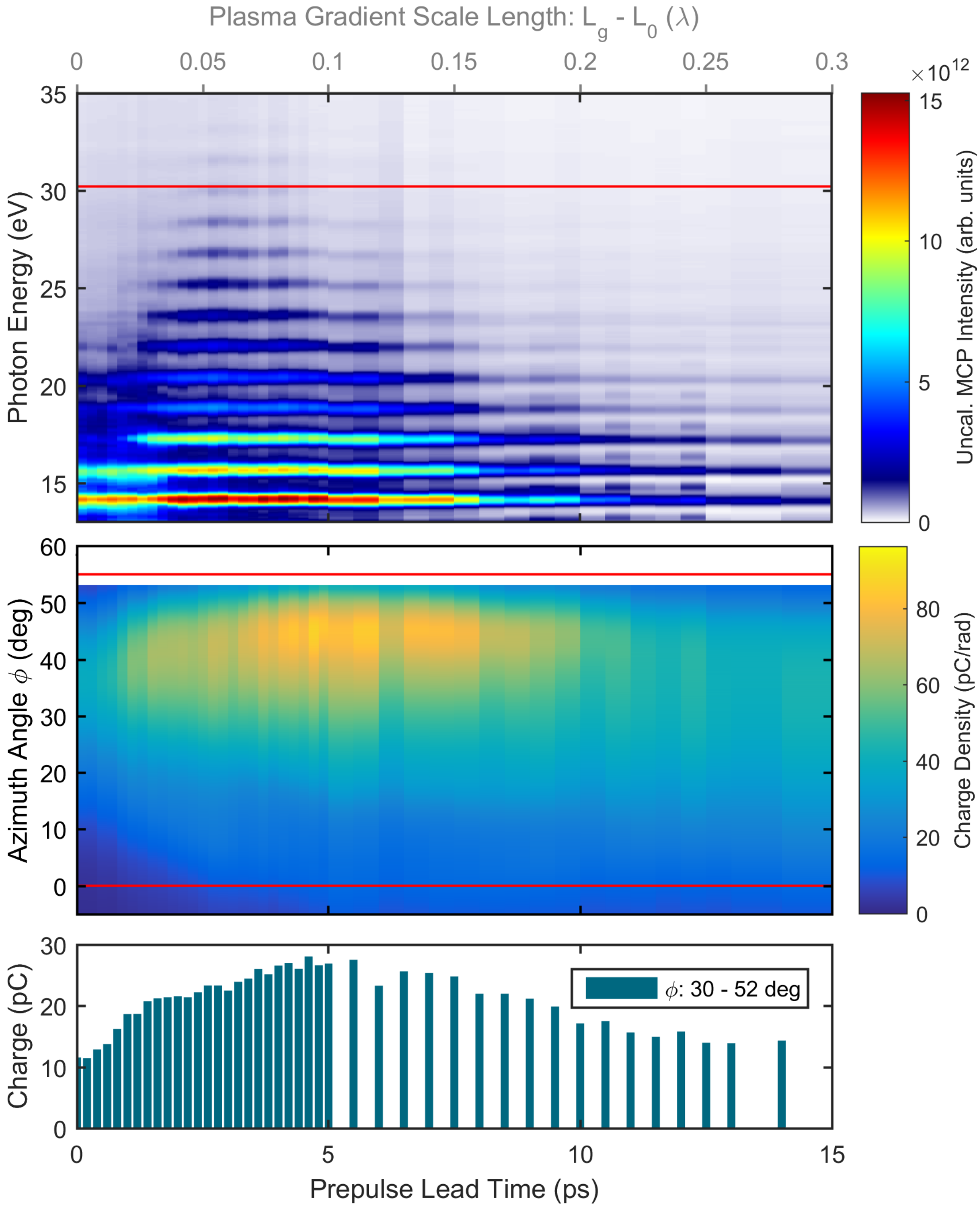

Figure 9.19. Simultaneous detection of HHG and electrons during a gradient scan for a laser pulse duration of 9 fs. The estimated peak intensity is $0.64 \cdot 10^{19}\,\mathrm{W\,cm^{-2}}$; $a_0 = 1.8$. Top graph shows the typical harmonic emission. Centre graph shows the spatial, vertically integrated, electron charge flux emitted between target normal (bottom red line) and target specular direction (top red line). The bottom graph shows the integrated electron charge between an emission angle of 30 to 52°.

9.3.1. Electron Acceleration at Long Gradients

During some gradient scans, we observed an unusual regime for electron acceleration at very long gradients, typically where no signal was expected. To further investigate this phenomenon, we devoted one day to the exclusive measurement of electrons acceleration. For this, we installed the Lanex screen in a position where it completely covered the target specular direction, thereby precluding any observation of harmonic emission. Although no harmonic emission could be observed, we were quite confident to be in the same experimental conditions as required to observe ROM harmonic emission except the gradient scale length.

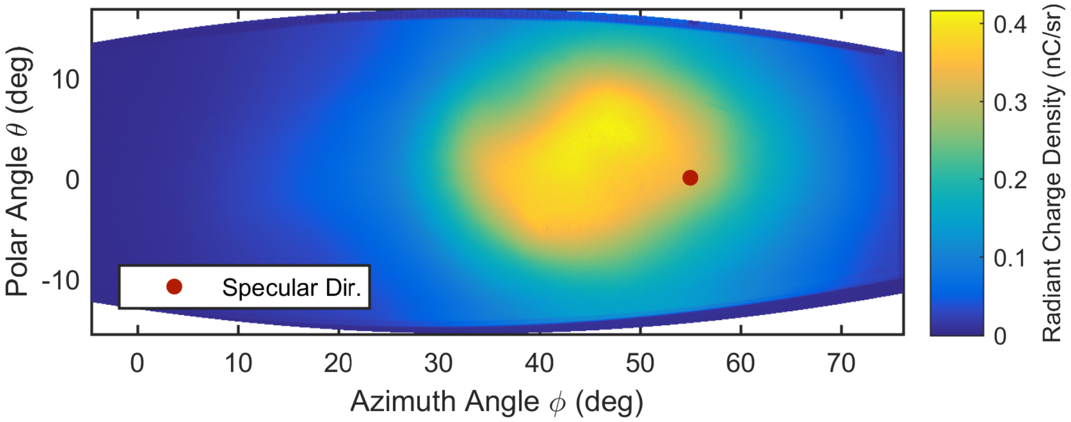

Figure 9.20. Spatial electron profile recorded with a Lanex screen placed around the target covering angles from target normal to target specular direction and beyond. Recorded from a laser with a pulse duration of 4.3 fs hitting a plasma with a gradient scale length of roughly 3λ. Target specular direction denoted by red point.

In Figure 9.20 we can see an apparent high quality electron beam with a divergence of around 25° and a centre roughly 10° away from the target specular direction towards target normal. It was recorded with a laser pulse duration of 4.3 fs hitting a plasma with a gradient scale length of roughly 3λ. With 90 pC on average per laser shot this electron beam exhibits a high charge and remained very stable from one sequence to the next.

We further investigated this novel acceleration mechanism, by scanning the gradient for different driving laser pulse durations, as shown in Figure 9.21. The top graph shows a gradient scan recorded with a laser pulse duration of 24 fs. At medium gradients ($0.1\lambda < L_g < 1\lambda$) we can observe the usual electron emission explained earlier by the push-pull mechanism and followed by vacuum laser acceleration (VLA). No significant electron emission could be observed for longer gradients.

This radically changed when going to shorter pulses and therefore higher intensities. The same scan was repeated for decreasing pulse durations down to 3.5 fs ($a_0 = 1$ to $a_0 = 2.8$). As the pulse energy stayed constant, this means the peak intensity was increased accordingly up to a maximum of $a_0 = 2.8$ for the 3.5 fs pulse.

The signal at intermediate gradients did not change that much, which might indicate a saturation effect. It could also mean, however, that the charge distribution shifted towards higher energy electrons (energy above 1 Mev), where the LANEX response strongly drops. The recorded signal could then remain unchained, despite an overall increase in charge.

At longer gradients we can see the appearance of strong electron emission, with the strongest signal generated with a 5 fs driving laser pulse. At 10 fs the electrons are emitted in the specular direction with a charge up to 30 pC. For shorter pulse duration the direction of emission shifts slightly towards target normal while the integrated charge dramatically increases. At 5 fs we observe the most intense electron beaming with close to 100 pC per shot for a gradient between 2λ and 4λ. At the shortest pulse duration (3.5 fs) the signal decreases again, which might indicate the onset of spatio-temporal coupling (STC) inherent to the extremely large laser spectrum.

This novel acceleration mechanism appears to be highly nonlinear. When we repeated the same set of gradients scans with an apertured laser beam (intensity drops to 11%), no significant electron emission can be observed at long gradients, despite observing the increase in signal at intermediate gradients (Figure 9.22). This nonlinear behaviour was then confirmed in a chirp scan displayed in Figure 9.23. The signal drops sharply when increasing the pulse duration up to 11 fs by chirping the driving laser pulse (positive and negative chirp).

In conclusion, we discovered a novel regime for electron acceleration on solid targets with wavelength scale plasma gradients. It has a extremely nonlinear response to laser parameters, but could become very interesting for applications given its stability and good beam characteristics. Indeed, the charge was very high compared to the electron beam generated at intermediate gradients. Unfortunately we did not have enough time to measure the electron energy. This should be done as soon as possible in the framework of the next PhD thesis on the subject.

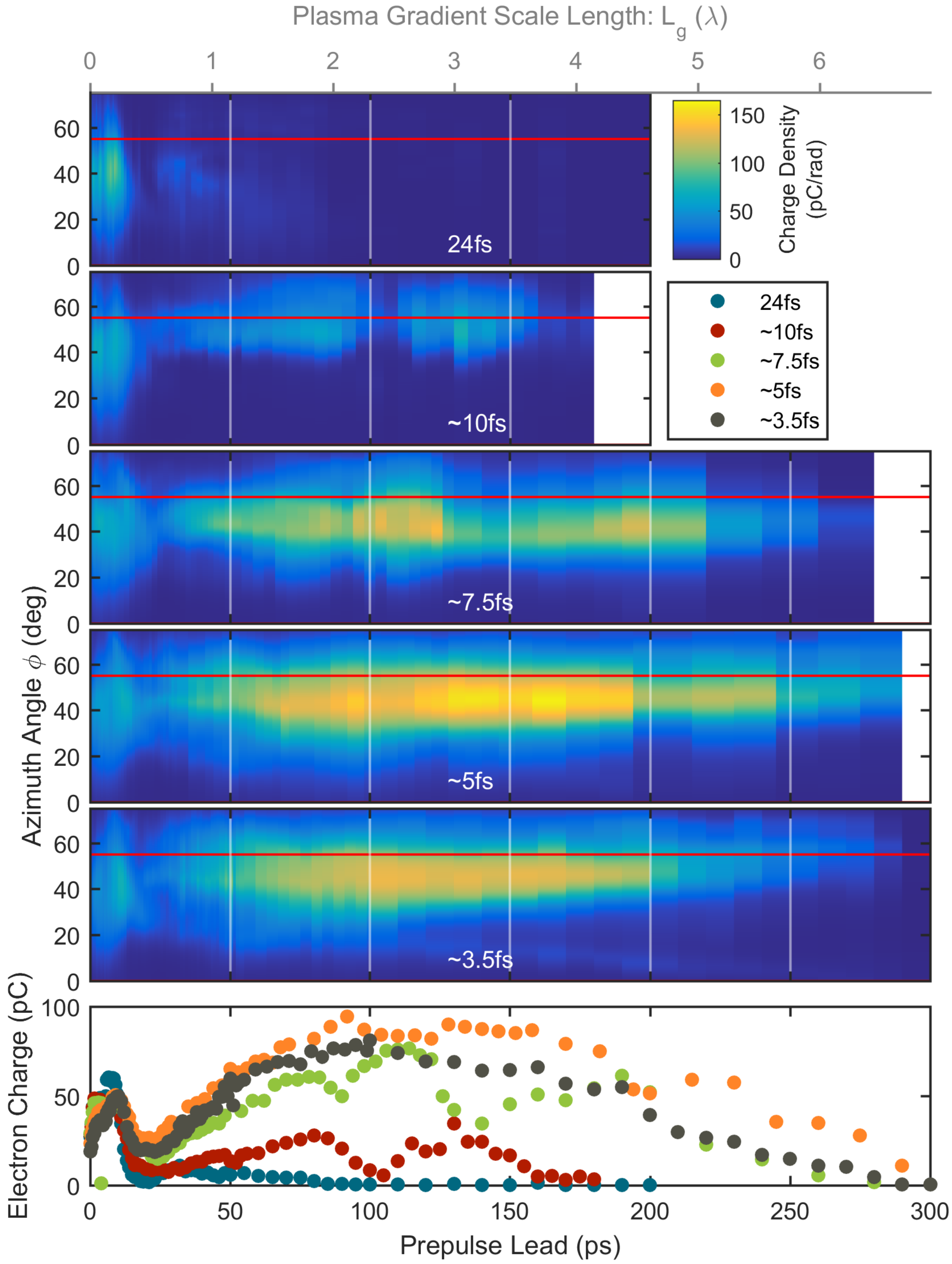

Figure 9.21. Vertically integrated, horizontally resolved electron emission in dependence to the plasma gradient length for varying laser pulse duration while keeping the focused energy constant (a_0 from $a_0 = 1$ to $a_0 = 2.8$). Red line denotes target specular direction. Integrated electron charge displays for all cases on bottom figure.

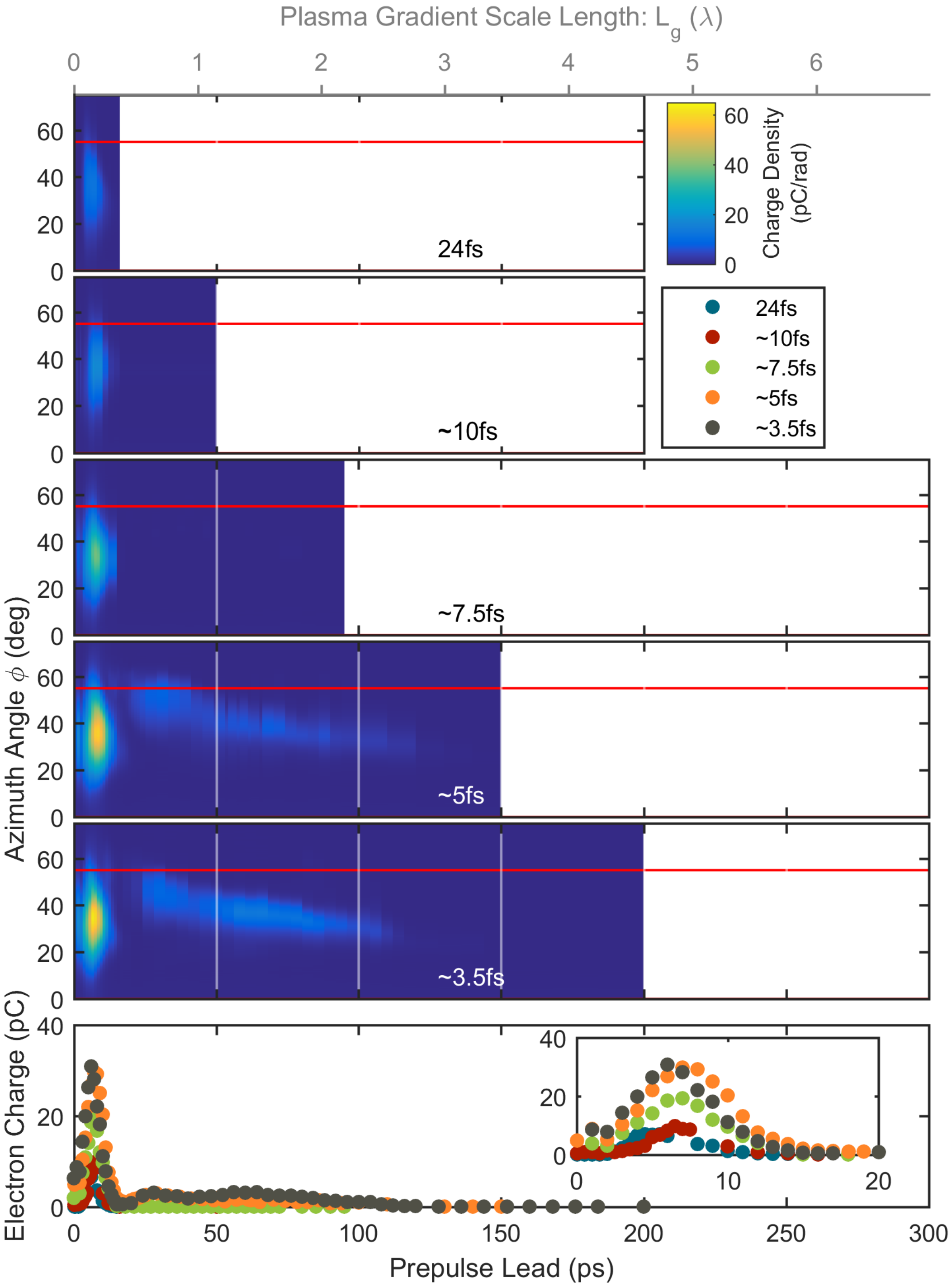

Figure 9.22. Same gradient scans as in Figure 9.21 but with a 15 mm aperture inside the laser beam. Intensity is reduced to 11%.

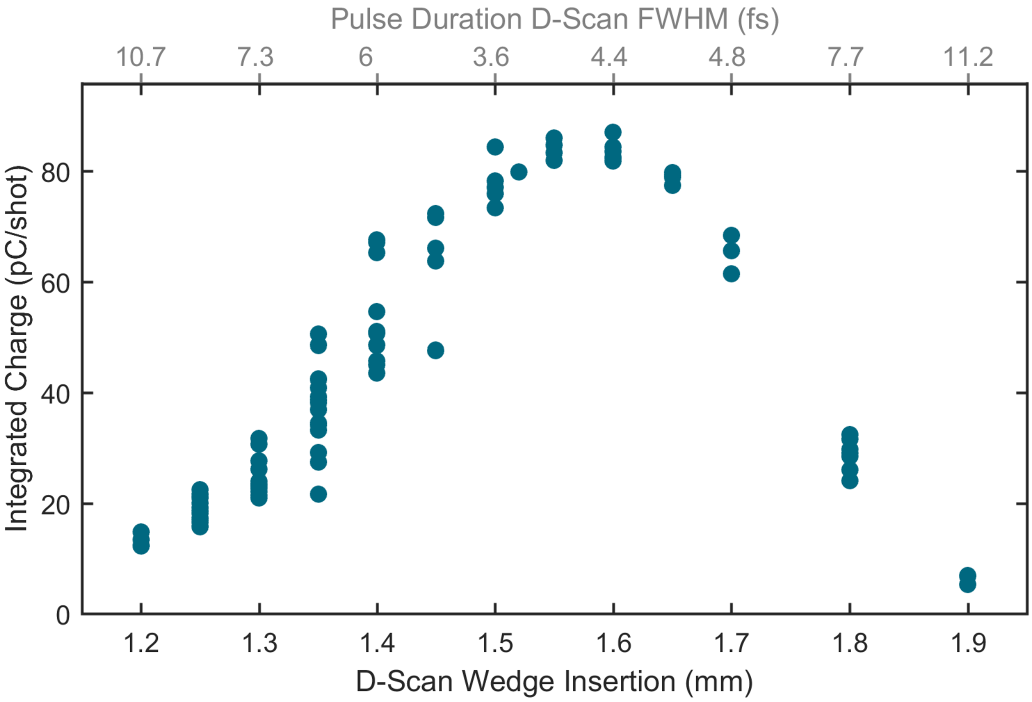

Figure 9.23. Spatially integrated electron charge in dependence for varying laser pulse durations (down to 3.5 fs and $a_0 = 2.8$) incident on a soft gradient with $\mathrm{L_g} \sim 2\lambda$.

Final Conclusion and Outlook

This thesis builds upon a long history of developmental work on the Salle Noire laser devoted to high fidelity laser plasma interaction on solid targets. I started in the group 5 years ago with my *Diplomarbeit* (Master Thesis) for the duration of 1 year. I worked with Aurélien Ricci and Aurélie Jullien on the development of the double CPA system including the GRISM compressor and the XPW filter stage.

Then with the start of my PhD I devoted my interest towards the high energy HCF post-compression idea. After initial tests with a simpler setup, we realized quickly that tremendous efforts need to put in the system to make it reliable and compatible with high energy input pulses. This led to a completely sealed setup with a vacuum chamber in front and gas chamber after the HCF. This paid off and we were able to reach TW peak power with near single-cycle-pulses. CEP stability was also shown.

Already during this development I worked together with Maimouna Bocoum on the solid HHG and electron acceleration. But then in a sub-relativistic regime with the 24 fs pulses coming out of the double CPA system. We developed the SDI technique to measure the plasma gradient scale length [117] and demonstrated anti-correlated electron emission [118].

The laser characteristics seemed good enough to perform relativistic plasma experiments, but first a vacuum beamline had to be conceived for accurate and reliable laser delivery onto the target. Also this was a crucial step and only in the final configuration we were able to control the plasma gradient accurately.

After Maimouna started to write up and I had finished the HCF setup with the vacuum beamline, I took over the solid plasma experiments to drive it in a completely new regime with the relativistic near single-cycle pulses.

During this time we achieved relativistic harmonic generation on solid targets for the first time at 1 kHz. We could see that the electron acceleration correlated to the relativistic HHG as predicted. Furthermore we gated single attosecond pulses by CEP controlling the driving laser. We can conclude, that thanks to the upgraded laser chain, we finally arrived in a completely new regime for us on solid target laser plasma interactions. This also led to the discovery of a new regime to accelerate electrons on soft gradients. This was an exciting step forward and will allow the group interesting experiments for the future to come.

In term of applications towards attosecond pump-probe experiments, this source seems certainly not ideally suited. Nowadays one would rather use gas HHG. For time resolved electron diffraction this is probably also the case and one would use gas wake-field acceleration sources. It is just so much more convenient to work in continuous operation without regard to the limit space on the solid target. But this experiment is very important in determining the scaling laws and vital insights in experimental operation for future installations. Particular as gas HHG has a limiting scaling law.

Based on the vacuum beamline and the solid target experimental chamber, we also designed the solid harmonics beamline for the kHz, high-contrast SYLOS laser at the new Extreme Light Infrastructure - Attosecond Light Pulse Source (ELI-ALPS) facility in Szeged, Hungary [126]. The final targeted laser parameters (SYLOS Phase 2) will increase the pulse peak power on target, relative to our beamline, 10 fold. The laser is supposed to reach 20 TW peak power at sub 6 fs with a CEP stability better than 200 mrad and the vacuum beamline will have a transmission of more than 50% including contrast cleaning. This beamline will open up new opportunities for high fidelity solid-target laser-plasma experiments for the next years to come. As the targeted ASE contrast level is supposed to be *only* better than 10^{10}, we design an additional plasma mirror contrast enhancement chamber to allow controlled experiments in the highly relativistic regime.

The next steps for our group will be to properly control the CEP. Also the generated attosecond pulses should be measured, which has so far been done only once from a solid target [97]. In terms of electron acceleration the energy still needs to be determined and an explanation found for the new regime at soft gradients.

Although not part of this thesis, we also performed electron wake-field acceleration in a gas jet with the laser chain and vacuum beamline under the lead of our partner group directed by J. Faure. By using the shortest laser pulse duration, high quality, relativistic electron beams ($\sim 5\,\mathrm{MeV}$) were accelerated in the bubble regime [127]. This might open up the possibility for time resolved electron diffraction experiments in our facility in the near future.

Bibliography

[1] M. Drescher, M. Hentschel, R. Kienberger, G. Tempea, C. Spielmann, et al. “X-ray pulses approaching the attosecond frontier”. In: *Science* 291.5510 (2001), pp. 1923–1927. DOI: `10.1126/science.1058561`.

[2] P. M. Paul, E. S. Toma, P. Breger, G. Mullot, F. Auge, et al. “Observation of a train of attosecond pulses from high harmonic generation”. In: *Science* 292.5522 (2001), pp. 1689–1692. DOI: `10.1126/science.1059413`.

[3] G. A. Mourou, T. Tajima, and S. V. Bulanov. “Optics in the relativistic regime”. In: *Reviews of Modern Physics* 78.2 (2006), pp. 309–371. DOI: `10.1103/RevModPhys.78.309`.

[4] D. Strickland and G. A. Mourou. “Compression of amplified chirped optical pulses”. In: *Optics Communications* 56.3 (1985), pp. 219–221. DOI: `10.1016/0030-4018(85)90120-8`.

[5] M. Perry. “Multilayer Dielectric Gratings: Increasing the Power of Light”. In: *Science & Technology Review* September (1995), pp. 25–33.

[6] R. W. Boyd. *Nonlinear optics*. 3rd ed. Amsterdam: Academic Press, 2008. ISBN: 9780123694706.

[7] R. Trebino. *Frequency-resolved optical gating: The measurement of ultrashort laser pulses*. Boston: Kluwer Academic, 2000. ISBN: 1-4020-7066-7.

[8] W. L. Kruer. *The physics of laser plasma interactions*. Vol. 73. Frontiers in physics. Redwood City Calif.: Addison-Wesley, 1988. ISBN: 0201156725.

[9] S. C. Wilks, W. L. Kruer, M. Tabak, and A. B. Langdon. “Absorption of ultra-intense laser pulses”. In: *Physical Review Letters* 69.9 (1992), pp. 1383–1386. DOI: `10.1103/PhysRevLett.69.1383`.

[10] C. N. Danson, L. J. Barzanti, Z. Chang, A. E. Damerell, C. B. Edwards, et al. “High contrast multi-terawatt pulse generation using chirped pulse amplification on the VULCAN laser facility”. In: *Optics Communications* 103.5-6 (1993), pp. 392–397. DOI: `10.1016/0030-4018(93)90163-Y`.

[11] S. Backus, C. G. Durfee, M. M. Murnane, and H. C. Kapteyn. “High power ultrafast lasers”. In: *Review of Scientific Instruments* 69.3 (1998), p. 1207. DOI: `10.1063/1.1148795`.

[12] E. W. Gaul, M. Martinez, J. Blakeney, A. Jochmann, M. Ringuette, et al. "Demonstration of a 1.1 petawatt laser based on a hybrid optical parametric chirped pulse amplification/mixed Nd:glass amplifier". In: *Applied Optics* 49.9 (2010), pp. 1676–1681. DOI: `10.1364/AO.49.001676`.

[13] W. P. Leemans, J. Daniels, A. Deshmukh, A. J. Gonsalbes, A. Magana, et al. "BELLA Laser and Operations". In: *PAC2013*. Ed. by T. Satogata, C. Petit-Jean-Genaz, and V. Schaa. 2013. ISBN: 978-3-95450-138-0.

[14] C. Danson, D. Hillier, N. Hopps, and D. Neely. "Petawatt class lasers worldwide". In: *High Power Laser Science and Engineering* 3 (2015), p. 662. DOI: `10.1017/hpl.2014.52`.

[15] O. Albert, H. Wang, D. Liu, Z. Chang, and G. A. Mourou. "Generation of relativistic intensity pulses at a kilohertz repetition rate". In: *Optics Letters* 25.15 (2000), p. 1125. DOI: `10.1364/OL.25.001125`.

[16] K. F. Wall and A. Sanchez. "Titanium sapphire lasers". In: *Lincoln Laboratory Journal* 3 (1990), pp. 447–462.

[17] C. P. Hauri, M. Bruck, W. Kornelis, J. Biegert, and U. Keller. "Generation of 14.8-fs pulses in a spatially dispersed amplifier". In: *Optics Letters* 29.2 (2004), p. 201. DOI: `10.1364/OL.29.000201`.

[18] M. Nisoli, S. De Silvestri, and O. Svelto. "Generation of high energy 10 fs pulses by a new pulse compression technique". In: *Applied Physics Letters* 68.20 (1996), pp. 2793–2795. DOI: `10.1063/1.116609`.

[19] N. Bloembergen. "Laser-induced electric breakdown in solids". In: *IEEE Journal of Quantum Electronics* 10.3 (1974), pp. 375–386. DOI: `10.1109/JQE.1974.1068132`.

[20] B. C. Stuart, M. Feit, S. Herman, A. Rubenchik, B. Shore, et al. "Nanosecond-to-femtosecond laser-induced breakdown in dielectrics". In: *Physical Review B* 53.4 (1996), pp. 1749–1761. DOI: `10.1103/PhysRevB.53.1749`.

[21] E. G. Gamaly, A. V. Rode, B. Luther-Davies, and V. T. Tikhonchuk. "Ablation of solids by femtosecond lasers: Ablation mechanism and ablation thresholds for metals and dielectrics". In: *Physics of Plasmas* 9.3 (2002), pp. 949–957. DOI: `10.1063/1.1447555`.

[22] X. Chen, L. Canova, A. Malvache, A. Jullien, R. López-Martens, et al. "1-mJ, sub-5-fs carrier–envelope phase-locked pulses". In: *Applied Physics B* 99.1-2 (2010), pp. 149–157. DOI: `10.1007/s00340-009-3835-y`.

[23] H. C. Kapteyn, M. M. Murnane, A. Szoke, and R. W. Falcone. "Prepulse energy suppression for high-energy ultrashort pulses using self-induced plasma shuttering". In: *Optics Letters* 16.7 (1991), pp. 490–492. DOI: `10.1364/OL.16.000490`.

[24] G. Doumy, O. Gobert, M. Perdrix, P. Audebert, J. C. Gauthier, et al. "Complete characterization of a plasma mirror for the production of high-contrast ultraintense laser pulses". In: *Physical Review E* 69.2 (2004). DOI: `10.1103/PhysRevE.69.026402`.

[25] A. Levy, T. Ceccotti, P. D'Oliveira, F. Réau, M. Perdrix, et al. "Double plasma mirror for ultrahigh temporal contrast ultraintense laser pulses". In: *Optics Letters* 32.3 (2007), pp. 310–312. DOI: `10.1364/OL.32.000310`.

[26] A. Borot, D. Douillet, G. Iaquianiello, T. Lefrou, P. Audebert, et al. "High repetition rate plasma mirror device for attosecond science". In: *Review of Scientific Instruments* 85.1 (2014), p. 013104. DOI: `10.1063/1.4860035`.

[27] M. P. Kalashnikov, E. Risse, H. Schonnagel, and W. Sandner. "Double chirped-pulse-amplification laser: a way to clean pulses temporally". In: *Optics Letters* 30.8 (2005), pp. 923–925. DOI: `10.1364/OL.30.000923`.

[28] A. Ricci. "Développement d'une source laser ultra-brève, stabilisée en phase et à haut contraste, pour l'optique relativiste haute cadence". Dissertation. Palaiseau: Ecole Polytechnique, 2013.

[29] F. Böhle. "Building a Source of Relativistic Intensity Few-Optical-Cycle Laser Pulses". Diplomarbeit. München: Technische Universität München, 2013.

[30] A. Borot, A. Malvache, X. Chen, D. Douillet, G. Iaquianiello, et al. "High-harmonic generation from plasma mirrors at kilohertz repetition rate". In: *Optics Letters* 36.8 (2011), pp. 1461–1463. DOI: `10.1364/OL.36.001461`.

[31] A. Jullien, O. Albert, F. Burgy, G. Hamoniaux, J.-P. Rousseau, et al. "10(-10) temporal contrast for femtosecond ultraintense lasers by cross-polarized wave generation". In: *Optics Letters* 30.8 (2005), pp. 920–922. DOI: `10.1364/OL.30.000920`.

[32] K. Osvay, L. Canova, C. G. Durfee, A. P. Kovács, A. Borzsonyi, et al. "Preservation of the carrier envelope phase during cross-polarized wave generation". In: *Optics Express* 17.25 (2009), pp. 22358–22365.

[33] J. M. Mikhailova, A. Buck, A. Borot, K. Schmid, C. Sears, et al. "Ultra-high-contrast few-cycle pulses for multipetawatt-class laser technology". In: *Optics Letters* 36.16 (2011), pp. 3145–3147.

[34] F. Lureau, S. Laux, O. Casagrande, C. Radier, O. Chalus, et al. “High energy 1 Hz Titanium Sapphire amplifier for PetaWatt class lasers”. In: *Solid State Lasers XXI: Technology and Devices*. Ed. by W. A. Clarkson and R. K. Shori. Vol. 8235. Proceedings of SPIE. Bellingham, Washington USA: SPIE, 2012. ISBN: 978-0-8194-8878-7. DOI: `10.1117/12.908127`.

[35] A. Ricci, A. Jullien, J.-P. Rousseau, Y. Liu, A. Houard, et al. “Energy-scalable temporal cleaning device for femtosecond laser pulses based on cross-polarized wave generation”. In: *Review of Scientific Instruments* 84.4 (2013), p. 43106. DOI: `10.1063/1.4801457`.

[36] A. Ricci, A. Jullien, J.-P. Rousseau, and R. López-Martens. “Front-End Light Source for a Waveform-Controlled High-Contrast Few-Cycle Laser System for High-Repetition Rate Relativistic Optics”. In: *Applied Sciences* 3.1 (2013), pp. 314–324. DOI: `10.3390/app3010314`.

[37] Z. Chang. “Carrier-envelope phase shift caused by grating-based stretchers and compressors”. In: *Applied Optics* 45.32 (2006), pp. 8350–8353. DOI: `10.1364/AO.45.008350`.

[38] N. Forget, V. Crozatier, and P. Tournois. “Transmission Bragg-grating grisms for pulse compression”. In: *Applied Physics B* 109.1 (2012), pp. 121–125. DOI: `10.1007/s00340-012-5126-2`.

[39] A. Ricci, A. Jullien, N. Forget, V. Crozatier, P. Tournois, et al. “Grism compressor for carrier-envelope phase-stable millijoule-energy chirped pulse amplifier lasers featuring bulk material stretcher”. In: *Optics Letters* 37.7 (2012), pp. 1196–1198. DOI: `10.1364/OL.37.001196`.

[40] A. Jullien, A. Ricci, F. Böhle, J.-P. Rousseau, S. Grabielle, et al. “Carrier-envelope-phase stable, high-contrast, double chirped-pulse-amplification laser system”. In: *Optics Letters* 39.13 (2014), p. 3774. DOI: `10.1364/OL.39.003774`.

[41] X. Liu, R. Wagner, A. Maksimchuk, E. Goodman, J. Workman, et al. “Nonlinear temporal diffraction and frequency shifts resulting from pulse shaping in chirped-pulse amplification systems”. In: *Optics Letters* 20.10 (1995), p. 1163. DOI: `10.1364/OL.20.001163`.

[42] N. V. Didenko, A. V. Konyashchenko, A. P. Lutsenko, and S. Y. Tenyakov. “Contrast degradation in a chirped-pulse amplifier due to generation of prepulses by postpulses”. In: *Optics Express* 16.5 (2008), pp. 3178–3190. DOI: `10.1364/OE.16.003178`.

[43] A. Baltuska, T. Fuji, and T. Kobayashi. “Visible pulse compression to 4 fs by optical parametric amplification and programmable dispersion control”. In: *Optics Letters* 27.5 (2002), p. 306. DOI: `10.1364/OL.27.000306`.

[44] L. Veisz, D. Rivas, G. Marcus, X. Gu, D. Cardenas, et al. “Multi-10-TW sub-5-fs optical parametric synthesizer”. In: *2014 IEEE Photonics Conference (IPC)*. 2014, pp. 510–511. DOI: `10.1109/IPCon.2014.6995473`.

[45] H. Nakatsuka, D. Grischkowsky, and A. C. Balant. “Nonlinear Picosecond-Pulse Propagation through Optical Fibers with Positive Group Velocity Dispersion”. In: *Physical Review Letters* 47.13 (1981), pp. 910–913. DOI: `10.1103/PhysRevLett.47.910`.

[46] C. Rolland and P. B. Corkum. “Compression of high-power optical pulses”. In: *Journal of the Optical Society of America B* 5.3 (1988), p. 641. DOI: `10.1364/JOSAB.5.000641`.

[47] C. P. Hauri, W. Kornelis, F. W. Helbing, A. Heinrich, A. Couairon, et al. “Generation of intense, carrier-envelope phase-locked few-cycle laser pulses through filamentation”. In: *Applied Physics B* 79.6 (2004), pp. 673–677. DOI: `10.1007/s00340-004-1650-z`.

[48] L. Gallmann, T. Pfeifer, P. M. Nagel, M. J. Abel, D. M. Neumark, et al. “Comparison of the filamentation and the hollow-core fiber characteristics for pulse compression into the few-cycle regime”. In: *Applied Physics B* 86.4 (2007), pp. 561–566. DOI: `10.1007/s00340-006-2503-8`.

[49] B. Beaurepaire, D. Guénot, A. Vernier, F. Böhle, M. Perrier, et al. “Limitations in ionization-induced compression of femtosecond laser pulses due to spatio-temporal couplings”. In: *Optics Express* 24.9 (2016), pp. 9693–9705. DOI: `10.1364/OE.24.009693`.

[50] S. C. Pinault and M. J. Potasek. “Frequency broadening by self-phase modulation in optical fibers”. In: *Journal of the Optical Society of America B* 2.8 (1985), p. 1318. DOI: `10.1364/JOSAB.2.001318`.

[51] F. DeMartini, C. H. Townes, T. K. Gustafson, and P. L. Kelley. “Self-Steepening of Light Pulses”. In: *Physical Review* 164.2 (1967), pp. 312–323. DOI: `10.1103/PhysRev.164.312`.

[52] A. L. Gaeta. “Catastrophic Collapse of Ultrashort Pulses”. In: *Physical Review Letters* 84.16 (2000), pp. 3582–3585. DOI: `10.1103/PhysRevLett.84.3582`.

[53] E. A. Marcatili and R. A. Schmeltzer. “Hollow Metallic and Dielectric Waveguides for Long Distance Optical Transmission and Lasers”. In: *Bell System Technical Journal* 43.4P2 (1964), pp. 1783+.

[54] R. L. Abrams. “Coupling losses in hollow waveguide laser resonators”. In: *IEEE Journal of Quantum Electronics* 8.11 (1972), pp. 838–843. DOI: `10.1109/JQE.1972.1076875`.

[55] C. Vozzi, M. Nisoli, G. Sansone, S. Stagira, and S. de Silvestri. "Optimal spectral broadening in hollow-fiber compressor systems". In: *Applied Physics B* 80.3 (2005), pp. 285–289. DOI: `10.1007/s00340-004-1721-1`.

[56] A. Malvache, X. Chen, C. G. Durfee, A. Jullien, and R. López-Martens. "Multi-mJ pulse compression in hollow fibers using circular polarization". In: *Applied Physics B* 104.1 (2011), pp. 5–9. DOI: `10.1007/s00340-011-4663-4`.

[57] A. Suda, M. Hatayama, K. Nagasaka, and K. Midorikawa. "Generation of sub-10-fs, 5-mJ-optical pulses using a hollow fiber with a pressure gradient". In: *Applied Physics Letters* 86.11 (2005). DOI: `10.1063/1.1883706`.

[58] S. Bohman, A. Suda, T. Kanai, S. Yamaguchi, and K. Midorikawa. "Generation of 5.0 fs, 5.0 mJ pulses at 1 kHz using hollow-fiber pulse compression". In: *Optics Letters* 35.11 (2010), pp. 1887–1889. DOI: `10.1364/OL.35.001887`.

[59] T. D. Nagy and P. D. Simon. "Lichtleiteranordnung, Herstellungsverfahren und Verwendung dafür". DE 102007048769 B3. 2009.

[60] T. Nagy, M. Forster, and P. Simon. "Flexible hollow fiber for pulse compressors". In: *Applied Optics* 47.18 (2008), pp. 3264–3268. DOI: `10.1364/AO.47.003264`.

[61] X. Chen, A. Malvache, A. Ricci, A. Jullien, and R. López-Martens. "Efficient hollow fiber compression scheme for generating multi-mJ, carrier-envelope phase stable, sub-5 fs pulses". In: *Laser Physics* 21.1 (2011), pp. 198–201. DOI: `10.1134/S1054660X11010063`.

[62] H. J. Lehmeier, W. Leupacher, and A. Penzkofer. "Nonresonant third order hyperpolarizability of rare gases and N2 determined by third harmonic generation". In: *Optics Communications* 56.1 (1985), pp. 67–72. DOI: `10.1016/0030-4018(85)90069-0`.

[63] J. Bernhardt, P. T. Simard, W. Liu, H. L. Xu, F. Théberge, et al. "Critical power for self-focussing of a femtosecond laser pulse in helium". In: *Optics Communications* 281.8 (2008), pp. 2248–2251. DOI: `10.1016/j.optcom.2007.12.001`.

[64] V. Pervak, I. Ahmad, M. K. Trubetskov, A. V. Tikhonravov, and F. Krausz. "Double-angle multilayer mirrors with smoothdispersion characteristics". In: *Optics Express* 17.10 (2009), pp. 7943–7951. DOI: `10.1364/OE.17.007943`.

[65] S. Akturk, C. D'Amico, and A. Mysyrowicz. "Measuring ultrashort pulses in the single-cycle regime using frequency-resolved optical gating". In: *Journal of the Optical Society of America B* 25.6 (2008), A63–A69. DOI: `10.1364/JOSAB.25.000A63`.

[66] M. Miranda, T. Fordell, C. L. Arnold, A. L'Huillier, and H. Crespo. "Simultaneous compression and characterization of ultrashort laser pulses using chirped mirrors and glass wedges". In: *Optics Express* 20.1 (2012), pp. 688–697.

[67] F. Silva, M. Miranda, B. Alonso, J. Rauschenberger, V. Pervak, et al. "Simultaneous compression, characterization and phase stabilization of GW-level 1.4 cycle VIS-NIR femtosecond pulses using a single dispersion-scan setup". In: *Optics Express* 22.9 (2014), pp. 10181–10191. DOI: `10.1364/OE.22.010181`.

[68] F. Lücking, A. Trabattoni, S. Anumula, G. Sansone, F. Calegari, et al. "In situ measurement of nonlinear carrier-envelope phase changes in hollow fiber compression". In: *Optics Letters* 39.8 (2014), p. 2302. DOI: `10.1364/OL.39.002302`.

[69] F. Böhle, M. Kretschmar, A. Jullien, M. Kovacs, M. Miranda, et al. "Compression of CEP-stable multi-mJ laser pulses down to 4 fs in long hollow fibers". In: *Laser Physics Letters* 11.9 (2014), p. 95401. DOI: `10.1088/1612-2011/11/9/095401`.

[70] H. Jacqmin, A. Jullien, B. Mercier, M. Hanna, F. Druon, et al. "Passive coherent combining of CEP-stable few-cycle pulses from a temporally divided hollow fiber compressor". In: *Optics Letters* 40.5 (2015), pp. 709–712. DOI: `10.1364/OL.40.000709`.

[71] H. Jacqmin, B. Mercier, A. Jullien, and R. López-Martens. "Manifold coherent combining of few-cycle pulses in hollow-fiber compressors". In: *Applied Physics B* 122.8 (2016). DOI: `10.1007/s00340-016-6488-7`.

[72] J. A. Wheeler, A. Borot, S. Monchocé, H. Vincenti, A. Ricci, et al. "Attosecond lighthouses from plasma mirrors". In: *Nature Photonics* 6.12 (2012), pp. 829–833. DOI: `10.1038/nphoton.2012.284`.

[73] Gibbon and Bell. "Collisionless absorption in sharp-edged plasmas". In: *Physical Review Letters* 68.10 (1992), pp. 1535–1538. DOI: `10.1103/PhysRevLett.68.1535`.

[74] D. Forslund, J. Kindel, K. Lee, E. Lindman, and R. Morse. "Theory and simulation of resonant absorption in a hot plasma". In: *Physical Review A* 11.2 (1975), pp. 679–683. DOI: `10.1103/PhysRevA.11.679`.

[75] F. Brunel. “Not-so-resonant, resonant absorption”. In: *Physical Review Letters* 59.1 (1987), pp. 52–55. DOI: `10.1103/PhysRevLett.59.52`.

[76] N. H. Burnett, H. A. Baldis, M. C. Richardson, and G. D. Enright. “Harmonic generation in CO 2 laser target interaction”. In: *Applied Physics Letters* 31.3 (1977), pp. 172–174. DOI: `10.1063/1.89628`.

[77] R. L. Carman, C. K. Rhodes, and R. F. Benjamin. “Observation of harmonics in the visible and ultraviolet created in C O2 -laser-produced plasmas”. In: *Physical Review A* 24.5 (1981), pp. 2649–2663. DOI: `10.1103/PhysRevA.24.2649`.

[78] A. McPherson, G. Gibson, H. Jara, U. Johann, T. S. Luk, et al. “Studies of multiphoton production of vacuum-ultraviolet radiation in the rare gases”. In: *Journal of the Optical Society of America B* 4.4 (1987), p. 595. DOI: `10.1364/JOSAB.4.000595`.

[79] N. Sarukura, K. Hata, T. Adachi, R. Nodomi, M. Watanabe, et al. “Coherent soft-x-ray generation by the harmonics of an ultrahigh-power KrF laser”. In: *Physical Review A* 43.3 (1991), pp. 1669–1672. DOI: `10.1103/PhysRevA.43.1669`.

[80] L’Huillier and P. Balcou. “High-order harmonic generation in rare gases with a 1-ps 1053-nm laser”. In: *Physical Review Letters* 70.6 (1993), pp. 774–777. DOI: `10.1103/PhysRevLett.70.774`.

[81] P. Antoine, A. L’Huillier, and M. Lewenstein. “Attosecond Pulse Trains Using High-Order Harmonics”. In: *Physical Review Letters* 77.7 (1996), pp. 1234–1237. DOI: `10.1103/PhysRevLett.77.1234`.

[82] I. P. Christov, M. M. Murnane, and H. C. Kapteyn. “High-Harmonic Generation of Attosecond Pulses in the “Single-Cycle” Regime”. In: *Physical Review Letters* 78.7 (1997), pp. 1251–1254. DOI: `10.1103/PhysRevLett.78.1251`.

[83] C. Spielmann, N. H. Burnett, S. Sartania, R. Koppitsch, M. Schnürer, et al. “Generation of Coherent X-rays in the Water Window Using 5-Femtosecond Laser Pulses”. In: *Science* 278.5338 (1997), pp. 661–664. DOI: `10.1126/science.278.5338.661`.

[84] M. Hentschel, R. Kienberger, C. Spielmann, G. A. Reider, N. Milosevic, et al. “Attosecond metrology”. In: *Nature* 414.6863 (2001), pp. 509–513. DOI: `10.1038/35107000`.

[85] K. Zhao, Q. Zhang, M. Chini, Y. Wu, X. Wang, et al. “Tailoring a 67 attosecond pulse through advantageous phase-mismatch”. In: *Optics Letters* 37.18 (2012), pp. 3891–3893. DOI: `10.1364/OL.37.003891`.

[86] J. Li, X. Ren, Y. Yin, K. Zhao, A. Chew, et al. “53-attosecond X-ray pulses reach the carbon K-edge”. In: *Nature communications* 8.1 (2017), p. 186. DOI: `10.1038/s41467-017-00321-0`.

[87] M. Drescher, M. Hentschel, R. Kienberger, M. Uiberacker, V. Yakovlev, et al. “Time-resolved atomic inner-shell spectroscopy”. In: *Nature* 419.6909 (2002), pp. 803–807. DOI: `10.1038/nature01143`.

[88] A. L. Cavalieri, N. Muller, T. Uphues, V. S. Yakovlev, A. Baltuska, et al. “Attosecond spectroscopy in condensed matter”. In: *Nature* 449.7165 (2007), pp. 1029–1032. DOI: `10.1038/nature06229`.

[89] S. V. Bulanov, N. M. Naumova, and F. Pegoraro. “Interaction of an ultrashort, relativistically strong laser pulse with an overdense plasma”. In: *Physics of Plasmas* 1.3 (1994), p. 745. DOI: `10.1063/1.870766`.

[90] R. Lichters, J. Meyer-ter-Vehn, and A. Pukhov. “Short-pulse laser harmonics from oscillating plasma surfaces driven at relativistic intensity”. In: *Physics of Plasmas* 3.9 (1996), p. 3425. DOI: `10.1063/1.871619`.

[91] T. Baeva, S. Gordienko, and A. Pukhov. “Theory of high-order harmonic generation in relativistic laser interaction with overdense plasma”. In: *Physical Review E* 74.4 (2006), p. 046404. DOI: `10.1103/PhysRevE.74.046404`.

[92] S. Kohlweyer, G. D. Tsakiris, C.-G. Wahlström, C. Tillman, and I. Mercer. “Harmonic generation from solid-vacuum interface irradiated at high laser intensities”. In: *Optics Communications* 117.5-6 (1995), pp. 431–438. DOI: `10.1016/0030-4018(95)00200-R`.

[93] D. von der Linde, T. Engers, G. Jenke, P. Agostini, G. Grillon, et al. “Generation of high-order harmonics from solid surfaces by intense femtosecond laser pulses”. In: *Physical Review A* 52.1 (1995), R25–R27. DOI: `10.1103/PhysRevA.52.R25`.

[94] U. Teubner, K. Eidmann, U. Wagner, U. Andiel, F. Pisani, et al. “Harmonic emission from the rear side of thin overdense foils irradiated with intense ultrashort laser pulses”. In: *Physical Review Letters* 92.18 (2004), p. 185001. DOI: `10.1103/PhysRevLett.92.185001`.

[95] F. Quéré, C. Thaury, P. Monot, S. Dobosz, P. Martin, et al. “Coherent wake emission of high-order harmonics from overdense plasmas”. In: *Physical Review Letters* 96.12 (2006). DOI: `10.1103/PhysRevLett.96.125004`.

[96] H. George, F. Quéré, C. Thaury, G. Bonnaud, and P. Martin. “Mechanisms of forward laser harmonic emission from thin overdense plasmas”. In: *New Journal of Physics* 11.11 (2009), p. 113028. DOI: `10.1088/1367-2630/11/11/113028`.

[97] Y. Nomura, R. Hörlein, P. Tzallas, B. Dromey, S. Rykovanov, et al. “Attosecond phase locking of harmonics emitted from laser-produced plasmas”. In: *Nature Physics* 5.2 (2008), pp. 124–128. DOI: `10.1038/nphys1155`.

[98] G. D. Tsakiris, K. Eidmann, J. Meyer-ter-Vehn, and F. Krausz. “Route to intense single attosecond pulses”. In: *New Journal of Physics* 8 (2006), p. 19. DOI: `10.1088/1367-2630/8/1/019`.

[99] C. Thaury and F. Quéré. “High-order harmonic and attosecond pulse generation on plasma mirrors: basic mechanisms”. In: *Journal of Physics B: Atomic, Molecular and Optical Physics* 43.21 (2010), p. 213001. DOI: `10.1088/0953-4075/43/21/213001`.

[100] B. Dromey, S. Kar, C. Bellei, D. C. Carroll, R. J. Clarke, et al. “Bright multi-keV harmonic generation from relativistically oscillating plasma surfaces”. In: *Physical Review Letters* 99.8 (2007), p. 085001. DOI: `10.1103/PhysRevLett.99.085001`.

[101] C. Rödel, D. an der Brügge, J. Bierbach, M. Yeung, T. Hahn, et al. “Harmonic generation from relativistic plasma surfaces in ultrasteep plasma density gradients”. In: *Physical Review Letters* 109.12 (2012), p. 125002. DOI: `10.1103/PhysRevLett.109.125002`.

[102] S. Kahaly, S. Monchocé, H. Vincenti, T. Dzelzainis, B. Dromey, et al. “Direct observation of density-gradient effects in harmonic generation from plasma mirrors”. In: *Physical Review Letters* 110.17 (2013), p. 175001. DOI: `10.1103/PhysRevLett.110.175001`.

[103] F. Dollar, P. Cummings, V. Chvykov, L. Willingale, M. Vargas, et al. “Scaling high-order harmonic generation from laser-solid interactions to ultrahigh intensity”. In: *Physical Review Letters* 110.17 (2013), p. 175002. DOI: `10.1103/PhysRevLett.110.175002`.

[104] F. Quéré, C. Thaury, J.-P. Geindre, G. Bonnaud, P. Monot, et al. “Phase properties of laser high-order harmonics generated on plasma mirrors”. In: *Physical Review Letters* 100.9 (2008), p. 095004. DOI: `10.1103/PhysRevLett.100.095004`.

[105] H. Vincenti, S. Monchoce, S. Kahaly, G. Bonnaud, P. Martin, et al. “Optical properties of relativistic plasma mirrors”. In: *Nature communications* 5 (2014), p. 3403. DOI: `10.1038/ncomms4403`.

[106] C. Thaury, F. Quéré, H. George, J. P. Geindre, P. Monot, et al. “High-order harmonic generation from plasma mirrors”. In: *The European Physical Journal Special Topics* 175.1 (2009), pp. 43–48. DOI: `10.1140/epjst/e2009-01115-6`.

[107] A. Malvache. "Optique non-linéaire à haute intensité: Compression d'impulsions laser Interaction laser-plasma". Dissertation. Palaiseau: Ecole Polytechnique, 2011.

[108] A. Malvache, A. Borot, F. Quéré, and R. López-Martens. "Coherent wake emission spectroscopy as a probe of steep plasma density profiles". In: *Physical Review E* 87.3 (2013). DOI: `10.1103/PhysRevE.87.035101`.

[109] A. Borot, A. Malvache, X. Chen, A. Jullien, J.-P. Geindre, et al. "Attosecond control of collective electron motion in plasmas". In: *Nature Physics* 8.5 (2012), pp. 416–421. DOI: `10.1038/nphys2269`.

[110] A. Leblanc, S. Monchocé, C. Bourassin-Bouchet, S. Kahaly, and F. Quéré. "Ptychographic measurements of ultrahigh-intensity laser–plasma interactions". In: *Nature Physics* 12.4 (2015), pp. 301–305. DOI: `10.1038/nphys3596`.

[111] C. Thaury, F. Quéré, J.-P. Geindre, A. Levy, T. Ceccotti, et al. "Plasma mirrors for ultrahigh-intensity optics". In: *Nature Physics* 3.6 (2007), pp. 424–429. DOI: `10.1038/nphys595`.

[112] A. Tarasevitch, K. Lobov, C. Wunsche, and D. von der Linde. "Transition to the relativistic regime in high order harmonic generation". In: *Physical Review Letters* 98.10 (2007), p. 103902. DOI: `10.1103/PhysRevLett.98.103902`.

[113] G. Sansone, L. Poletto, and M. Nisoli. "High-energy attosecond light sources". In: *Nature Photonics* 5.11 (2011), pp. 655–663. DOI: `10.1038/nphoton.2011.167`.

[114] P. Lan, P. Lu, W. Cao, Y. Li, and X. Wang. "Attosecond ionization gating for isolated attosecond electron wave packet and broadband attosecond xuv pulses". In: *Physical Review A* 76.5 (2007), p. 595. DOI: `10.1103/PhysRevA.76.051801`.

[115] H. Vincenti and F. Quéré. "Attosecond Lighthouses: How To Use Spatiotemporally Coupled Light Fields To Generate Isolated Attosecond Pulses". In: *Physical Review Letters* 108.11 (2012). DOI: `10.1103/PhysRevLett.108.113904`.

[116] A. Borot, R. López-Martens, J.-P. Geindre, and D. Douillet. "Device for generating a secondary source by laser-matter interaction, including an optical device for monitoring the position and the orientation of a moving surface". EP2364579 B1. 2009.

[117] M. Bocoum, F. Böhle, A. Vernier, A. Jullien, J. Faure, et al. "Spatial-domain interferometer for measuring plasma mirror expansion". In: *Optics Letters* 40.13 (2015), p. 3009. DOI: `10.1364/OL.40.003009`.

[118] M. Bocoum, M. Thevenet, F. Böhle, B. Beaurepaire, A. Vernier, et al. "Anticorrelated Emission of High Harmonics and Fast Electron Beams From Plasma Mirrors". In: *Physical Review Letters* 116.18 (2016), p. 185001. DOI: `10.1103/PhysRevLett.116.185001`.

[119] M. Bocoum. "High-Order Harmonics and Electron Beams from Plasma Mirrors". Dissertation. Palaiseau: ENSTA ParisTech, 2016.

[120] Y. Glinec, J. Faure, A. Guemnie-Tafo, V. Malka, H. Monard, et al. "Absolute calibration for a broad range single shot electron spectrometer". In: *Review of Scientific Instruments* 77.10 (2006), p. 103301. DOI: `10.1063/1.2360988`.

[121] A. Buck, K. Zeil, A. Popp, K. Schmid, A. Jochmann, et al. "Absolute charge calibration of scintillating screens for relativistic electron detection". In: *Review of Scientific Instruments* 81.3 (2010), p. 033301. DOI: `10.1063/1.3310275`.

[122] J.-P. Geindre, A. Mysyrowicz, A. D. Santos, P. Audebert, A. Rousse, et al. "Frequency-domain interferometer for measuring the phase and amplitude of a femtosecond pulse probing a laser-produced plasma". In: *Optics Letters* 19.23 (1994), p. 1997. DOI: `10.1364/OL.19.001997`.

[123] A. Borot. "Attosecond pulses generation from plasma mirrors at very high repetition rate". Dissertation. Palaiseau: Ecole Polytechnique, 2012.

[124] M. Thévenet, H. Vincenti, and J. Faure. "On the physics of electron ejection from laser-irradiated overdense plasmas". In: *Physics of Plasmas* 23.6 (2016), p. 063119. DOI: `10.1063/1.4954822`.

[125] A. Leblanc. "Miroirs et réseaux plasmas en champs lasers ultra-intenses: génération d'harmoniques d'ordre élevé et de faisceaux d'électrons relativistes". Dissertation. Saclay: Université Paris-Saclay, 2016.

[126] S. Kühn, M. Dumergue, S. Kahaly, S. Mondal, M. Füle, et al. "The ELI-ALPS facility: The next generation of attosecond sources". In: *Journal of Physics B: Atomic, Molecular and Optical Physics* 50.13 (2017), p. 132002. DOI: `10.1088/1361-6455/aa6ee8`.

[127] D. Guénot, D. Gustas, A. Vernier, B. Beaurepaire, F. Böhle, et al. "Relativistic electron beams driven by kHz single-cycle light pulses". In: *Nature Photonics* 11.5 (2017), pp. 293–296. DOI: `10.1038/nphoton.2017.46`.

ÉCOLE DOCTORALE
Ondes et Matière
(EDOM)

Titre: Génération d'impulsions laser proches du cycle optique pour le pilotage de miroirs plasma relativistes au kHz

Mots clefs: attoseconde, miroir plasma, optique non linéaire

Résumé: Notre groupe au LOA se concentre sur la génération d'impulsions attoseconde sur miroir plasma en régime relativiste. Pour cela, il cherche à développer une source d'impulsions femtosecondes à forte cadence et fort contraste et suffisamment énergétiques pour atteindre des intensités relativistes ($\gg 10^{18}\,\mathrm{W/cm^2}$) lorsqu'elles sont fortement focalisées sur un plasma surdense. Un plasma surdense réfléchit la lumière incidente et par conséquent agit comme un miroir qui se déplaçant à vitesse relativiste et qui comprime l'impulsion incidente, produisant ainsi un flash attoseconde par cycle optique.

Dans la première partie de mon travail de thèse, j'ai réalisé un compresseur nonlinéaire pour réduire la durée des impulsions issues d'une chaîne à double dérive de fréquence (10 mJ, 25 fs, 1 kHz) à phase enveloppe-porteuse (CEP) stabilisée. En propageant les impulsions du laser à haute intensité dans une fibre creuse remplie de gaz rare, j'ai réussi à générer des impulsions de 1.3 cycle optique avec une puissance crête autour de 1TW avec une CEP stabilisée. Dans un deuxième temps, j'ai mis en forme spatialement et temporellement les impulsions issues du compresseur à fibre pour générer à la fois des impulsions attosecondes intenses et des faisceaux d'électrons énergétiques sur un miroir plasma à gradient de densité contrôlé. Ces expériences nous permis, pour la première fois, de mettre en évidence la production d'impulsions attosecondes isolées dans l'XUV, l'émission corrélée de faisceaux d'électrons énergétiques en régime relativiste ainsi qu'un nouveau régime d'accélération d'électrons à très long gradient plasma.

Title: Near-single-cycle laser for driving relativistic plasma mirrors at kHz repetition rate - development and application

Keywords: attosecond, plasma mirror, ultrafast nonlinear optics

Abstract: Very short light pulses allow us to resolve ultrafast processes in molecules, atoms and condensed matter. This started with the advent of Femtochemistry and ever since, researcher have been trying to increase the temporal resolution. Nowadays we have reached attosecond pulse durations. Their generation, however, remains challenging and various different generation mechanisms are the topic of heated research around the world.

Our group at the LOA focuses on attosecond pulse generation on plasma mirrors in the relativistic regime. For this a high intensity, high contrast and high repetition-rate femtosecond laser chain is beeing developed to reach relativistic intensities ($\gg 10^{18}\,\mathrm{W/cm^2}$) when focused onto an overdense plasma (solid target).

During the first part of my PhD, I implemented a nonlinear compressor to reduce the duration of CEP stable laser pulses coming from double CPA laser system. While propagating these high intensity, but many cycle laser pulses through a gas filled waveguid (HCF), I was able to compress them to near-single-cycle duration (3.5 fs) and increase their peak intensity to 1 TW while maintaining controlled CEP. During the second part, I controled their spatio-temporal characteristics in a vacuum beamline to precisely drive relativistic high-harmonic-generation on solid targets. It was the first time ever that this has been achieved at 1 kHz repetition rate. By CEP gating the few-cycle-pulses, single attosecond pulses were generated. The conclusion has been supported by numerical simulations. Additionally a new regime to accelerate electron bunches on soft gradients has been detected.

Université Paris-Saclay
Espace Technologique / Immeuble Discovery
Route de l'Orme aux Merisiers RD 128 / 91190 Saint-Aubin, France